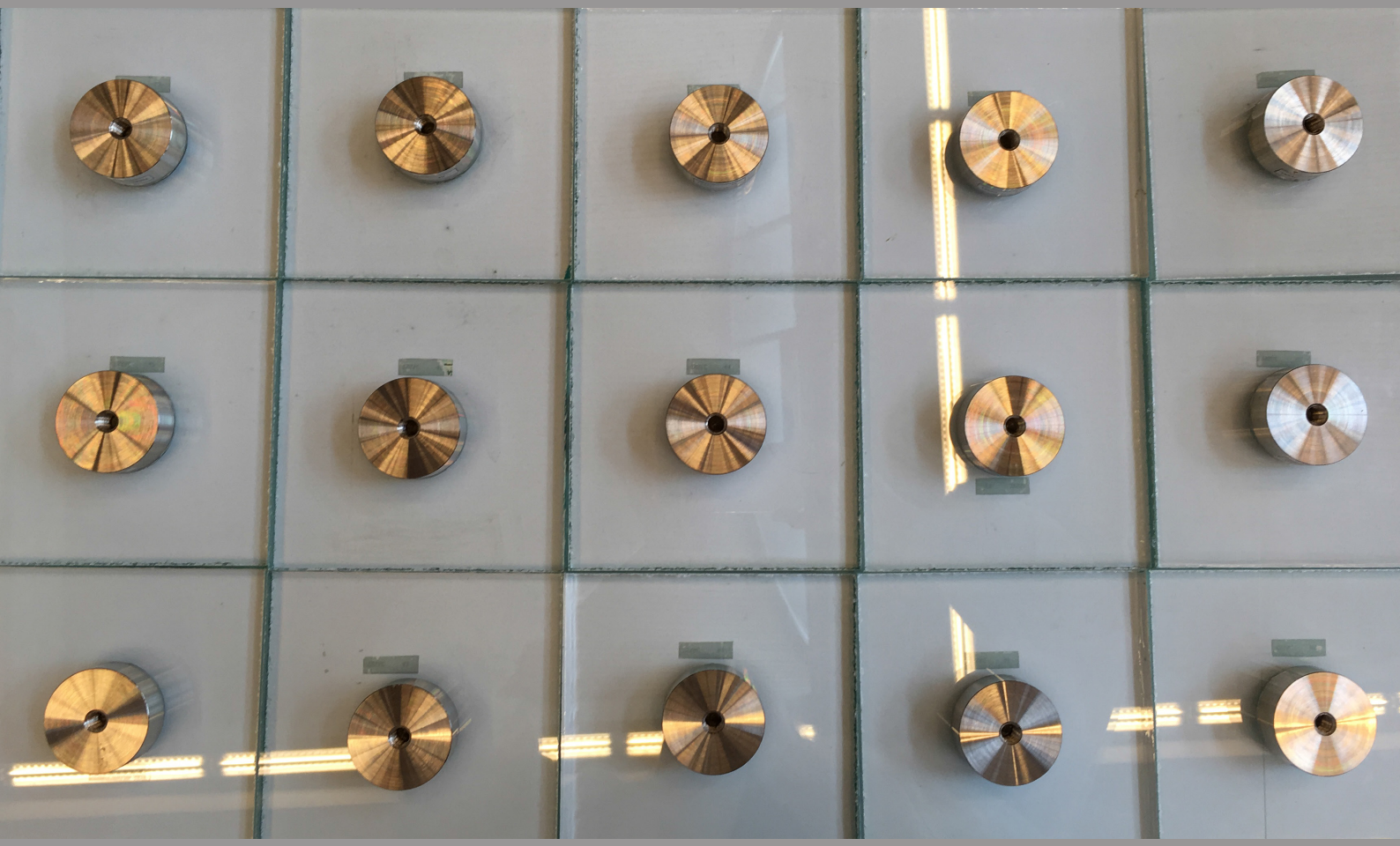
MSc Civil Engineering
Track: Building Engineering
Technical University of Delft

Master thesis:

MECHANICAL BEHAVIOUR OF TRANSPARENT STRUCTURAL SILICONE ADHESIVE LAMINATED CONNECTIONS UNDER MONOTONIC AND CYCLIC LOADING

Anna Ioannidou-Kati
4502558



Delft, Netherlands
October, 2017

Master thesis:

MECHANICAL BEHAVIOUR OF TRANSPARENT STRUCTURAL SILICONE ADHESIVE LAMINATED CONNECTIONS UNDER MONOTONIC AND CYCLIC LOADING

Student:
Anna Ioannidou-Kati
4502558 (student number)
Delft University of Technology
MSc Civil Engineering
Building Engineering track

Chair:

Prof. ir. Rob Nijsse
Department: Structural and Building Engineering

Committee:

Dr. ir. Christian Louter (daily supervisor)
Department: Architectural Engineering & Technology

Ir. PA de Vries
Department: Structural Engineering and Building Techn. Structures

Dr. Sofia Teixeira de Freitas
Faculty of Aerospace Engineering

Dt. ir. Manuel Santarsiero (external supervisor)
Company: Eckersley O'Callaghan

TU Delft

Abstract

Transparency and translucency are essential features of modern architecture. Glass products have been widely used in facade applications and recently their use has expanded to the load-bearing structure due their large in-plane compressive strength. However, the fragile nature of glass requires special treatment and attention to detail to avoid fracture caused by tensile stresses. Connections between glass components are very critical to the structural integrity of the system. Bolted connections, which are often used to transfer forces between glass elements, require drilling the glass. This process may cause additional flaws and stress intensifications around the holes and thus reduces the bearing capacity of glass elements. Adhesive connections offer an alternative approach for the connecting joints and enable a more uniform distribution of stresses. Laminated connections have recently been developed that combine high strength and transparency. This work focuses on the Transparent Structural Silicone Adhesive (TSSA), produced by Dow Corning, that is used for the realization of laminated connections. TSSA connections have been used in several projects worldwide; however, the hyperelastic and viscoelastic nature of the material has not been fully investigated. In this work, the mechanical response of TSSA laminated connections under static and cyclic loading is investigated by means of experimental, analytical and numerical studies.

Firstly, the shear behaviour of TSSA laminated circular connections is characterized by means of monotonic and cyclic loading tests at different frequencies. The hysteretic behaviour of the material under loading cycles, which is caused due to its viscoelastic nature, is analyzed. The adhesive exhibits significant stress-softening under repeated cycles that becomes more severe as the maximum load increases. Energy dissipation analysis is conducted to understand the nature of this phenomenon with the aim to simplify the cyclic behaviour of the adhesive for modeling purposes.

Secondly, TSSA laminated circular connections are subjected to monotonic and cyclic tensile loading of increasing maximum load. The development of the whitening phenomenon is studied for both cases. The stress level when whitening appears for the first time and the way it propagates to the adhesive surface show some consistency both for the cases of static and cyclic loading. The occurrence of the stress-softening phenomenon is also recorded, in order to observe whether it appears within the working limit of the connection.

Thirdly, the deformation behaviour of the adhesive is described analytically based on hyperelastic prediction models. Conventional test set-ups, such as uniaxial and biaxial tension tests, are combined with the simple shear test results obtained within the framework of this thesis, for the material characterization of TSSA. The hyperelastic material parameters are calibrated by a simultaneous multi-experiment-data-fit based on the nonlinear least squares optimization method. The softening behaviour observed in shear tests is modeled based on a simplified pseudo-elastic damage model, which is supported by most finite element software. A first attempt is also made to model the actual softening response of the adhesive. A less conservative approach proposed by Guo, also based on the theory of pseudo-elasticity, proved to give a good approximation of the actual cyclic response of the adhesive.

Finally, TSSA laminated connections on the edge of the glass are experimentally and numerically investigated. The edge bonded specimens are tested in shear and the stress distribution of the adhesive is analyzed by means of a three-dimensional finite element model. The distribution of stresses in the adhesive is non-linear showing significant stress peaks towards the free edges of the adhesive. A parametric study is conducted to relate the magnitude of the stress peaks with the eccentricity of the applied load.

Acknowledgements

This master thesis was written as part of the Building Engineering MSc programme at the Delft University of Technology. I would like to take this chance to express my gratitude to those who have contributed to the completion of this MSc thesis project.

Firstly, I would like to express my sincere gratitude to Dr. ir. Christian Louter, for the continuous support of my master thesis study and related research. Thank you for always having the time to discuss the progress of my thesis, whenever I ran into a trouble spot or had a question about my research. I am also very grateful to Dr. Manuel Santarsiero, who has helped me from distance. Your knowledge and experience were of great value and thank you for always keeping me on the right track. I would also like to express my sincere gratitude to ir. Peter de Vries for his valuable input during the design and preparation of the tests and Dr. Sofia Teixeira de Freitas for taking the time to reflect on my findings and for her useful insight on adhesives. Thank you for your guidance and useful advice on my writing. Finally, I would like to thank Rob Nijsse, the chair of the committee, for providing valuable feedback to improve my work and for keeping me in the right direction.

Furthermore, I would like to express my gratitude to James O'Callaghan, for listening to the findings of this thesis and for his valuable advice relating research with practice. I am also grateful to Dr. ir. Max Hendriks and and Peter Eigenraam, who provided useful advice on the numerical analysis and modelling.

My sincere gratitude goes out to Kees Baardolf, who helped me prepare the test set-ups, and Fred Schilperoort, who provided technical support throughout the experiments. Without their precious help and support it would not be possible to conduct this research. I would also like to express my special thanks to Fred Bosch from the Delft Aerospace Structures and Materials Laboratory, who gave me access to the laboratory's equipment and for his valuable insights into lamination procedures.

Last but not the least, I would like to thank my family for supporting me spiritually throughout writing this thesis and my my life in general.

Anna Ioannidou-Kati

Delft, October 2017

This thesis is dedicated to my father.

Contents

1 Introduction **9**

1.1 Background . . . 9
1.2 Structural glass . . . 10
1.3 Connections for structural glass components . . . 14
1.4 Problem definition and objectives . . . 18
1.5 Thesis outline . . . 20

2 Transparent Structural Silicone Adhesive (TSSA) **21**

2.1 Introduction . . . 21
2.2 Characteristics and properties of TSSA . . . 22
2.3 Studies on TSSA laminated connections . . . 26
2.4 Standard specifications and norms . . . 29

3 Analysis of hyperelastic materials **31**

3.1 Introduction . . . 31
3.2 Finite deformation theory . . . 31
3.3 The Mullin's effect - stress-softening phenomenon . . . 32
3.4 Fundamental theory of constitutive models . . . 34
3.5 Phenomenological models . . . 38
3.6 Mechanical modeling of the stress-softening effect . . . 41

4 Experimental analysis of shear tests **45**

4.1 Method . . . 45
4.2 Results . . . 49
4.3 Analysis and discussion . . . 54
4.4 Conclusions . . . 59

5 Experimental analysis of tensile tests 60

5.1 Method . . . 60

5.2 Results . . . 64

5.3 Analysis and discussion . . . 69

5.4 Conclusions . . . 73

6 Assessment of hyperelastic material models 74

6.1 Introduction . . . 74

6.2 Methodology . . . 75

6.3 Results and discussion . . . 83

6.4 Conclusions . . . 87

7 TSSA laminated connections on the edge of the glass 88

7.1 Method . . . 88

7.2 Experimental analysis . . . 93

7.3 Numerical analysis . . . 94

7.4 Discussion and conclusions . . . 98

8 Conclusions and recommendations 101

8.1 Conclusions . . . 101

8.2 Recommendations for future research . . . 103

Bibliography 104

A Appendix: Shear tests 109

B Appendix: Tensile tests 117

C Appendix: Curve fitting hyperelastic and damage models to experimental data 124

D Appendix: TSSA laminated connections on the edge of the glass 126

Chapter 1

Introduction

1.1 Background

Glass is a material widely used in contemporary architecture. It combines aesthetics, it enables natural light to enter the building, it is weather resistant and does not gradually degrade by any chemical or environmental effects. A few years ago, glass components have almost exclusively been used in facade applications. Recently, its use has expanded to the load bearing structure due to the high compressive strength that it offers. Even though glass comes with high strength, engineers are still reluctant of using it as a structural material due to its brittle behaviour and fragile nature. In fact, the bearing strength of glass components largely depends on the surface flaws or cracks, as even the smallest flaw may prove to be crucial for the structural behaviour of the component.

Although, glass exhibits a purely elastic behaviour and breaks without warning, specific treatments have been developed that mitigate these problems and allow its use as a load-bearing element. One of the biggest challenges that still remains in structural glass engineering is the connecting joints. These can either be metal-to-glass or glass-to-glass, with the former being the most commonly used. Connections, and especially point ones, always cause stress peaks. Glass elements cannot accommodate these peaks due to their inability to plastically redistribute stresses [1] and thus their bearing capacity is significantly reduced. Further reduction of the strength is caused by drilling the glass in case of mechanical (bolted) connections. On the other hand, the development of adhesive connections seems promising for structural glass applications. They allow a more uniform distribution of stresses and avoid drilling the glass. A special case of such connections is laminated connections, which require autoclave-heating curing. These are realized with the use of specific polymer foils / interlayers that combine high transparency and strength. Even though extensive research has been performed on the mechanical response of laminated connections, there are still a lot of unanswered questions regarding cyclic behaviour, fatigue and aging effects.

This chapter gives an introduction to structural glass as a load bearing material and focuses on the connection types that are currently used in building construction or are still under research. In Section 1.2, an overview of structural glass, its properties, fabrication process and treatments is presented. Then the state-of-the-art of steel to glass connections, both mechanical and adhesive, is provided in Section 1.3. Finally, the problem definition and the objectives of the thesis are described in Section 1.4.



Figure 1.1: Apple 5th Avenue Mark 2, New York (Source: Eckersley O'Callaghan)

1.2 Structural glass

1.2.1 Chemical composition

Materials can be categorized in the following five groups [2]:

- Metals and alloys
- Polymers
- Elastomers
- Ceramics and glasses
- Composites

Ceramics and glasses belong in the same category; however they have some basic differences regarding their micro-structure. Glasses are non-crystalline (or amorphous) solids, whereas ceramics are crystalline, inorganic non-metals [2]. Amorphous solids are characterized of irregular arrangement of silicon and oxygen atoms, a fact which mainly depends on the production process [3]. The amorphous state of glass is advantageous when it comes to its stability and chemical resistance against a large variety of solvents and acids [3].

Clear glass used in construction typically consists of soda-lime silica. The main constituents of glass are presented in Table 1.1.

Table 1.1: Chemical composition of soda-lime silica glass [4]

Chemical component	Chemical formula	Mass amount %
Silicone dioxide	SiO_2	69-74
Calcium oxide	CaO	5-14
Sodium oxide	Na_2O	10-16
Magnesium oxide	MgO	0-6
Aluminium oxide	Al_2O_3	0-3
Others	-	0-5

1.2.2 Material properties

In Table 1.2, the most important physical properties of glass are presented.

Table 1.2: Physical properties of glass [2]

Material properties	Notation	Unit	Value
Softening temperature	T_s	°C	530 (varies with composition)
Glass transition temperature	T_{glass}	°C	570 (varies with composition)
Thermal conductivity	λ	W/m/K	1
Coefficient of thermal expansion	α_T	1/K	7.7 - 8.8 x 10^{-6}
Reflective index within visible spectrum	η	-	1.52

Thermal expansion coefficient is a critical property of glass that must be taken into consideration when designing steel to glass connections. It describes the change in size per unit length of a specific material under a temperature change of 1 K. The thermal coefficient of glass is approximately 1.5 times lower than that of steel and 2.4 times lower than that of aluminum [3]. It is evident that rigid steel to glass or aluminum to glass connections should be avoided due to the brittle behaviour of glass. Furthermore, glass has relatively high thermal conductivity, meaning that heat is transferred through the glass with no significant losses. For this reason, in facade applications double or triple glazed units are common practice in order to reduce the thermal conductivity of the system.

Propagation of light and sound through the glass are also critical physical properties that usually demand post-processing of the glass elements according to the specific needs. Approximately 90% of solar radiation is transmitted through a single glass pane and the rest is absorbed and reflected. Only the short wavelengths of the visible spectrum pass through the glass into a closed space. However, they are converted by the surrounding materials into high wavelengths leading to heat release [3]. This phenomenon is mitigated by further processing the glass with the use of special coatings or tints which minimize the light transmittance. Propagation of sound follows the same principle as light, part of it is reflected, absorbed or transmitted through the glass. The amount of sound that is reflected depends on the frequency. Higher frequency sounds cause higher reflections. Acoustic isolation is achieved by increasing the sound absorption of glass either by using plates of higher thickness or by laminating plates with varying thicknesses [3].

1.2.3 Mechanical properties

Glass exhibits high strength in compression and is weaker in tension. More specifically, annealed glass has a characteristic tensile bending strength of 45 MPa [5]. Glass shows a perfect elastic mechanical response when loaded, until the point when it fractures without warning. Brittle fracture may be caused by bending stresses, thermal stresses, imposed strains or impact loading. The glass flaws, the stress level and the duration of loading largely determine the point of fracture. Glass flaws are micro-cracks which may even exist right after the production process or are later caused from cutting, grinding or drilling the glass [2]. Under sustained and cyclic loading slow growth of these cracks is expected [2, 6]. Humidity also encourages crack growth [2] when tensile stresses are present. In general, the behaviour of the glass is considered stochastic, a fact which means that the larger the glass surface is, the higher the probability of finding flaws [3].

Table 1.3: Standard glass mechanical properties [3, 2]

Mechanical properties	Notation	Unit	Value
Density	ρ	kg/m^3	2500
Modulus of elasticity	E	MPa	70000 - 74000
Poisson's ratio	ν	-	0.22 - 0.23

1.2.4 Production process

There are many different types of annealed glass depending on the requirements of the design. Clear, tinted, printed or coated glass are some of the different options that are possible these days. The basic production procedure though is the same and is referred to as the "float process", developed by Pilkington Brothers in the early sixties. This process currently represents 90% of the world's flat glass production [3]. The "float process" begins by blending together silica sand, soda ash, limestone, salt cake and cullet (recycled broken glass). Then the mixture is heated up to 1500°C to form molten glass. The molten glass is then let to flow on top of a molten tin bath, where heating is controlled in order to make sure that the glass forms a smooth flat ribbon of uniform thickness. Subsequently, the glass slowly cools down to 600°C (glass transition temperature) to gain its viscosity and then is led into the annealed lehr (oven) to be further gradually cooled under controlled conditions. This step is very important, as the speed of the rollers that lead the glass into the oven determines the thickness of the plates [2]. In the end, the glass is inspected with special video recording equipment to ensure that no imperfections are present. Subsequently, the edges of the glass are trimmed and the panels are cut into the prescribed lengths [2].

1.2.5 Glass post-processing and treatments

After the completion of the float glass production process, the glass can be further treated in order to enhance its properties.

Mechanically treated glass

After the float process the glass panels are cut to the prescribed sizes either by using water jets or a diamond wheel. These cutting methods result in very sharp and weakened edges. Therefore, the edges

are usually chamfered, sanded or polished in order to create a smoother finish [3]. The glass plates may further be treated in case the design requires mechanical point fixings. In such cases, the glass must be drilled by using complicated machinery that allows simultaneous drilling of the glass on both sides in order to avoid stress peaks [3].

Laminated glass

The process during which two or more pieces of glass are bonded together with the use of an interlayer is called lamination. Interlayers come in varying thicknesses from 0.4mm up to 6mm. The most common materials used are Polyvinylbutyral (PVB) and resins such as acrylic [2]. Laminated glass components may combine many different thicknesses or even other materials such as poly-carbonates. The lamination process takes place in three basic steps; first the interlayers are positioned between the glass panels, then pre-lamination follows under a specified temperature and finally the elements are placed inside an autoclave where they are heated up to temperatures of 130°C to 150°C under a pressure of 13 bars [4].

Glass lamination is very beneficial when it comes to safety, because in case of breakage of the outside layers the broken pieces will remain bonded to the interlayer. The interlayer has also a damping effect against sound, a fact which makes laminated panels to absorb sound better then single layered glass panes. Furthermore, it is possible to produce tinted interlayers which provide better control of solar radiation.

Heat strengthened glass

Heat strengthened glass is created by heat treating the glass right after its fabrication. As already mentioned, glass has significantly higher compressive than tensile strength. In addition, glass has micro-cracks at its surface and thus it is very sensitive to tensile forces close to this area. The heat strengthening procedure involves heating the glass above its softening point at approximately 620°C and then letting the glass to cool down [2]. This process induces tensile stresses in the middle of the element's cross section and compressive stresses towards the surface of the glass. This is because the surface cools and solidifies faster then the middle part of the cross section and as the interior cools down and tries to shrink, tensile forces are created [2]. This procedure can also be referred to as glass pre-tensioning. The main characteristic of heat strengthened glass is the breaking pattern. Heat strengthened glass breaks into large pieces. This breaking pattern renders possible for glass elements to keep a percentage of their original strength (post breakage capacity), a fact which is favorable for the design of glass beams and columns. The characteristic tensile bending strength of heat strengthened glass is 70 MPa [5].

Toughened (or fully tempered) glass

The manufacturing of toughened glass is similar to the heat strengthening process already described. The main difference is that, in this case, the glass is cooled down rapidly with cold air jets and this leads to higher pre-tensioning stresses. The typical value of the characteristic tensile bending strength of toughened glass is 90 MPa. Toughened glass breaks into small fragments, a fact which makes it suitable for vertical facade panels close to circulation areas and roof elements. However, its post breakage capacity is rather low compared with heat strengthened glass.

Another disadvantage of toughened glass is that it might suddenly break after several years in use. This is because Nickel Sulfide (NiS) inclusions may appear during the fabrication process. These particles

increase rapidly in volume due to temperature changes and thus the inner tensile strength of the glass may be exceeded. Heat soak tests are usually conducted in order to reduce the possibility of sudden fractures during the life cycle of the building. These tests require heating the glass for a period of time after heat treatment at relatively high temperatures.

Chemically strengthened glass

Chemical strengthening is an alternative glass treatment that involves immersing the glass in a potassium bath at 450°C. This causes the exchange of the sodium ions that exist on the glass surface and potassium ions [2]. The latter are significantly larger and as they integrate to the glass micro-structure they cause compression of the glass surface. The disadvantage of this method is that it causes a thinner compressive layer compared with the thermal toughening process [2]. Even though chemical strengthening is an effective way to induce compression near the surface of the glass, flaws may also exist even deeper than the thin compressive zone caused by the potassium ions and thus this method is avoided for structural applications [3].Chemically strengthened glass exhibits six to eight times higher strength than annealed (float) glass; however, it breaks in large pieces and therefore it cannot be considered as safety glass.

1.3 Connections for structural glass components

One of the biggest challenges when designing glass structures is realizing the connection joints. In most structural glass applications, the glazed elements are supported by secondary steel, aluminum or even glass structures. They are usually connected to these supporting structures via point or linear connections that can be either mechanical (bolted) or adhesive.

1.3.1 Considerations

These days various types of steel to glass connections exist that can provide either a soft or a rigid connecting behaviour. Soft connections are easily deformed and thus stress peaks, which may lead to an abrupt fracture of the glazed component, are avoided. However, too soft connections cannot ensure composite action of steel and glass and thus the transfer of loads to the substructure may be insufficient [3]. On the other hand, stiff connections allow the full transfer of loads from the glass component to the substructure, but they do not avoid stress peaks which may prove to be crucial for the design. For example, stiff connections cannot accommodate in-plane stresses induced by thermal loads and may lead to failure of the glass [3]. Therefore, a middle ground solution between a too stiff and too soft connection is considered as the optimum.

Manufacturing tolerances are also a very important matter when designing connections for structural glass components. Mechanical connections, discussed in more detail in Section 1.3.2, involve the drilling of holes in the glass. The manufacturing of these holes requires special attention to their finishing, their size, the distance from each other and from the edges of the component [3]. For adhesive connections, the geometry, uniformity (less air bubbles possible) and dimensions of the adhesive layer are decisive factors for the behaviour of the connection [3]. Furthermore. the tolerances are often determined based on the installation process and the level of prefabrication. For example, in case of in-situ installation of mechanically supported glass elements, the lifting and fixing method highly influence the design of tolerances.

Another important consideration regarding steel to glass connections is the contact method. Direct contact between steel and glass should be avoided. Steel, aluminium or other metal alloys that are used in structural glass connections are very stiff materials with rough surfaces that are capable of damaging the glass. In addition, there is a high chance that impurities (e.g. dust or sand particles) infiltrate the connecting interface during fabrication causing a degradation of the properties of glass over time [3]. Therefore, soft plastic materials are often used on the interface of glass and steel elements.

1.3.2 Mechanical connections

Mechanically fixing the glass is the most widely used type of steel to glass connection. First, linear supporting glass was developed and nowadays point fixations realized with bolts or clamping devices are coming more and more into practice.

Linear supports

Linearly supported glazing systems is the most popular type of supporting construction in the facade industry. The linear support is usually implemented by a metallic frame onto which the glass panels are fixed. Soft elastic materials such as Neoprene or EPDM rubber blocks are used to accommodate deformations caused by thermal variations and the self-weight of the glazing [3], as well as to avoid direct contact of glass and steel. The out-of-plane loads are transferred by the glass plate to the supporting structure by means of an elastic material, which is positioned exactly on the interface between the glass and the metal frame.



Figure 1.2: Linearly supported glass facade (Source: Forster Profile Systems)

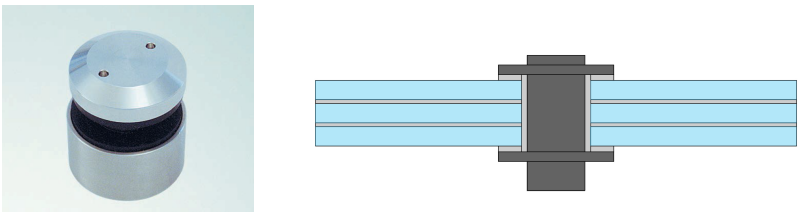
Bolted connections

Bolted connections require drilling holes in the glass. These holes must have larger diameter than that of bolts to make space for inserting soft materials (with low E modulus). In this way direct contact of glass and steel is avoided and a more uniform redistribution of loads is ensured. The use of soft materials at the interface between glass and steel also accommodates possible misalignments caused by laminating multiple glass panels together. Soft materials used in these applications can be aluminium alloys, plastics (EPDM, POM and polyamide), cast resins or mortars [3].

Mechanical fixing glass elements with bolts requires special attention from the designer, since stress concentrations are expected around the holes of the glass. Therefore, the positioning of these holes must conform to the existing national or international standards. In addition, due to weakening of the

glass at these points, the use of annealed glass is not recommended and thus heat strengthened or tempered glass must be used [7].

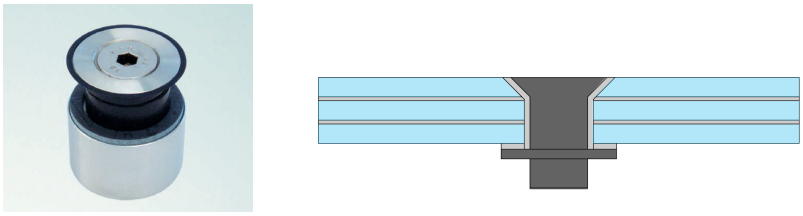
Point fitted connections may be designed with cylindrical or conical shaped bolts. Figure 1.3 illustrates a basic configuration of a cylindrical shaped bolted connection. This type of connection requires a clamping mechanism in order to restrain the out-of-plain bending of the glass element. This is achieved by using two steel plates on both sides of the glass with a soft material interlayer in between [3]. Several disadvantages of this clamping mechanism are the reduction of transparency as well as the fact that they are not easily cleaned resulting in water and dust accumulating around the steel plates [3].



(a) (b)

Figure 1.3: Picture (Source: Glasströsch) (a) and scheme (b) of cylindrical shaped bolted connections

In the case of conical shaped bolts, the out-of-plane loads are restrained only by the bolts [3] due to their geometry. Such configuration requires a steel plate only from the inside face of the glass and thus the outer surface of the glazed structure appears more sleek and can be very easily cleaned, avoiding dust accumulation. The downside of conical shaped connections is that they have a small contact area between the bolt and the glass, resulting in high stress concentrations and no post breakage capacity [3]. However, this can be mitigated by introducing a hinge into the system. Hinged point connections that allow rotations of 10° to 20° have been developed to enhance the behaviour of glass under out-of-plane loads [3]. Finally, the fabrication of those connections is difficult, as there is the need for precise fixation of the conical bolt inside the glass hole [3]. Figure 1.4 illustrates a basic example of conical shaped bolts.



(a) (b)

Figure 1.4: Picture (Source: Glasströsch) (a) and scheme (b) of conical shaped bolted connections

A variation of the conical shaped connections, illustrated in Figure 1.4, is undercut ties. This type of connection results in a sleek finish, without steel elements protruding out of the glass. The bolts do not penetrate through the glass, but are embedded inside the thickness of the plate as illustrated in Figure 1.5. To avoid stress peaks caused by direct contact of steel and glass, a bushing material (e.g. polyamide PA6) must be used [3]. The conical shaped hole is manufactured in indoor conditions with a special drill that is able to rotate [3].

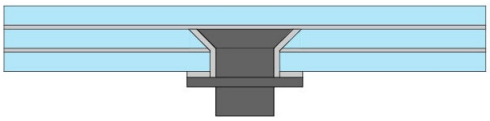


Figure 1.5: Embedded conical shaped bolt

Clamped connections

The configuration of clamped fixations is very close to the one already described for linear supports. Their difference is that clamped connections provide local supporting conditions and thus they enable lighter and more transparent facade structures. Clamped connections can be designed at the vertical edges of the glazed element, but also at the horizontal edges to support the self-weight of the glass. In such cases, Neoprene or EPDM rubber blocks are used at the bottom of the clamps to accommodate uneven deformations. The interlayer that separates the glass from the steel clamp is often made of frictionless materials, such as Teflon [3]. The main advantage of clamped connections compared with linear supports is that they do not exhibit drainage problems often caused by water accumulation inside the channel of the metal frame [3].

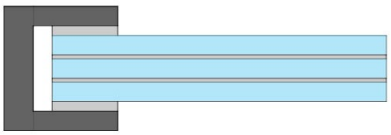


Figure 1.6: Clamped connection

1.3.3 Adhesive connections

Cold-curing adhesive connections

The mechanical connections discussed in the previous section come with some important disadvantages, such as the non uniform distribution of loads causing stress peaks to the glazed elements. Adhesive connections have recently been developed which allow an almost uniform stress distribution and the ability to transfer high loads from the glass to the substructure. Based on current construction practice, adhesive connections for exterior applications, such as for building envelopes, are limited to structural silicone sealants and acrylic-pressure sensitive adhesive (structural) foam tapes [7]. Structural silicone sealants, in specific, are used for the last 60 years and thus a great standardization level has been achieved. Their disadvantage is that they are not strong and require a thick opaque layer to ensure structural integrity. On the other hand, recent studies have examined the performance of photo-cured acrylics, which provide a transparent effect. However, results showed insufficient water resistance and thus this option is considered not suitable for exterior applications [7].

Laminated or heat-curing adhesive connections

Laminated connections that have been developed the recent years are very promising and constitute an innovative way of using transparent adhesive foils for bonding steel to glass. They are called laminated, because they are fabricated in the same principle as laminated glass panels where the lamination process takes place inside an autoclave. [8].

Laminated connections can be realized by using different types of adhesives such as SentryGlas® (SG) from Kuraray (former Dupont) or Transparent Structural Silicone Adhesive (TSSA) produced by Dow Corning. SG is a thermoplastic rigid ionomer adhesive and due to its transparent appearance after curing, it is mainly used in laminated glass applications. Compared to other interlayers, such as PVB[1] or EVA[2], SG has higher stiffness and strength as well as it exhibits enhanced durability [8]. Transparent Structural Silicone Adhesive (TSSA), which is the focus of this study, is a structural addition-cured flexible silicone that exhibits higher stiffness and strength compared with other silicone adhesives used in construction. Even though it exhibits quite lower strength than SG, it shows high durability against water and aging exposure. In addition, in contrast with most commonly used adhesives it shows great stability against temperature variations [1].

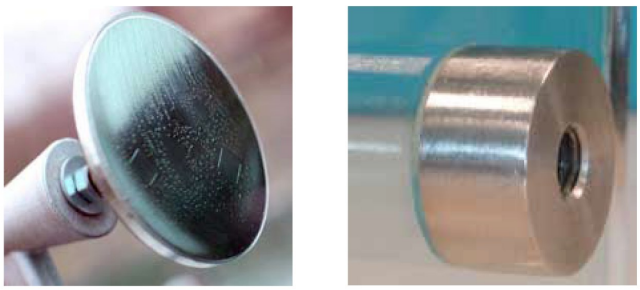


Figure 1.7: Transparent adhesive steel-to-glass connections (Source: Dow Corning)

1.4 Problem definition and objectives

In this research, the deformation behaviour of TSSA connections under monotonic and cyclic loading is studied. In the past, research on the mechanical behaviour of TSSA connections under monotonic loading has been performed by Santarsiero et al. [8, 1], Hagl et al. [9] and Sitte et al. [7] who studied the mechanical response of TSSA dumbbell specimens and TSSA laminated circular connections. However, very few experimental data exist on the cyclic behaviour of TSSA. Sitte et at. [7] conducted uniaxial, simple shear and equibiaxial cyclic tests and observed that the stiffness of TSSA changes when submitted to loading cycles. TSSA is a rubber-like material that exhibits hyperelastic behaviour when loaded. Rubber materials always exhibit viscoelastic behaviour that leads to hysteresis when loaded cyclically. In literature, this is referred to as the stress-softening effect of hyperelastic materials. This phenomenon was extensively investigated by Mullins [10, 11, 12] and therefore it is also referred to as the "Mullins effect".

[1] Polyvinyl butyral or PVB is a kind of resin usually used for laminating safety glass and offers strong adhesion and optical clarity.

[2] Ethylene vinyl acetate or EVA is the copolymer of ethylene and vinyl acetate. EVA film is used for laminating glass panels for interior and exterior applications.

Within the framework of this research, TSSA laminated circular connections with diameter 50mm are subjected to a series of monotonic and cyclic - shear and tensile tests. The first objective of this master thesis is to study the mechanical response of these connections under loading cycles and to observe if they exhibit the stress-softening effect. The aim is to record when the stress softening phenomenon occurred for the first time and to study the softening behaviour of the adhesive in different load levels, frequencies and number of cycles.

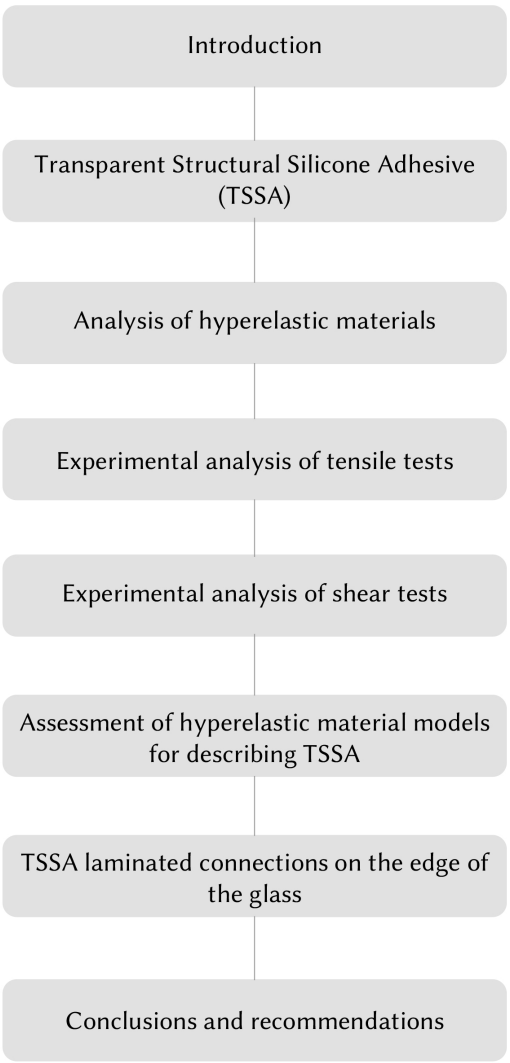
Furthermore, the development of the whitening phenomenon, that TSSA exhibits when stretched, will be compared under monotonic and cyclic loading. Santarsiero et al. [8, 1], Sitte et al. [7] and Hagl et al. [9] have observed that TSSA turns white after a certain stress level. This whitening phenomenon causes a reduction of the reflective index of TSSA and thus influences the design limit of those connections (see Section 2.2.5). The second objective of the thesis is to understand whether the stress level when whitening starts to develop appears to be consistent both for cases of static and cyclic loading, as well as to observe if the whitening of the adhesive recovers after removing the load.

Even though significant research has been performed on the mechanical response and the stress state of circular TSSA connections as well as a generalized failure criterion has been developed by Santarsiero [1], the non-linear properties of TSSA are still unknown. This makes it difficult to produce a finite element model that sufficiently describes the deformation state of the adhesive under various stress levels. The adherents, which are usually glass and stainless steel, may be modeled very accurately with linear properties; however, hyperelastic materials, such as TSSA, require a non-linear constitutive law in order to reproduce their behaviour using finite elements. In literature, there is a broad range of hyperelastic material laws, most of which can be implemented in finite element software. The accuracy of the predicted response of the adhesive largely depends on the chosen model. Therefore, the third objective of this master thesis is the calibration of the various material models based on the experimental data and the assessment of each model in terms of its suitability to describe the stress-strain response of the adhesive. The experiments conducted in this study are combined with uniaxial tests performed by Santarsiero [1] and biaxial tests performed by Drass et al. [13, 14].

The simulation of the mechanical response of TSSA will be extended to account for the stress-softening effect. The goal is to understand whether the softening behaviour, in the tested configuration, follows a pattern. This would allow the simplification of the problem and thus to create a method for analyzing the phenomenon for civil engineering purposes. Subsequently, various “damage models” are going to be assessed based on their ability to recreate the softening behaviour of the adhesive.

Finally, the possibility of using TSSA in an alternative configuration is going to be addressed. More specifically, the first attempt in utilizing TSSA to implement laminated connections on the glass edge is going to be experimentally and numerically studied. Laminated TSSA connections on the glass edge are fabricated and tested in shear. The deformation behaviour, the failure load and the stress distribution of those connections is going to be analyzed. The objective is to understand the performance of those connections and discuss advantages or weaknesses that would be relevant for further research and development of edge bonded connections.

1.5 Thesis outline



Chapter 2

Transparent Structural Silicone Adhesive (TSSA)

2.1 Introduction

Transparent Structural Silicone Adhesive or TSSA is a crystal clear, high strength silicone adhesive film produced by the Dow Corning that exhibits thermal stability and excellent weatherability [7]. It was developed with the purpose of realizing steel to glass laminated connections for frameless glazed facade applications. In contrast with SentryGlas®, TSSA is not intended for embedded laminated connections neither to be used as an interlayer between glass panes. It exhibits though significantly higher stiffness and strength compared with standard silicone adhesives used in construction [1]. In the work of Sitte et al. [7], TSSA is described as a very promising adhesive both for interior and exterior applications. It may be used either to connect glass to steel fixings or even for direct glass-to-glass bonding applications.



(a) (b) (c)

Figure 2.1: Dow Corning European Distribution Center in Feluy (Belgium)

TSSA connections have been used in real scale projects in Belgium, Italy, Germany, Poland, Switzer-

land, Japan and United States of America [1]. In all of these projects, TSSA was used to realize steel-to-glass point fixings. An example of a building project where TSSA laminated point connections where used to support the glazed facade panels is the Dow Corning European Distribution Center in Feluy (Belgium). In this project, the laminated TSSA connections allowed a more uniform distribution of stresses in the glass as well as the use of insulating glazed units leading to the elimination of thermal bridges.

2.2 Characteristics and properties of TSSA

2.2.1 Chemical composition and cure chemistry

TSSA is an elastomeric one-component addition cured silicone with no by-products (and no odor), characterized by nanosilica and cross-linked polymers [8]. It has an amorphous structure and crystallizes below -55°C. The adhesive film is cured inside an autoclave at 120 - 135°C for 20-30 minutes. During that period, it is recommended that the adhesive layer is under a pressure of 0.15-1.3MPa, in order to ensure efficient wet-out on the substrate [7, 15]. The curing of TSSA occurs rather rapidly; however, the specimen must stay in the autoclave for at least 1 hour to ensure a homogeneous bond between the glass and steel[7, 1].

2.2.2 Material properties

Table 2.1 provides an overview of the most important physical properties of TSSA. TSSA has a reflective index of 1.41, which is very close to that of glass (1.51 - 1.52) [7]. This renders possible the design of a completely transparent connection between glass and steel. A very important characteristic of TSSA is that it is not significantly affected by temperature variations. The glass transition temperature of the adhesive is expected to be close to -120°C and thus its stiffness is stable against environmental temperature changes [1]. In addition, TSSA exhibits very good performance against UV radiation and shows high weather resistance.

Table 2.1: Typical physical properties of TSSA [7, 15]

Property	Unit	Value
Colour	-	Crystal clear
Specific gravity	g/ml	1.01
Service temperature range	°C	-50 to 150
Glass transition temperature (T_g)	°C	-120
Reflective index (1mm thick film at 589.3nm)	-	1.41
Thermal conductivity	W/(m K)	0.2
Linear thermal expansion coefficient	$10^{-6}K^{-1}$	281

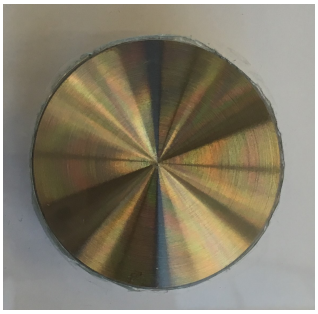


Figure 2.2: TSSA laminated connection as seen through the glass

2.2.3 Mechanical properties

According to the manufacturing company, Dow Corning, the following typical mechanical properties characterize the behaviour of TSSA. The mechanical properties of Table 2.2 refer to uniaxial (ASTM D412[1]) and simple shear (ASTM D3165[2]) tests, as specified by the American Society for Testing and Materials.

Table 2.2: Typical mechanical properties of TSSA (Source: Dow Corning)

Test type	Property	Unit	Value
ASTM D412	Maximum tensile strength	MPa	8.5
ASTM D412	Elongation at maximum tensile	%	250
ASTM D412	Modulus at origin	MPa	9
ASTM D412	Tensile strength at 100% elongation	MPa	4.5
ASTM D3165	Shear strength in lap shear	MPa	5.7
ASTM D3165	Shear modulus in lap shear	MPa	2.5

The characteristic tensile and shear strength of TSSA as cured on stainless steel circular connectors is given in Table 2.3.

Table 2.3: TSSA strength as cured on typical hardware (Source: Dow Corning)

Test type	Unit	Strength
Tensile test - 50 mm button	MPa	4.5
Shear test- 50 mm button	MPa	5

2.2.4 The whitening effect

Tensile tests of TSSA dumbbells and TSSA metal to glass connections [1, 8, 7] have showed that the adhesive does not remain transparent throughout testing. Its colour changes from completely transparent to white after a certain stress level. This whitening of TSSA though develops gradually, a fact

[1]ASTM D412 specifies a standard test method for deriving strength properties of dumbbell shaped adhesive specimens in uniaxial tension.

[2]ASTM D3165 specifies a standard test method for deriving strength properties of adhesives in shear, by tension loading of single-lap-joint laminated assemblies.

which makes it difficult to clearly define the starting point of the phenomenon. Small white spots may be visible at low stress levels which then gradually take over the whole surface of the adhesive. According to the manufacturing company, Dow Corning®, the whitening phenomenon is expected when the local stress exceeds 2MPa [15]. In the work of Santarsiero et al. [8] and Sitte et al. [7], the whitening of TSSA is clearly visible at engineering stress close to 5MPa.

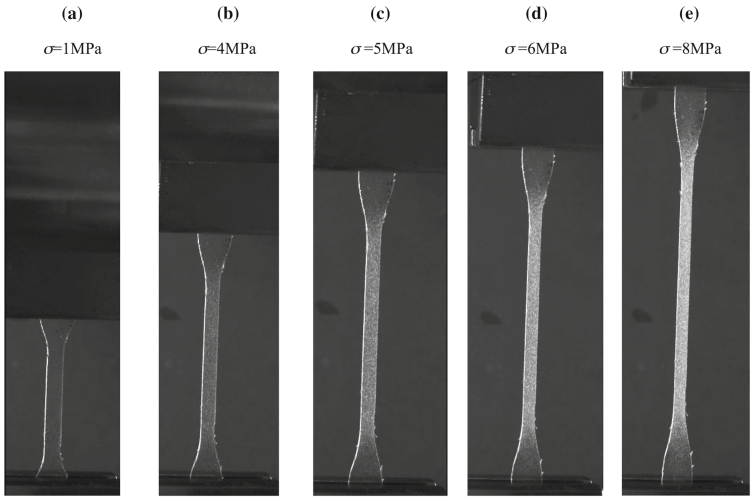


Figure 2.3: Whitening effect of TSSA recorded at different stress levels under uniaxial tensile stress [1, 8]

A theory about the causes of the whitening phenomenon is expressed in the work of Santarsiero [1], where the whitening is attributed to the strain-induced crystallization phenomenon. Transparent polymeric materials have an amorphous non-crystallized structure. However, when they are subjected to tensile forces the polymer chains tend to align with each other and thus favor the development of crystals (also referred to as lamellae). In this case, the light scatters at the boundaries of the lamellae crystals resulting in this white color that is visible during stretching. This phenomenon is more evident under tensile rather then shear loading, because in the latter case polymer chains tend to slide. In the unloaded state, the polymer chain network of amorphous materials may partially or fully recover the initial amorphous state. The degree of recovery depends on the type of polymer.

2.2.5 Design stress

Dow Corning® recommends design stress values for permanent and non permanent loads. In structural engineering, the design values for non permanent loads are often determined based on the yield point, which is the transition point between the elastic and the plastic phase. In the case of TSSA, there is no clear plastic phase. However, Dow Corning® related the yield point to the start of the whitening phenomenon and thus the stress level of 2 MPa is considered as the yield limit for TSSA [15]. According to the recommended safety factor of 1.5 [15], the following design value is proposed:

Design stress for non permanent loads in tension and simple shear [15]:

2MPa / 1.5 = 1.33 MPa

In case of permanent loads, Dow Corning® specifies that TSSA failure might happen after more than 100 years at stress level above 1MPa [15]. The long-term behaviour of TSSA though has not be fully in-

vestigated, as very few tests have been performed under sustained loading[3], and thus further research is required to verify the following design stress level.

Design stress for permanent loads:

1MPa / 1.5 = 0.66 MPa

2.2.6 Fabrication

Dow Corning recommends that TSSA should be applied inside a clean and dust free room and the temperature should range between 15°C and 25°C [15]. The process begins with cleaning the substrates either with isopropanol (IPA) or acetone. The two-cloth cleaning method should be followed, where the substrate is cleaned with a cloth saturated in solvent and then the surface is dried by a separate clean cloth. Clean, soft, absorbent and lint-free cloths should be used for this purpose. For structural applications, it is recommended to apply a primer before lamination. The priming of the substrates must begin immediately after the cleaning process to avoid any dirt accumulation. TSSA must be applied only after the primer has completely dried, which usually takes 5 to 20 minutes.

TSSA is produced in foils with a thickness of 1mm, which are delivered with two protective (PETP) films on both sides. These foils should be stored at low temperatures to prevent curing of the adhesive [1]. After priming the surfaces [4], the TSSA foil is taken out of the refrigerator, and is maintained at room temperature until all condensation at its surface is removed. When TSSA has dried completely, the foil may be cut into the desired size. First, one of the protective films is removed and the TSSA foil is applied on the stainless steel connector. Subsequently, the second film is removed and TSSA is applied on the glass surface. During this process, touching the surface of TSSA should be avoided. After the application of TSSA, Dow Corning recommends a pre-pressure of 0.15 to 1.3 MPa [7, 15]. Afterwards, the film adhesive is cured at temperatures of 120-140 °C inside an autoclave. Optimum cure conditions are achieved in autoclaves, but alternative production methods such as pre-pressure (prior to heat cure) followed by oven curing or vacuum-bagging (during heat cure) may also result in good quality connections. It strongly depends on the design of the connection and the ability to eliminate air bubbles [5].



Figure 2.4: Fabrication of TSSA laminated circular connections [15]

[3] Sitte et al. [7] performed sustained loading tests in circular connections with a diameter 20mm at a constant load of 1.25 MPa and 0.63 MPa. The specimens exposed to 1.25 MPa load failed, on average, after 7 years. The specimens loaded with 0.63 MPa have not failed after 11 years of sustained loading (as the time of this publication).

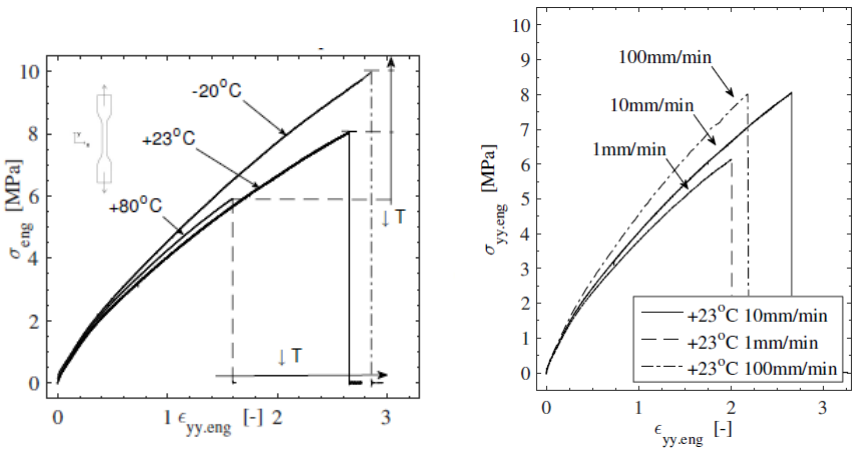
[4] Dow Corning recommends to use the DOW CORNING(R) 92-023 PRIMER (87% (w/w) heptane, 7.8% allyltrimethoxysilane, 5% titanium tetrabutanolate).

[5] Dow Corning Europe, personal communication on 23rd May 2017.

2.3 Studies on TSSA laminated connections

In the work of Sitte et al. [7], the tensile and shear monotonic behavior of TSSA connections is investigated at room temperature. In addition, the behaviour of TSSA bulk material is also investigated at room temperature and at a constant displacement rate. The results of this study showed that TSSA exhibits a hyperelastic behaviour. Cyclic loading tests were also performed and preliminary results showed the appearance of the stress softening phenomenon. On the other hand, Watson and Overend [16] tested TSSA single lap joints and T-peel specimens. The experimental results showed that TSSA exhibits sufficient strength in combination with a flexible behavior which is unique among other transparent heat-curing foils, such as SentryGlas.

In the work performed by Santarsiero [1], TSSA dumbbell shaped specimens are subjected to uniaxial tensile tests. The tests were performed at different temperatures (-20°C, 23°C and 80°C) and displacement rates (1mm/min, 10mm/min and 100mm/min). Figure 2.5 a illustrates the stress-strain curve derived from these tests at different temperatures. A linear behaviour is observed for stress levels up to 2MPa [1] and then the response becomes nonlinear until failure. The stress-strain graph confirms the hyperelastic nature of TSSA. As expected, the stiffness of the material is not significantly influenced by temperature at small stresses and strains, since the glass transition temperature is above the investigated temperatures. However, the stress and strain at the point of failure showed a temperature dependency. The stress level at failure is higher as the temperature decreases and the same observation is made for the strains. The graph provided in Figure 2.5(b) shows the dependency on the displacement rate of the stress-strain curve at 23°C. At higher rates of 10mm/min and 100mm/min, the maximum stresses are larger compared with the 1mm/min rate. Event though, the behaviour of TSSA shows a displacement rate dependency, more tests are needed in order to form more solid conclusions [1].



(a) (b)

Figure 2.5: Uniaxial tensile test results: (a) temperature effect and (b) displacement rate effect [1]

Table 2.4 summarizes the mechanical properties and the maximum stresses and strains [6] observed in uniaxial tension tests performed by Santarsiero [1] under different temperatures and displacement rates.

[6] Results are given in terms of engineering and true stresses and strains (refer to Section 3.2)

Table 2.4: Uniaxial test results of TSSA dumbbells at different temperatures and engineering strain rates [1]

T (^{o}C)	$\dot{d}$ (mm/min)	$\dot{\varepsilon}$ (-/sec)	E (MPa)	v (-)	$\sigma_{yy,max}$ (MPa)	$\sigma_{yy,max,true}$ (MPa)	$\varepsilon_{yy,max}$ (MPa)	$\varepsilon_{yy,max,true}$ (MPa)
80	1	4E-04	6.79	0.46	5.00	10.91	1.33	0.85
23	1	4E-04	6.23	0.44	6.13	15.89	1.99	1.09
-20	1	4E-04	6.39	0.46	7.52	23.39	2.21	1.17
80	10	4E-03	6.95	0.45	6.06	14.68	1.60	0.95
23	10	4E-03	6.45	0.44	7.87	21.31	2.58	1.28
-20	10	4E-03	6.57	0.44	9.57	31.70	2.82	1.34
23	100	4E-02	7.1	0.44	8.02	22.8	2.13	1.11

Figure 2.6 illustrates graphically the effect of temperature on the E modulus and the Poisson's ratio. It is evident that E and v are not influenced significantly by temperature variations.

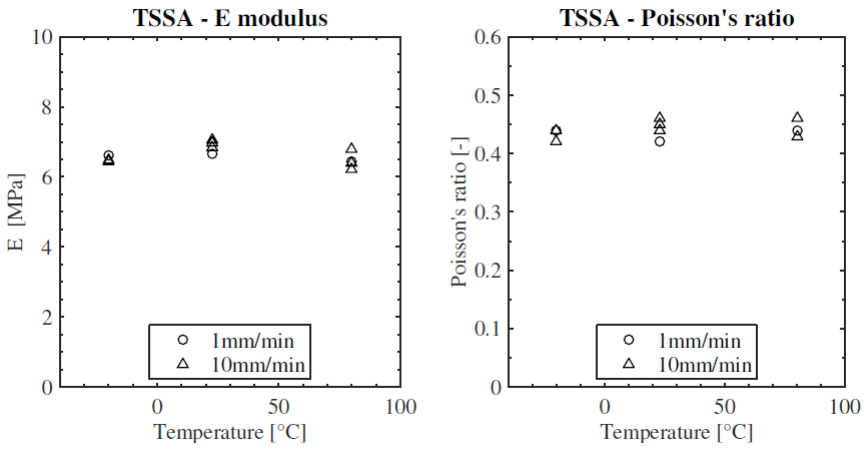


Figure 2.6: E-modulus and Poisson ratio under the influence of temperature and displacement rate [1]

Santarsiero [1, 17] also performed shear and tensile tests on TSSA laminated circular connections. The specimens consisted of 150 x 150 mm glass plates with a laminated stainless steel circular button of diameter 50 mm. The shear behaviour of such connections proved to be mainly linear until failure, a fact which was also observed in the work of Sitte et al. [7] and Hagl et al. [9]. The connection exhibits quite a flexible shear behaviour with maximum displacement at approximately 3 mm. The influence of temperature on the shear behaviour of the connection is negligible, as the curves of Figure 2.7, representing different temperature states, almost overlap. However, there is a temperature influence on the maximum stress, which increases as the temperature decreases. The failure mode was fully cohesive and glass failure did not occur [1].

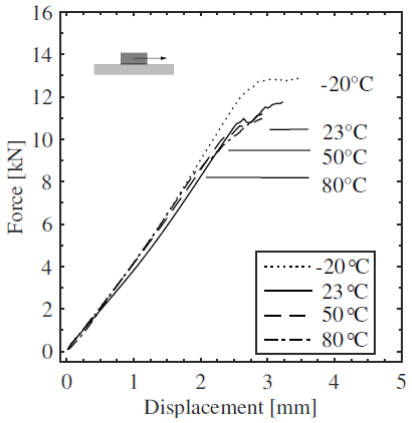


Figure 2.7: Shear test results of TSSA laminated connections - temperature effect [1]

Table 2.5: Shear test results of TSSA laminated circular connections [1]

T (^{o}C)	n. tests (-)	$\dot{d}$ (mm/min)	$\dot{\gamma}$ (-/sec)	F_v (KN)	$\sigma_{eng,v}$ (MPa)
-20	3	1	1.2E-02	12.96	6.60
23	1	0.1	1.2E-03	9.32	4.75
23	5	1	1.2E-02	10.42	5.31
23	1	10	1.2E-01	11.86	6.04
50	1	0.1	1.2E-03	9.15	4.66
50	3	1	1.2E-02	9.65	4.91
50	1	10	1.2E-01	9.79	4.99
80	1	0.1	1.2E-03	7.22	3.68
80	3	1	1.2E-02	8.17	4.16
80	1	10	1.2E-01	8.90	4.53

On the other hand, the mechanical response of laminated circular connections under tensile load appears to be bilinear (see Figure 2.8). The first phase of the force-displacement curve shows very high stiffness and is not influenced by temperature variations or by the displacement rate. The second phase is characterized by an approximately linear behaviour. The influence of temperature is expected to be minimum, since the glass transition temperature is at -120^{o}C. This can be observed from the graph as most the curves are very slightly offset depending on the tested temperature [1, 18].The maximum load and displacement show a temperature dependency, with higher values observed at lower temperatures (see the left graph of Figure 2.8). Figure 2.8 (right) illustrates the effect of displacement rate on the tensile behaviour of the connection. According to the results, even though the shape of the curve is not significantly affected by the different displacement rates, the maximum load and displacements appear to be affected by this parameter. Higher failure loads (F_N) are observed when the specimens are subjected to higher loading rates and vice versa. During the tensile tests, the whitening phenomenon made its appearance at a certain load level (F_w) [1]. Table 2.6 provides the recorded load levels where whitening appeared for the first time. The values are dependent on temperature and strain rate [1].

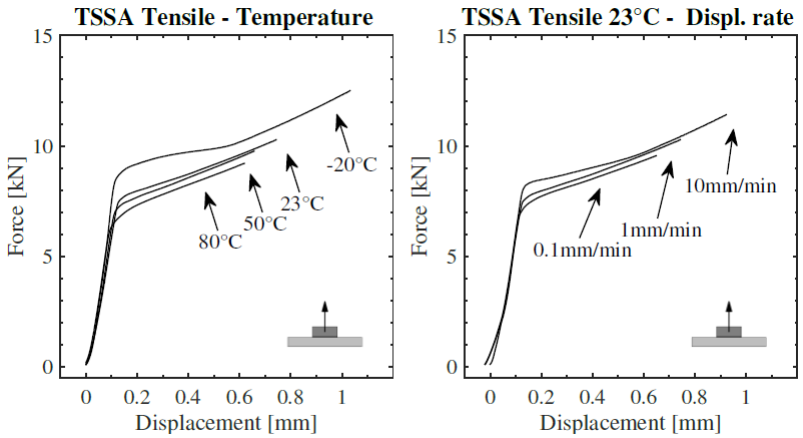


Figure 2.8: Tensile test results of TSSA laminated connections - temperature (left) and displacement rate (right) effect [1]

Table 2.6: Tensile test results of TSSA laminated circular connections [1]

T (^{o}C)	n. tests (-)	$\dot{d}$ (mm/min)	$\dot{\varepsilon}$ (-/sec)	F_w (KN)	$\sigma_{eng,w}$ (MPa)	F_N (KN)	$\sigma_{eng,N}$ (MPa)
-20	3	1	1.2E-02	6.8	3.46	12.46	6.35
23	1	0.1	1.2E-03	4.48	2.28	10.25	5.22
23	5	1	1.2E-02	4.63	2.36	10.8	5.50
23	1	10	1.2E-01	6.1	3.11	11.42	5.82
50	1	0.1	1.2E-03	3.91	1.99	9.27	4.72
50	3	1	1.2E-02	4.52	2.3	9.82	5.00
50	1	10	1.2E-01	5.3	2.70	10.97	5.59
80	1	0.1	1.2E-03	3.8	1.94	9.24	4.71
80	3	1	1.2E-02	4.07	2.07	9.49	4.83
80	1	10	1.2E-01	4.91	2.50	9.93	5.06

2.4 Standard specifications and norms

Several International and European standard specifications exist for the design of structural glazing systems that make use of silicone sealants. Silicone adhesives used in building construction must be approved to carry the design loads and to be in accordance with the serviceability limit states described in these standards. More specifically, one of the following standards may be used to design silicone sealant connections for structural glass components; ASTM C1184-05 Standard Specification for Structural Silicone Sealants [19], ETAG 002 Guideline for European Technical Approval for Structural Sealant Glazing Systems [20] or EN 15434 : 2006 + A1:2010 Glass in building-Product standard for structural and/or ultraviolet resistant sealant [21]. These standards were developed for cold applied chemically curing structural silicone sealants [7] and thus they do not provide any provisions for heat-curing adhesives such as TSSA. Even though TSSA applications are not covered by these standards,

based on tests performed by Sitte et al. [7], the adhesive is expected to pass the durability aspects[7].

[7] Sitte et al. [7] performed tensile tests on circular connections (with diameter 20 mm) exposed to hot water (at 50^{o}C for 8 weeks), to accelerated weathering (12,200h in an Ultraviolet Condensation Weathering Device with UV-A 340) and to outdoor weathering (36 months is Chiba, Japan). The results showed a 25% decrease of the tensile strength of the specimens immersed into hot water. Specimens subjected to accelerated weathering showed a 11% decrease of the initial strength, whereas specimens subjected to outdoor weathering for 36 months, showed a 5% increase of the initial tensile strength.

Chapter 3

Analysis of hyperelastic materials

3.1 Introduction

Rubber materials consist of long chain molecules, also known as polymers [22]. The mechanical behaviour of rubbers, or in other words of elastomers, includes large deformations, viscoelastic effects and stress-softening under loading cycles [23]. The material nonlinearities constitute very difficult the analytical calculation of rubber structures. These days, finite element software allow the simulation of rubbers and conduct in minimum amount of time the computationally complex calculations to derive the stress state of such materials. The mechanical response of elastomers is expressed by a broad amount of hyperelastic laws, most of which are currently supported by finite element software.

This chapter provides the fundamental theory for the analysis of hyperelastic materials. In Sections 3.4 and 3.5, an overview of various hyperelastic laws is provided and the most commonly used material models are further discussed. Finally, the way of modeling the specific case of stress softening effects under cyclic loading is explained in Section 3.6.

3.2 Finite deformation theory

A simplified assumption considers rubber materials as linearly elastic at small strains. However this assumption does not apply for larger strains, where the difference between the cross sectional area in the deformed and non-deformed state is not negligible [8]. Therefore, the finite elastic deformation theory is more suitable for the analysis of rubber structures [22]. The finite deformation theory implies that the actual (or true) stress and the actual (or true) strain are defined by the actual (deformed) length or cross sectional area. This does not apply to the infinitesimal theory, where the engineering stresses and strains are calculated based on the non-deformed state. Based on the infinitesimal theory, which is mostly applied in civil engineering practice, the (engineering) stress and strains are calculated as follows:

$$\sigma_{eng} = \frac{F}{A_o} \tag{3.1}$$

$$\epsilon_{eng} = \frac{\Delta l}{l_o} \tag{3.2}$$

Where:

A_o the original cross sectional area
l_o the original length (or thickness)

On the other hand, the (actual) stresses and strains based on the finite deformation theory are calculated as follows:

$$\sigma_{true} = \frac{F}{A} \tag{3.3}$$

$$\epsilon_{true} = \int \frac{\partial l}{l_o} = ln\left(\frac{l}{l_o}\right) = ln\left(1 + \frac{\Delta l}{l_o}\right) = ln\left(1 + \epsilon_{eng}\right) \tag{3.4}$$

Where:

A the actual cross sectional area
l the current length (or thickness)

3.3 The Mullin's effect - stress-softening phenomenon

3.3.1 Overview of the stress-softening effect

Rubber-like materials and more specifically filled rubbers and crystallizing pure gums undergo a stress softening phenomenon under cyclic loading. More specifically, they exhibit a hysteretic behaviour which is characterized by a difference between the loading and unloading mechanical response. This softening effect, also referred to as the Mullins effect, was first extensively studied by Mullins [10] almost 50 years ago. Since then, scientists have not reached to a general agreement on the physical explanation or the mechanical modeling of this phenomenon [24]. However, it is widely accepted that it is related to the previously applied maximum stress, since similar softening behaviour is observed when rubbers are stretched up to the same stress level [24]. Furthermore, the stress-softening effect is considered to be closely related to the fatigue behaviour and thus to the life expectancy of rubber materials [22].

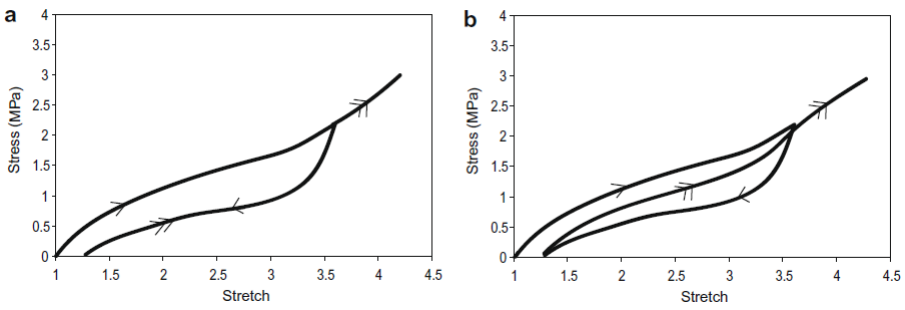


Figure 3.1: Model representation of the stress-softening behavior of rubber-like materials [24]

Figure 3.1 shows two basic representations of the stress-softening behaviour of rubbers. In the first case (see Figure 3.1(a)) , the second loading coincides with the unloading curve and this is often referred to as "the ideal Mullins effect" [24], whereas Figure 3.1(b) shows the case when the reloading diverges from the unloading curve.

The Mullins effect has been observed in many deformation states of rubbers such as uniaxial tension, uniaxial compression, simple shear and equibiaxial tension. However, it is still subject of research which of the above mechanical quantities pilots the phenomenon [24]. The lower stress limit where the phenomenon starts to develop is also not quite clear and seems to vary depending on the material tested.

Extensive research has been performed to investigate the correlation between the Mullins effect and strain-induced crystallization. Strain-induced crystallization occurring in many rubber-like materials (see Section 2.2.4) does not seem to be affected by the stress softening effect [24]. Mullins [12] also studied the permanent deformations after stretching and releasing pure and filled natural rubbers. He noticed that the permanent set, caused by viscoelastic effects, recovered rapidly after a certain release time. In addition, he noted that materials that show little softening exhibit little residual deformations [24].

Healing of the Mullins effect has been recorded for several types of rubbers. The healing is related either to the recovery of the permanent deformations, the return to the initial stress levels for a fixed strain or even the recovery of the complete stress-strain response [24]. In his work, Mullins[1] [11] showed that there is a temperature dependency of the recovery of the stress softening phenomenon. At room temperature very little recovery was observed, whereas at high temperatures, such as 100°C, the softening was recovered up to 80% [24]. Further research was implemented by Harwood and Payne[2] [25], who observed that the level of recovery of the Mullins effect depends on the type of cross-linking of the material [24] and thus rubbers may exhibit either partial or full recovery of their response.

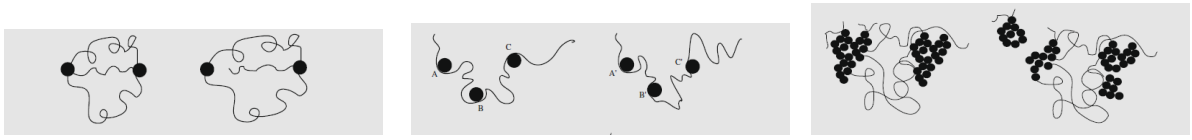
3.3.2 Physical interpretations

Several physical interpretations have been proposed in order to understand the stress-softening phenomenon of rubbers. However, there is still no agreement on the origin of this phenomenon [24]. Blanchard and Parkinson [26] expressed the theory that the stress-softening effect is the result of bond ruptures taking place during stretching. According to their theory, the weaker bonds (or physical bonds) are ruptured first, followed by the stronger (or chemical) bonds. On the other hand, Houwink [27] rejected this theory as it is not in line with the ability of the adhesive to slowly recover its behaviour at room temperature. If the phenomenon is caused by the rupture of rubber bonds than the damage is expected to be permanent. Therefore, Houwink explained the theory of molecules slipping over the surface of fillers, a fact which causes new bonds to be created. These new bonds are of the same physical nature as the previous ones, but they are located at different places along the rubber molecules [24]. According to this theory, the phenomenon could be reversible with exposing the rubber at elevated temperatures. Dannenberg and Brennan [28] conducted tests to measure any changes in the network density when subjecting rubbers to loading cycles. No significant change of the network density was observed, while significant stress-softening was taking place. Therefore, they adhered to Houwink's theory. However, they also accepted that irreversible stress-softening could be the consequence of bond breakage. Other theories have been developed by Kraus et al. [29] who attribute the

[1] Mullins investigated the recovery of unfilled natural rubbers stretched up to 420% [24, 11].

[2] Harwood and Payne studied the recovery of the Mullins effect in unfilled vulcanizates natural rubber considering the type of cross-linking as an important factor [25, 24].

stress-softening effect to the rupture of carbon-black structure, which is used as reinforcing filler in many rubber products. However, this theory has not been adopted by many researchers, as such a process is expected to be irreversible and thus there is no compatibility with the ability of rubbers to recover their response [24].



(a) Bond rupture (b) Molecules slipping (c) Filler rupture

Figure 3.2: Physical explanations of the Mullins effect [24]

3.4 Fundamental theory of constitutive models

Nonlinear elasticity problems are often solved using strain energy functions and most of the constitutive models, for rubber-like materials, are expressed as a function of the deformation gradient tensor.

$$W = f(F) \tag{3.5}$$

Where:

W the strain energy density (or potential) or the strain per unit of reference volume volume
F the deformation gradient tensor

The deformation gradient tensor F separates rigid body translations from deformations which are the cause of stress. If x is the deformed vector and X is the reference vector of a specific point P of the rigid body, then:

$$F = \frac{\partial x_i}{\partial X_j} = \begin{bmatrix} \frac{\partial x_1}{\partial X_1} & \frac{\partial x_1}{\partial X_2} & \frac{\partial x_1}{\partial X_3} \\ \frac{\partial x_2}{\partial X_1} & \frac{\partial x_2}{\partial X_2} & \frac{\partial x_2}{\partial X_3} \\ \frac{\partial x_3}{\partial X_1} & \frac{\partial x_3}{\partial X_2} & \frac{\partial x_3}{\partial X_3} \end{bmatrix} \tag{3.6}$$

By defining the displacement of point P as $u = x - X$, the deformation tensor can also be written as:

$$F = \frac{\partial}{\partial X}(X + u) = \frac{\partial X}{\partial X} + \frac{\partial u}{\partial X} = I + \frac{\partial u}{\partial X} \tag{3.7}$$

Most rubber-like materials have a Poisson's ratio very close to 0.5; however, it is not correct to assume that their behaviour is incompressible. Rubbers still exhibit volume changes especially when they are under a confined state. For this reason, the strain energy function often breaks down to an isochoric and a volumetric part. The decoupled strain energy function is written as follows.

$$W(F) = W_{iso}(\overline{F}) + W_{vol}(J) \tag{3.8}$$

Where:

$W_{iso}(\overline{F})$	the isochoric part of the strain energy function, corresponding to the case of perfect incompressibility
$W_{vol}(J)$	the volumetric part of the strain energy function, accounting for volume changes

In this case, the deformation gradient is written as follows:

$$F = J^{\frac{1}{3}}\overline{F} \tag{3.9}$$

Where:

J	the Jacobian of the deformation gradient tensor ($J = det(F)$)
$\overline{F}$	the volume-preserving deformation gradient tensor

Isochoric part - Incompressibility assumption

The vast majority of hyperelastic material models are based on the assumption of incompressibility and thus are based on the volume-preserving deformation tensor $\overline{F}$. A model that is solely based on this assumption can only be considered acceptable for non-confined cases, such as uniaxial tension or compression, simple shear and biaxial stress states. Furthermore, most finite element codes express the strain energy function in terms of the left Cauchy-Green tensor $\overline{B}$, due to its symmetric nature[3]. The left Cauchy-Green deformation tensor is:

$$B = \overline{FF}^T \tag{3.10}$$

The above deformation tensor admits the principal invariants $\overline{I}_1, \overline{I}_2$ and $\overline{I}_3$, which are calculated based on Equations 3.11,3.12 and 3.13 respectively. Based on the assumption of incompressibility, the third invariant is equal to 1.

$$\overline{I}_1 = tr(\overline{B}) \tag{3.11}$$

$$\overline{I}_2 = \frac{1}{2}[tr(\overline{B})^2 - tr(\overline{B}^2)] \tag{3.12}$$

$$\overline{I}_3 = det\overline{B} = 1 \tag{3.13}$$

The invariants can also be given in terms of the principal extension rations λ_1, λ_2 and λ_3 of the deformation gradient tensor.

$$\overline{I}_1 = \lambda_1^2 + \lambda_2^2 + \lambda_3^2 \tag{3.14}$$

$$\overline{I}_2 = \lambda_1^2\lambda_2^2 + \lambda_2^2\lambda_3^2 + \lambda_3^2\lambda_1^2 \tag{3.15}$$

[3]The left Cauchy-Green tensor is symmetric because the product of any matrix with its transpose is always symmetric.

$$\overline{I}_3 = \lambda_1^2 \lambda_2^2 \lambda_3^2 = 1 \tag{3.16}$$

Taking into consideration the physical interpretation of the invariants, $\overline{I}_1$ is related to the hydrostatic and $\overline{I}_2$ to the deviatoric component of the green deformation tensor[4]. The third invariant, $\overline{I}_3$, represents the ratio of the deformed to initial volume ($det\left(\overline{F}\right) = V_{\overline{F}}/V_o$), which is 1 for perfectly incompressible materials.

Therefore, most hyperelastic models that are based on the incompressibility assumption are expressed as a function of the first two principal invariants ($\overline{I}_1, \overline{I}_2$) or of the principal extension ratios ($\lambda_1, \lambda_{2,}\lambda_3$).

$$W_{iso}(\overline{F}) = W_{iso}(\overline{I_1}, \overline{I_2}) = W_{iso}(\lambda_1, \lambda_{2,}\lambda_3) \tag{3.17}$$

Marckmann and Veron [30] compared twenty hyperelastic models for rubber-like materials and classified the models into three basic categories based on the expression of the strain energy function.

- The phenomenological models that provide a mathematical framework for describing the mechanical behaviour of elastomers based on continuum mechanics. The determination of the material parameters is difficult and these models may prove to be inaccurate for large deformations out of the predefined range of the model. Since they are in essence empirical expressions, they lack a physical interpretation [31].
- The models that express the material behaviour directly from the functions $\frac{\partial W}{\partial I_1}$ and $\frac{\partial W}{\partial I_2}$ based on experimental data.
- The physical (or micro-mechanical) models that are based on physics of polymer chains and on statistical and kinetic theory. These models derive elastic properties from an idealized model of the structure [32]. The strain energy function is formed based on microscopic phenomena. The mathematical formulation of most physical models is quite complicated.

The first two categories are both based on continuum mechanics theory and thus the above categorization can be simplified into phenomenological and physical models. Figure 3.3 shows the most commonly used hyperelastic models, along with their parameters, to describe the mechanical response or rubber-like incompressible materials. This study approaches the problem from a continuum mechanics point of view and thus focuses only on phenomenological models. These will be further discussed in Section 3.5.

[4]Every strain tensor can be subdivided into a hydrostatic and a deviatoric component. The summation of those strain tensors gives the original tensor back. The hydrostatic strain is related to volume change and the deviatoric strain is related to the deformation at constant volume.

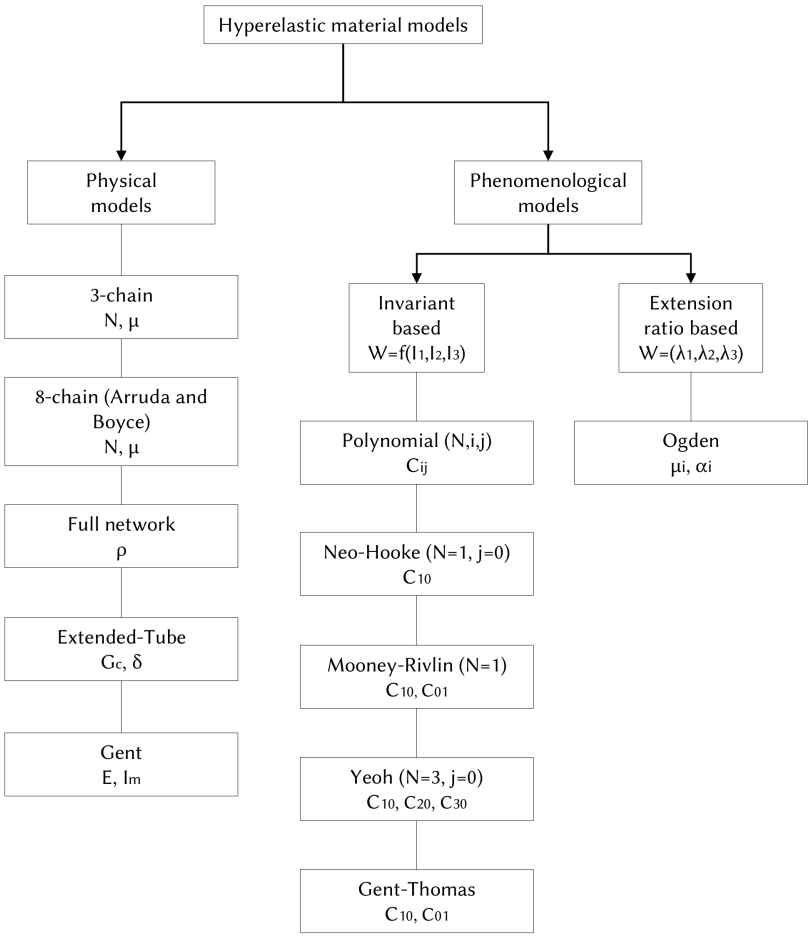


Figure 3.3: The most commonly used physical and phenomenological models for incompressible materials

The results of a finite element analysis largely depend on the appropriateness of the chosen hyperelastic model. The suitability of a model depends on the type of application, the corresponding variables and the available data [22]. In the work of Chagnon et al. [23], the efficiency of a hyperelastic model is described by four main aspects [22]:

- It should be able to recreate an S-shaped stress-strain graph, if this is the case.
- It should be considerably accurate for all modes of deformation (e.g. uniaxial, shear, equibiaxial).
- The number of material parameters should be limited, in order to decrease the required number of tests.
- The mathematical formula should stay simple and practical.

Volumetric part - Extension to compressibility

Perfect incompressibility means that the material exhibits zero volumetric changes under hydrostatic pressure. Practically there is no material that can be considered perfectly incompressible; however, most rubbers are characterized by "near incompressibility", meaning that their Poisson's ratio is very close to 0.5. In literature, one can find several models that describe volumetric changes of rubbers and which are expressed as a function of the jacobian J of the deformation gradient tensor. These models consist of a single material constant which is the bulk modulus of the adhesive. In order to properly define the bulk modulus of rubbers, oedometric test are needed [3]. An oedometric test requires inserting a piece of the adhesive, often a circular specimen, inside a rigid matrix in order to achieve a perfectly confined state by fully restraining lateral expansion. Subsequently, the upper part of the adhesive is compressed with the help of a piston in order to impose a hydrostatic stress state to the adhesive. During this process, stress and strain data are kept for the determination of the bulk modulus.

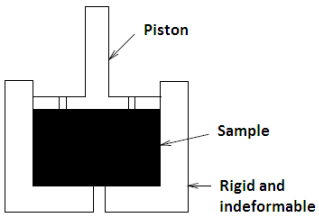


Figure 3.4: Oedometric test scheme [3]

3.5 Phenomenological models

In this section, the most widely used phenomenological models are presented and discussed with regard to their strengths and weaknesses. It must be noted that the basic theory of nonlinear elasticity describes the material response under static loading. Based on this theory several models have also been developed that describe viscoelastic and stress softening phenomena [30]; however, these are extensions of the fundamental theory and will be further discussed in Section 3.6.

3.5.1 Polynomial model

The phenomenological theory expressed by Rivlin was based on the assumption that elastomers with elastic behaviour are isotropic and quasi incompressible [31, 33]. This theory was developed based on a previous phenomenological theory proposed by Rivlin, which considers isotropic behaviour and near incompressibility of rubber materials [22]. The polynomial model of the strain energy function for rubber materials is given in Equation (3.18) and forms the base for other hyperelastic models.

$$W = \sum_{i+j+k=1}^{N} C_{ijk}(I_1 - 3)^i \cdot (I_2 - 3)^j \cdot (I_3 - 1)^k \tag{3.18}$$

If the material is considered incompressible, as is the case for most rubbers, then I_3 is equal to 1 and (3.19) becomes:

$$W_{iso} = \sum_{i+j=1}^{N} C_{ij}(\overline{I}_1 - 3)^i \cdot (\overline{I}_2 - 3)^j \tag{3.19}$$

Where C_{ij} are coefficients that describe the shear behaviour of the material [22] and their number depends on the degree N of the polynomial [31]. They are rarely more than 3, because then the determination of the material parameters becomes more complex [31, 34]. This mathematical formulation of the strain energy function is mainly used for very large strain problems [30].

The complete expression of the model, also including volumetric changes, is given in Equation (3.20).

$$W(\overline{I}_1, \overline{I}_2, J) = \sum_{i+j=1}^{N} C_{ij}(\overline{I}_1 - 3)^i \cdot (\overline{I}_2 - 3)^j + \sum_{i=1}^{N} \frac{1}{D_i}(J-1)^{2i} \tag{3.20}$$

Where:

C_{ij}	material parameters related to the isochoric part of the strain energy function
J	the Jacobian of the deformation gradient tensor ($J = det(F)$), or the volume ratio (V_F/V_0)
D_i	material parameter that controls the bulk compressibility of the material $D_i = 2/K$, where K is the bulk modulus of the material
N	number of terms of the strain energy function

3.5.2 Mooney-Rivlin

The Mooney-Rivlin hyperelastic material model is a special form of the basic polynomial model, for N=1 polynomial degree [31]. The strain energy function of this model is given in Equation (3.21), where C_{10} and C_{01} are the material parameters [31, 35]. In the work of Marckmann et al. [30], the Mooney-Rivlin theory is considered appropriate for rubbers exhibiting moderate deformations (lower than 200%) . Moreover, it has been proven inadequate to describe the compression mode of deformation as well as to account for hardening of the material [36].

$$W_{iso} = C_{10}(\overline{I}_1 - 3) + C_{01}(\overline{I}_2 - 3) \tag{3.21}$$

The complete expression of the model, also including volumetric changes, is given in Equation (3.22).

$$W(\overline{I}_1, \overline{I}_2, J) = C_{10}(\overline{I}_1 - 3) + C_{01}(\overline{I}_2 - 3) + \frac{1}{D_1}(J-1)^2 \tag{3.22}$$

3.5.3 Neo-Hookean

The Neo-Hookean hyperelastic model is a special case of the Mooney-Rivlin model, where C_{01} is equal to zero and thus the strain energy function depends only on the first invariant $\overline{I}_1$[31]. It is the simplest hyperelastic model and it is applicable in cases when few test data are available, such as only from one test configuration [31]. Even though a single test is needed to determine the material response, the model is not able to accurately describe the behaviour in other modes such as other multi-parameter

models; however, it can still provide a good approximation[22, 37]. In addition, due to its simplified formula, this model does not accommodate differences in curvature and therefore cannot describe an S-shaped stress-deformation diagram. According to Steinmann et al. [38] the model describes experimental data fairly accurate for small deformations in uniaxial tension (λ) and simple shear up to 1.5 and 1.9, respectively .

$$W_{iso} = C_{10}(\overline{I}_1 - 3) \tag{3.23}$$

The complete expression of the model, also including volumetric changes, is given in Equation (3.24).

$$W(\overline{I}_1, \overline{I}_2, J) = C_{10}(\overline{I}_1 - 3) + \frac{1}{D_1}(J-1)^2 \tag{3.24}$$

3.5.4 Reduced polynomial model - Yeoh

The Yeoh model [39]comes from a reduction of the basic polynomial model, because the strain energy function depends only in the first invariant $\overline{I}_1$ and consists of the first three terms of the infinite sum of the polynomial function. This model is suitable to describe large deformations [31] and predicts the stress-strain behaviour of different deformation states from test data coming only from uniaxial tension data [40]. However, the performance of the Yeoh model at low strains must be carefully examined [39]. The mathematical expression of the reduced polynomial and Yeoh models are given in Equations (3.25) and (3.26), respectively.

$$W_{iso} = \sum_{i=1}^{\infty} C_{i0}(\overline{I}_1 - 3)^i \tag{3.25}$$

$$W_{iso} = C_{10}(\overline{I}_1 - 3) + C_{20}(\overline{I}_1 - 3)^2 + C_{30}(\overline{I}_1 - 3)^3 \tag{3.26}$$

The complete expression of the Yeoh model, also including volumetric changes, is given in Equation (3.27).

$$W(\overline{I}_1, \overline{I}_2, J) = C_{10}(\overline{I}_1 - 3) + C_{20}(\overline{I}_1 - 3)^2 + C_{30}(\overline{I}_1 - 3)^3 + \sum_{i=1}^{3} \frac{1}{D_i}(J-1)^{2i} \tag{3.27}$$

3.5.5 Ogden

The Ogden model for describing hyperelastic stress-strain behaviour is not based on the invariants of the stress tensor, as the previously mentioned models, but on the principal extension ratios λ_1, λ_2, λ_3. This model is suitable and most widely used for describing large strains, up to 700% [36], and becomes more accurate with large experimental data from multiple test configurations [31, 22, 30]. The strain energy function based on the Ogden theory is given in Equation (3.28), where λ_i the principal extension ratios according to the main axes. The coefficients μ_i and α_i are material parameters which are determined by experimental tests. In addition, the Ogden model has to meet the stability condition $\mu_i \alpha_i > 0$ [31]. In the work of Marckmann and Verron [30] it is stated that the strain energy function with three terms (N=3) can describe accurately an S-shaped stress-strain behaviour [31].

$$W_{iso} = \sum_{i=1}^{N} \frac{2\mu_i}{\alpha_i^2}(\lambda_1^{ai} + \lambda_2^{ai} + \lambda_3^{ai} - 3) \tag{3.28}$$

The Neo-Hookean model is a specific form of the Ogden model for N=1 and $\alpha_1 = 2$. This specific case is described by Equation (3.29), where the coefficient C_{10} is equal to $\mu_1/2$.

$$W_{iso} = \frac{\mu_1}{2}(\lambda_1^2 + \lambda_2^2 + \lambda_3^2 - 3) = C_{10}(I_1 - 3) \tag{3.29}$$

The Mooney-Rivlin model is also a specific form of the Ogden model for N=2, $\alpha_1 = 0$ and $\alpha_2 = -2$. This form is described in Equation (3.30), where $C_{10} = \mu_1/2$ and $C_{01} = -\mu_2/2$.

$$W_{iso} = \frac{\mu_1}{2}(\lambda_1^2 + \lambda_2^2 + \lambda_3^2 - 3) - \frac{\mu_2}{2}(\lambda_1^2 + \lambda_2^2 + \lambda_3^2 - 3) = C_{10}(I_1 - 3) + C_{01}(I_2 - 3) \tag{3.30}$$

The complete expression of the Ogden model, also including volumetric changes, is given in Equation (3.31).

$$W(\lambda_1, \lambda_2, \lambda_3, J) = \sum_{i=1}^{N} \frac{2\mu_i}{\alpha_i^2}(\lambda_1^{ai} + \lambda_2^{ai} + \lambda_3^{ai} - 3) + \sum_{i=1}^{N} \frac{1}{D_i}(J-1)^{2i} \tag{3.31}$$

3.5.6 Gent-Thomas

The phenomenological model proposed by Gent and Thomas [41] has the same material constants as the Mooney-Rivlin model, with the only difference that the natural logarithm is included in the second term. Since it does not include higher terms of I_1, it is not suitable for predicting large deformations [31], as the Yeoh model, but it is considered fairly accurate at small strains.

$$W_{iso} = C_{10}(\overline{I}_1 - 3) + C_{01} ln(\frac{\overline{I}_2}{3}) \tag{3.32}$$

The complete expression of the Gent-Thomas model, also including volumetric changes, is given in Equation .

$$W(\overline{I}_1, \overline{I}_2, J) = C_{10}(\overline{I}_1 - 3) + C_{01} ln(\frac{\overline{I}_2}{3}) + \frac{1}{D_1}(J-1)^2 \tag{3.33}$$

3.6 Mechanical modeling of the stress-softening effect

In literature, several continuum mechanics and pseudo-elastic models exist that describe the stress-softening phenomenon observed in elastomers. In practice, few of them are used and are commercially available in finite element analysis software. Such modes were proposed by Simo [42], Govindjee and Simo [43], Ogden and Roxburgh [44], Chagnon et al. [23], Qi and Boyce [45] and many more. It must be noted that these models can describe only a small fraction of the structural properties of elastomers

[46], since the mechanical response of these materials changes constantly with the number of cycles. Before proceeding to the mechanical modeling of the Mullins effect, it is important to mention the limitations of hyperelastic material models for describing stress-softening phenomena [46]:

1. The stress-strain functions are stable, meaning that they do not change with repetitive loading.
2. The stress-strain function cannot be altered based on the maximum stress experienced.
3. The models assume that the material exhibits a perfectly elastic behaviour and thus there is no provision for permanent deformations.
4. If the adhesive can heal, there is no provision for recovery of the mechanical response.

Most finite element software make use of pseudo-elastic material models to describe stress-softening phenomena of elastomers. Models based on continuum mechanics are considered complex and computationally demanding. On the other hand, pseudo-elastic models use the theory of pseudo-elasticity to describe the loading path with a common strain energy function (see Section 3.5) and the unloading and reloading paths with a different strain energy function that is based on the undamaged situation.

3.6.1 Ogden-Roxburgh

The most commonly used model in finite element codes that considers cyclic stress-softening effects is based on the Ogden and Roxburgh model [44]. This model introduces a scalar variable η that ranges between 0 and 1. This variable represents the damage caused by the Mullins effect. In the undamaged situation (1^{st} loading) η is equal to 1. The constitutive material law is described by function (3.34). It must be noted that this variable does not affect the hydrostatic (volumetric) part of the strain energy function, because volume variations are very small [3].

$$W = \eta W_{iso}(\overline{I}_1, \overline{I}_2) + \Phi(\eta) + W_{vol} \tag{3.34}$$

Where:

η	the damage variable, $0 < \eta < 1$
$\Phi(\eta)$	the damage function, with $\Phi(1) = 0$, represents the energy required to damage the elastomer

The Ogden Roxburgh model considers the behaviour of the material dependent on maximum reached strain energy. Therefore, the damage parameter and the damage function depend on the difference between the current strain energy function W_{iso} and the previously maximum energy encountered W_m . The calibration of the mathematical model requires constantly checking the difference between these values, in order to activate or deactivate the damage parameter. The damage parameter and the damage function are expressed as follows.

$$n = 1 - \frac{1}{r} erf\left[\frac{1}{m}\left(W_m - W_{iso}\left(\overline{I}_1, \overline{I}_2\right)\right)\right] \tag{3.35}$$

$$-\Phi\left(\eta\right) = merf^{-1}\left[r\left(\eta - 1\right)\right] + W_m \tag{3.36}$$

Where

m and r	material constants, with m and $r > 0$
erf	the error function, $erf\,(x) = \frac{2}{\sqrt{\pi}} \int_{-x}^{x} e^{-t^2} dt$
erf^{-1}	the inverse if the error function
W_m	previously maximum energy encountered

Mars [47] proposed a generalization of the above law by adding the parameter b in the denominator of the error function. This modified model reduces to the Ogden - Roxburgh model when b=0 [48]. Most finite element software currently support this generalized form of the Ogden - Roxburgh model.

$$n = 1 - \frac{1}{r} erf \left[\frac{\left(W_m - W_{iso}\left(\overline{I}_1, \overline{I}_2\right)\right)}{m + bW_m} \right] \tag{3.37}$$

Where:

b	material constant, with $b < 0.5$

3.6.2 Guo

The Ogden - Roxburgh model can only describe situations that approach the "ideal Mullins effect", as shown in Figure 3.1(a), where the unloading and reloading response follow the same path. In cases of diverging loading and reloading responses (see Figure 3.1(b)), a second class of models is defined. To this day, these models are not supported by finite element codes, unless they are considered via a user defined subroutine. Models accounting for this divergence of the loading and reloading paths have been developed by Miehe [49] and Besdo and Ihlemann [50]. Recently, a damage model based on the theory of pseudo-elasticity was proposed by Guo [32]. This model is again based on Equation (3.34) but specifies different expressions for the damage variable n in the unloading and reloading phase.

Unloading branch:

$$n = 1 - \frac{1}{r} erf \left[\frac{W_m - W_0}{m(W_m - W_{00})} \right] \tag{3.38}$$

Where:

m and r	material constants, with m and $r > 0$
W_m	previously maximum energy encountered
W_0	current strain energy of the undamaged material (or $W_{iso}\left(\overline{I}_1, \overline{I}_2\right)$)
W_{00}	strain energy at the origin in the stress-free state

When the material returns to the origin from primary loading and no deformation remains, the minimum value of the damage variable is n_m:

$$n_m = 1 - \frac{1}{r} erf(\frac{1}{m}) \tag{3.39}$$

Reloading branch:

During unloading the damage variable is monotonously decreasing from 1 to its minimum value n_m. Assuming that at a specific value of strain energy, W_{mr}, the material is reloaded. Then damage is taken into account based on variable n_r, which increases from n_m and more. Therefore, in this case Equation (3.34) is written as:

$$W = \eta_r W_{iso}(\overline{I}_1, \overline{I}_2) + \Phi(\eta) + W_{vol} \tag{3.40}$$

The damage variable n_r ($n_m < n_r < 1$) that pilots the reloading response of the material is calculated as follows.

$$n_r = n_m + (1 - n_m) erf \left[\frac{1}{m_1} (\frac{W_0 - W_{mr}}{W_m - W_{00}})^{r_1} \right] \tag{3.41}$$

Where:

m_1 and r_1	material constants
n_m	the minimum value of the damage variable
W_{mr}	the strain energy when the material is again subjected to loading

Chapter 4

Experimental analysis of shear tests

This chapter studies the mechanical behaviour of TSSA laminated circular connections under simple shear load. The specimens are subjected to both monotonically increasing and cyclic loads and subsequently they are brought to failure. In this chapter, the design of the tests is presented and the results are discussed.

4.1 Method

4.1.1 Materials and geometry of specimens

The specimens consist of a solid 316L stainless steel connector with diameter 50mm, height 20mm and tolerance h9 [ISO 286][1] [1], which is in the center of a 150 x 150 mm annealed glass plate with a thickness of 15mm. The TSSA foil is 1mm thick. The connector has a circular shape, which is favorable, because in this way stress intensifications at the edges are avoided, unlike the case of rectangular connectors [1]. The bonded surface is machined with roughness (R_a) of 8 micron [1], in order to ensure good contact of the materials.

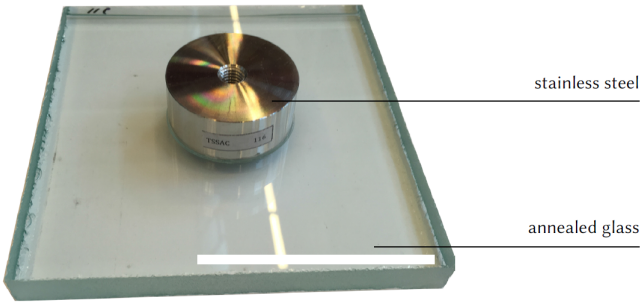


Figure 4.1: Glass specimens with a TSSA laminated steel connector

[1]ISO 286 (Geometrical product specifications (GPS) — ISO code system for tolerances on linear sizes) specifies international tolerance grades for holes and shafts. Tolerance h9 refers to round bar tolerances based on ISO 286-2.

4.1.2 Test set-up

Tests are performed with a SCHENCK testing machine and a 10KN load cell. A specially designed steel set-up is made, in order to fix the glass properly and to ensure that a pure shear load is applied to the connection. The shear load is transferred via a 10mm thick steel plate with a circular hole (diameter 50.1 mm) in the middle. The circular hole renders possible to impose inverse shear load to the connection as well. The steel plate is connected to a steel rod (M24) which in turn is connected to the load cell and fixed at the upper part of the machine. The rest of the steel set-up ensures that the glass specimen is rigidly fixed to the machine base. The base is able to move up and down and in this way introduces the shear load into the system. The glass plate is placed in-between 15mm thick steel plates and is clamped in this position with bolts. Stability is ensured by four L-profiles (L 80 x 80 x 8 mm). Aluminum plates with 2mm thickness are placed on the interfaces of glass and steel in order to reduce the probability of glass breakage during the test.

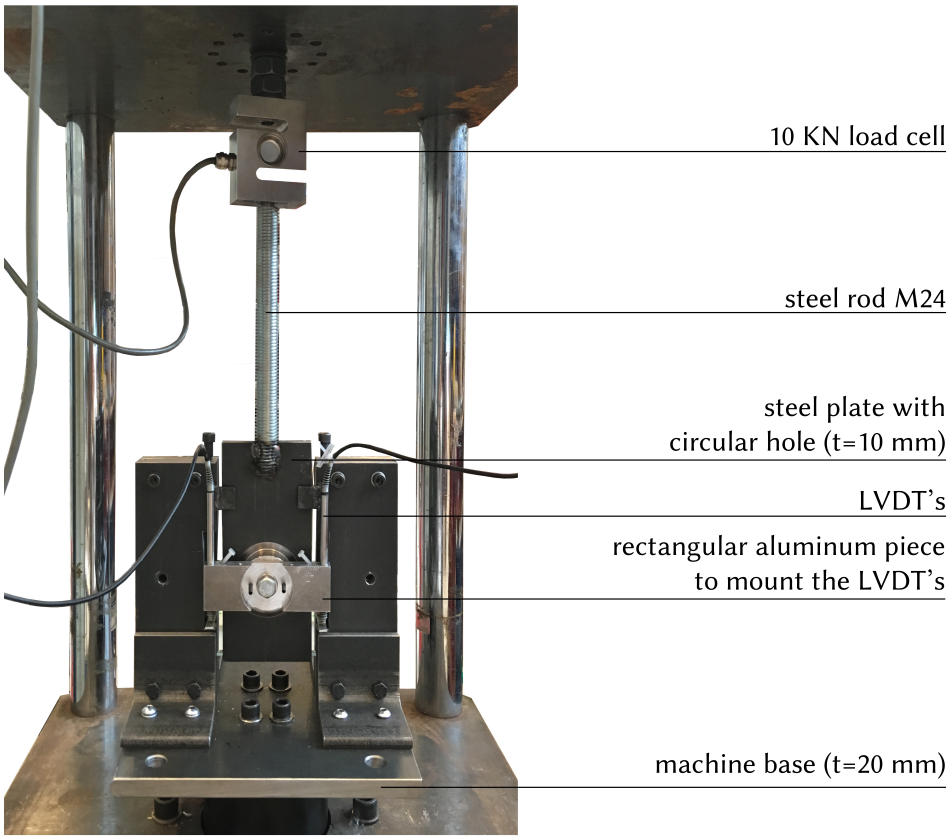
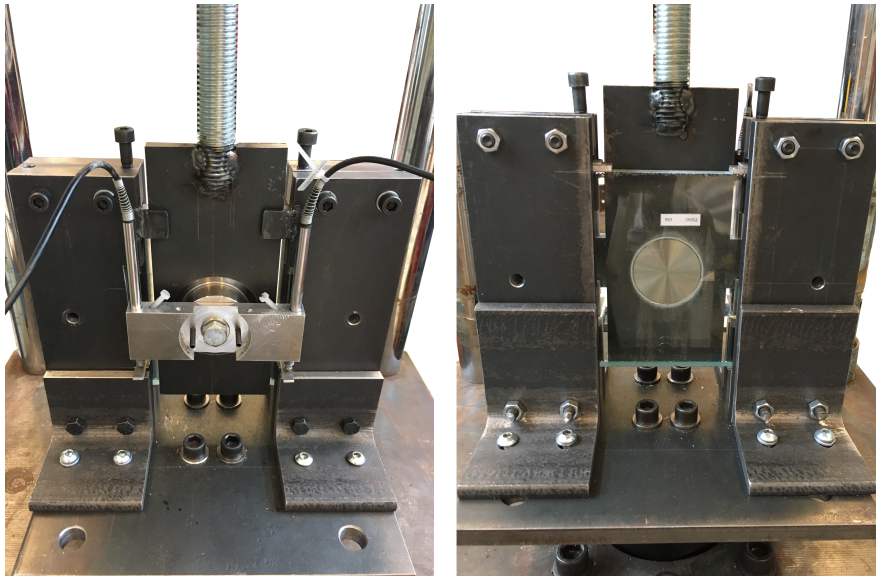


Figure 4.2: Shear test set-up

The relative displacement between the glass and the connector is measured by two LVDT's ± 5 mm which are placed on the right and left side of the connector. These are mounted onto a rectangular aluminum piece which in turn is rigidly connected to the stainless steel button (see Figures 4.2 and (4.3a)). The LVDT's stand on two small aluminum L-profiles with a thickness of 2 mm, which are glued

on the glass surface. In this way, it is possible to measure the relative displacement of glass and steel and thus the displacement of the adhesive. The behaviour of TSSA in shear is recorded on video during the tests, as the set-up allows visual inspection of the adhesive (see Figure (4.3b)).



(a) Front view (b) Backside

Figure 4.3: Close view to the shear test set-up

The steel plate that transfers the load to the connector is aligned to the interface between the glass plate and the adhesive. Its thickness is reduced to 3mm close to the circular hole. In this way, the eccentricity of the shear load to the connector is minimized [1], in order to approach as much as possible a pure shear stress state.

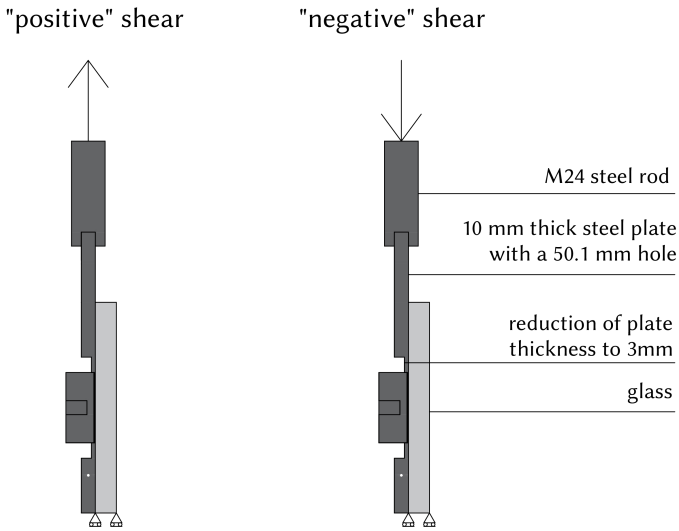


Figure 4.4: Simplified sketch of the shear load application

4.1.3 Description of tests

A series of static and cyclic tests are performed in order to study the behaviour of TSSA laminated connections under simple shear load. The average room temperature at the time of the tests is recorded at 23.5^{o}C. The monotonic tests are performed in displacement control at a displacement rate of 1mm/min. The cyclic tests are conducted in force control and loading cycles are performed from 0 to +P or from -P to +P, as illustrated in Figure (4.5). The loading pattern is based on the guideline ETAG 002 [20], which specifies a trapezoidal-shaped function with time for mechanical fatigue tests of structural sealants. The guideline describes a linear increase of load with time, followed by a stable phase where the maximum (or minimum load) remains constant to counteract creep effects. When unloaded, a steady state of zero (or nearly zero) loading follows. In this way, the mechanical response of the adhesive is isolated as much as possible from viscoelastic effects related to creep or relaxation, in order to derive the time-independent response of TSSA.

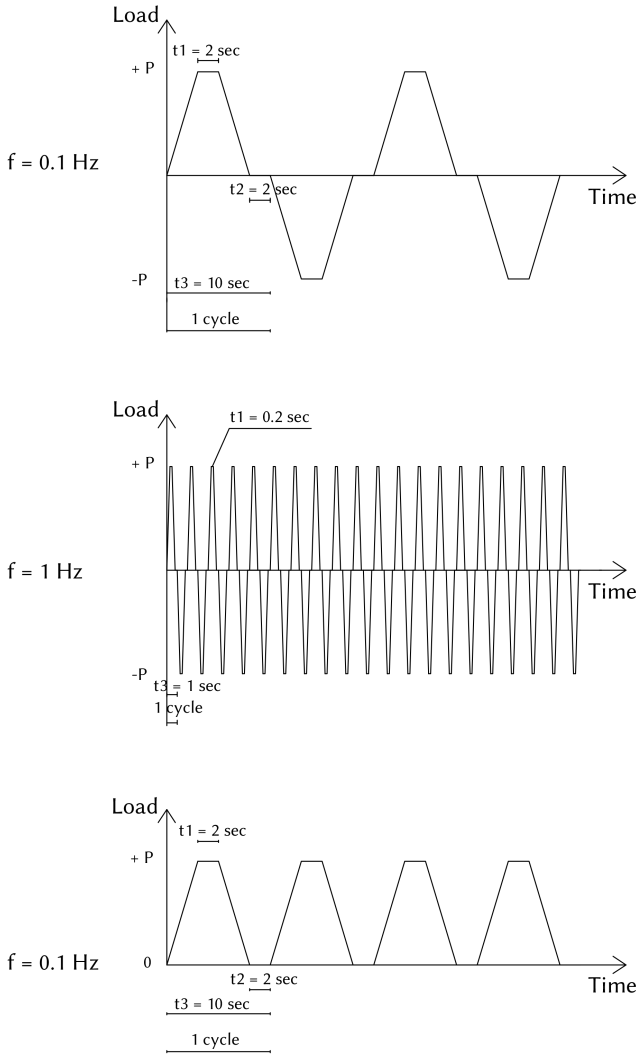


Figure 4.5: Cyclic loading pattern for shear tests performed from -P to +P and from 0 to +P

Cycles are performed at different load levels in order to record the point when the stress softening starts to occur, to study the hysteretic behaviour of the adhesive at different load levels and to observe if and when the whitening phenomenon appears. The cycles begin from a loading loop of -1 to 1 KN, which is repeated 50 times. Subsequently the maximum (and minimum) load increases in absolute terms with a step of 1 KN every 50 cycles. Loading cycles are performed up to 8 KN, according to the cyclic loading schedule of Table 4.1. At least three specimens were tested for each type of test described in the table below.

Table 4.1: Cyclic loading schedule of shear tests

Tests without inverse shear:		Tests with inverse shear:		
Cycles in KN (force)	Cycles in MPa (engineering stress)	Cycles in KN (force)	Cycles in MPa (engineering stress)	Number of cycles
from 0 to 1KN	from 0 to 0.5 MPa	from -1 to 1KN	from -0.5 to 0.5 MPa	50
from 0 to 2KN	from 0 to 1 MPa	from -2 to 2KN	from -1 to 1 MPa	50
from 0 to 3KN	from 0 to 1.5 MPa	from -3 to 3KN	from -1.5 to 1.5 MPa	50
from 0 to 4KN	from 0 to 2 MPa	from -4 to 4KN	from -2 to 2 MPa	50
from 0 to 5KN	from 0 to 2.5 MPa	from -5 to 5KN	from -2.5 to 2.5 MPa	50
from 0 to 6KN	from 0 to 3 MPa	from -6 to 6KN	from -3 to 3 MPa	50
from 0 to 7KN	from 0 to 3.5 MPa	from -7 to 7KN	from -3.5 to 3.5 MPa	50
from 0 to 8KN	from 0 to 4 MPa	from -8 to 8KN	from -4 to 4 MPa	50
			Total:	400

Healing of the stress-softening phenomenon has been observed in many industrial rubber materials. Healing may refer to either the recovery of the permanent deformations or of the complete stress-strain response [24]. A series of tests are conducted in order to study if any recovery of the mechanical response of the adhesive takes place. It has been proven that temperature and time may have an effect on the recovery of several elastomers, but the latter to a much lesser extend. Specimens are loaded cyclically from -4 KN to +4 KN and then are left to rest for almost two days. During this rest period, half of the specimens are heated up to 80°C for 5 hours. After two days, the specimens are loaded cyclically for the second time.

4.2 Results

4.2.1 Static tests

The mechanical response of TSSA connections under shear load is shown in Figure 4.6[2] and appears to be mainly linear. This is in agreement with the results of Santarsiero [1], Sitte et al. [7] and Hagl et al. [9]. From the video recording, very slight whitening is visible starting at an engineering stress of approximately 3.5 MPa. It becomes more evident at the bottom part of the connection as we approach failure. This is probably due to some bending taking place, as in practice it is difficult to impose a pure

[2]Considering a 2-dimensional square element, which has width dx and height dy, simple shear causes the square element to change into a rhombus. The amount of shear (or shear strain), γ, is equal to the change in angle in radians. Therefore:$\gamma = tan\alpha \approx \alpha = \delta/t$, where δ is the recorded horizontal displacement and t is the thickness of the adhesive in mm (see also Table 6.1).

shear load to the connection. Therefore, the bottom part of the adhesive is in tension and the upper part is in compression, thus leading the bottom half of the area to gradually turn white. Nevertheless, the whitening phenomenon is far less evident for the most part of the deformation field compared with the observations of Santarsiero [1], Hagl et al. [9] and Sitte et al. [7] in tensile tests of circular connections (see also following Chapter 5).

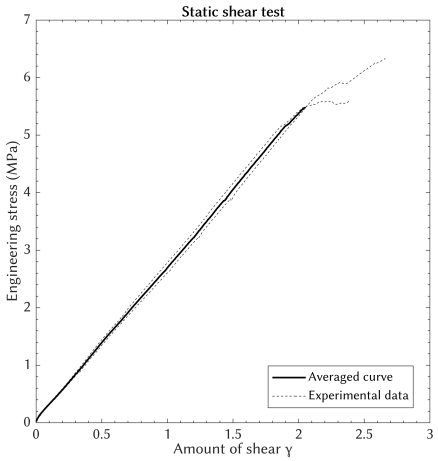
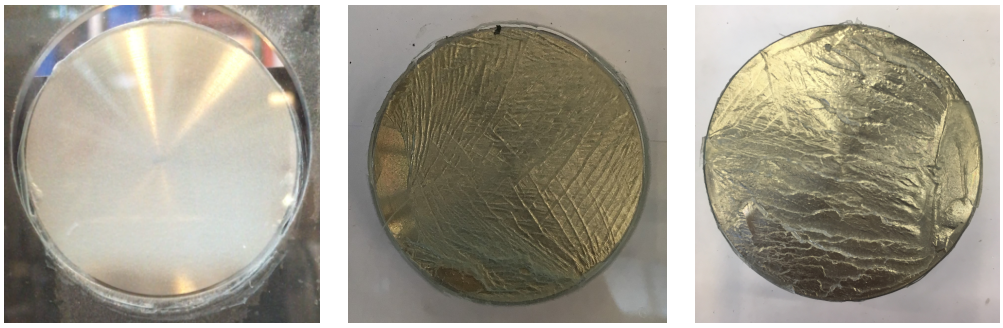


Figure 4.6: Experimental results of TSSA laminated connections under static shear force



(a) Whitening effect during testing (b) Failure pattern after testing (c) Failure pattern after testing

Figure 4.7: TSSA laminated connections under static shear loading. The load is applied along the vertical direction.

The mean values of the failure load and (engineering) stress levels (F_u and σ_u, respectively) recorded during the static shear tests are summarized in Table 4.2.

Table 4.2: Test results of TSSA laminated connections subjected to shear static loading

Test type	Number of tests	Failure load F_u (KN)	Failure load $\sigma_{eng,u}$ (MPa)	Displacement at failure (mm)	Standard deviation (KN)	COV (-)
Shear static	3	11.71	5.97	2.528	1.03	0.088

4.2.2 Cyclic tests

Figure 4.8 shows the mechanical response of TSSA under repeated loading cycles from 0 to +P at 0.1 Hz. The stress-softening phenomenon is observed even at loading cycles performed up to 0.5 MPa and it becomes more critical as the maximum load increases. In the graph it is observed that for the same applied engineering stress the shear strains become significantly larger as the maximum load increases. A relation is observed between the magnitude of softening and the permanent deformations at the stress-free state, as for higher damage due to softening, larger permanent deformations are observed. Isolating the cycles for each load level, the damage appears to increase with the number of cycles, but it seems that it tends to stabilize towards the 50^{th} cycle (see Section 4.3). Throughout the test, very slight whitening of the adhesive surface takes place, which is barely visible.

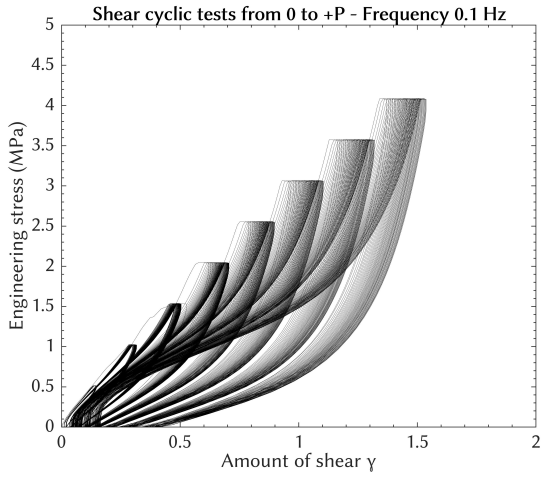
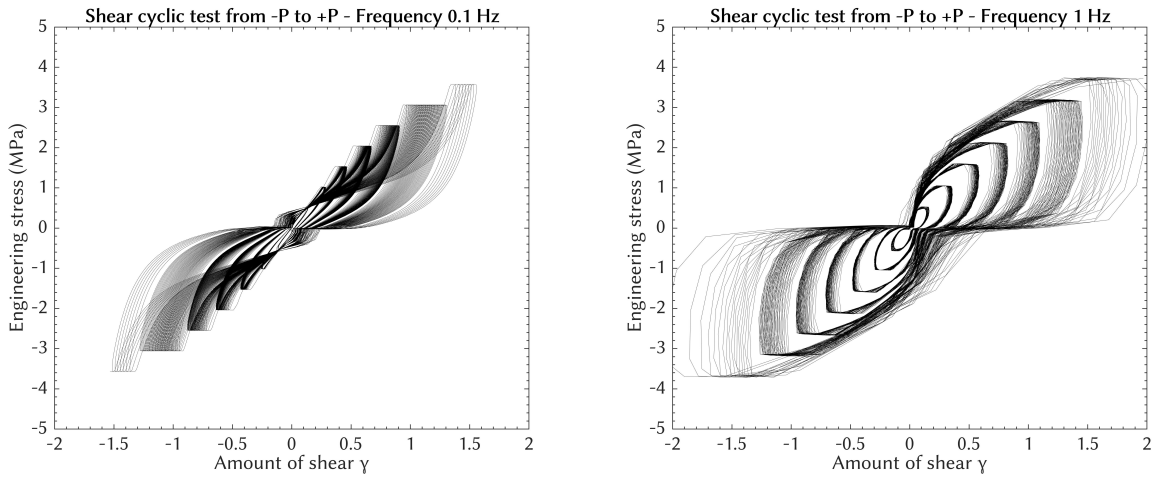


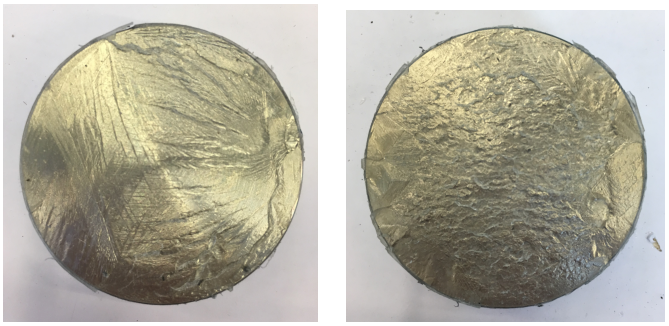
Figure 4.8: Shear cyclic loading tests from 0 to +P at 0.1 Hz

Figure 4.9 compares the deformation behaviour of the adhesive when loaded cyclically from -P to +P under two different frequencies. Figure 4.9(a) illustrates the mechanical response of specimens loaded with a frequency of 0.1 Hz. The softening response resembles the one of Figure 4.8. Most of the tested specimens failed to reach loading cycles up to 4 MPa, unlike the case of shearing in only one direction. Specimens imposed under a higher frequency of 1 Hz also exhibit a stress softening behaviour during unloading. However, in contrast with the results obtained at 0.1Hz, the stiffness appears to increase during the loading phase (see Section 4.3).



(a) (b)

Figure 4.9: Shear cyclic loading from -P to +P: (a) Frequency 0.1 Hz, (b) Frequency 1 Hz



(a) Failure pattern at 0.1 Hz (b) Failure pattern at 1 Hz

Figure 4.10: TSSA laminated connections under cyclic shear loading from -P to +P. The load is applied along the vertical direction.

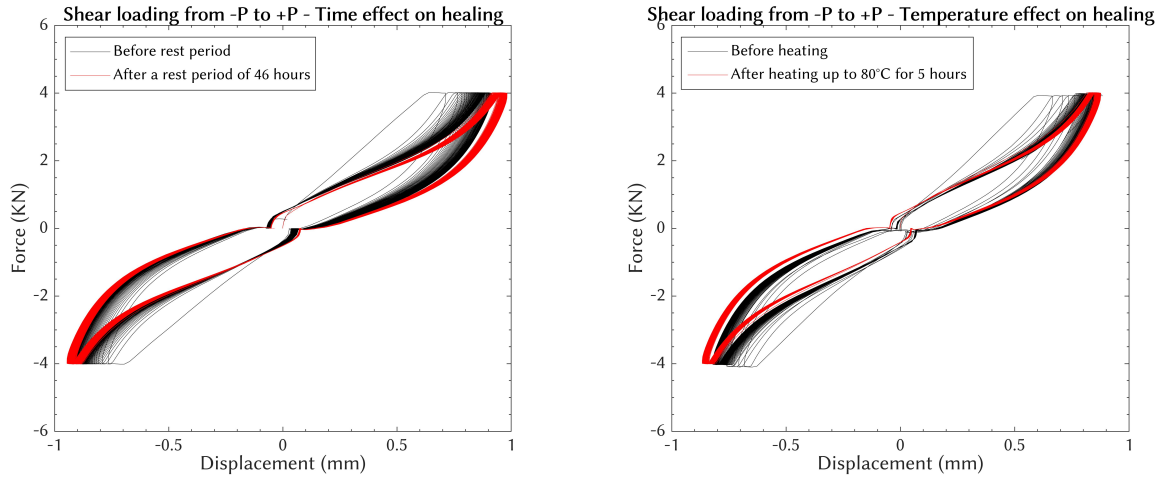
The mean values of the failure load levels (F_u) and the corresponding engineering stresses (σ_u) recorded during the cyclic tests are summarized in Table 4.3. Cyclic tests performed from 0 to +P did not fail during the cyclic loading test and thus were subsequently brought to failure by a static test (1mm/min). On the other hand, tests performed from -P to +P stopped before the completion of the cyclic loading schedule due to failure of the connection. The average number of cycles when failure occurred is also given in the following table. For more detailed information on the failure of the connections under shear load see Appendix A.

Table 4.3: Results of TSSA laminated connections subjected to cyclic and static shear tests

Test type	Freq. (Hz)	Number of tests	F_u (KN)	$\sigma_{eng,u}$ (MPa)	Failure occurred:	St. dev. (KN)	COV (-)
Cyclic shear from 0 to +P followed by a static test	0.1	3	12.17	6.20	during the static test	0.67	0.055
Cyclic shear from -P to +P	0.1	3	7.15	3.64	after 326 cycles	0.30	0.042
Cyclic shear from -P to +P	1	4	7.64	3.89	after 354 cycles	0.55	0.073

4.2.3 Healing

A series of tests are conducted to observe if any healing of the stress softening phenomenon takes place. Figure 4.11 illustrates the mechanical response of TSSA after a rest period of 46 hours (Figure 4.11(a)) and after heating the specimens to 80°C (Figure 4.11(b)). Time does not seem to have an effect on the behaviour of the adhesive, as when the specimens are subjected to loading cycles for the second time, the deformations (permanent or not) seem to continue to grow from the same level recorded during the first loading phase. Regarding the temperature effect, it is evident that no recovery of the mechanical response of TSSA takes place after heating the specimens for 5 hours. A small decrease of the maximum and permanent deformation is though observed in the range of 5% and 4%, respectively. Event though, the damage due to the Mullins effect appears to be irreversible, more tests are needed in order to form more solid conclusions.



(a) (b)

Figure 4.11: Shear test results related to healing of the stress-softening phenomenon: (a) Time effect, (b) Temperature effect

4.3 Analysis and discussion

Figure 4.12 shows the first (1^{st}) and last (50^{th}) cycles for each load level. The cyclic test results are also compared with those derived from the static tests. The deformation behaviour of TSSA in shear exhibits considerable difference under static and cyclic loading. The Mullins effect causes significant loss of stiffness during the unloading phase. The softening becomes more severe as the maximum load applied increases. On the other hand, the reloading branch follows a different path and shows an S-shaped response. Similar unloading and reloading response is observed in the work of Sitte et al. [7], who conducted shear cyclic tests at a strain rate of 0.1 mm/sec. At low and moderate deformations the material shows a softening response and as we approach the maximum (previously applied) load a stiffer behaviour is observed, where an increase of the engineering stress results in a very small change of the shear strains. This could be attributed to strain hardening effects; however, microscopic observation at a molecular level is needed to verify such a hypothesis. Treolar [51] studied strain hardening effects of rubber materials, which are caused due to locking of molecular chains that are fully stretched. In other words, when molecular chains reach their deformation limit, they become extremely stiff for any further increase of the load.

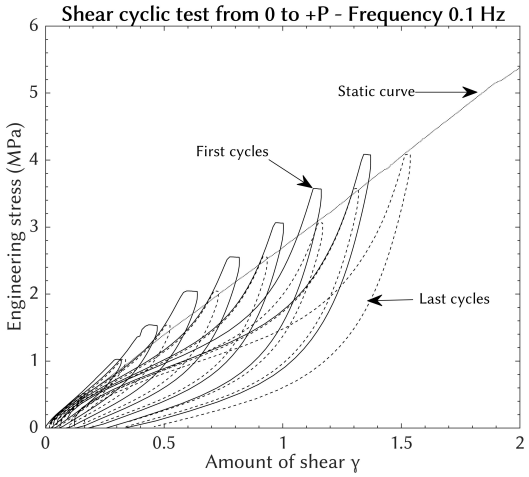


Figure 4.12: Comparison between cyclic and static shear test data

In Figure 4.12 a shift of the loading and unloading curves to the right is observed, which is caused due to creep of the adhesive during the test. This movement seems to gradually decrease with the number of cycles (see also Figure 4.8). For lower load levels the shifting of the curves appears to be minimum, while as the maximum load increases it becomes more severe. To make this more clear, energy dissipation analysis is conducted. Here the dissipated energy for cycles performed at engineering stresses up to 0.5, 1.5, 2.5 and 3.5 MPa is indicatively given in Figure 4.13.

On the left side of Figure 4.13, the calculated dissipated energy in MPa (or 10^{-6} J/m^3) is plotted against the number of cycles. On the right side, the first and last cycles for each load level are plotted separately. It is typical in rubbers exhibiting the stress softening phenomenon that during the first cycle a large amount of energy is dissipated. This is in fact observed in the work of Sitte et al. [7], where TSSA was subjected to uniaxial, shear and equibiaxial cyclic tests. After the first cycles the dissipated energy of rubbers either gradually decreases, in case of displacement controlled tests, due to relaxation or increases, in case of force controlled tests, due to creep. The latter is in fact observed in this case, since

the tests are carried out in force control.

For maximum engineering stresses up to 1 MPa, the material does not show significant creep effects and this is the reason the dissipated energy remains almost stable after the first cycle. In this case, the curves of the first and last cycle overlap. For loading cycles performed above 1 MPa the effect of creep becomes clearly visible, as the dissipated energy does not remain stable after the first cycle but shows an increase. In this case, creep causes the shifting of the curves to the right. In most cases the rate of increase seems to decrease as we approach the 50^{th} cycle, meaning that the dissipated energy tends to stabilize with the number of cycles. For cycles performed up to 1.5 MPa, the dissipated energy has almost stabilized at the 50^{th} cycle, a fact which indicates that the unloading and reloading response will not further keep shifting to the right. For cycles above 1.5 MPa, the rate of increase of the dissipated energy seems to decrease approaching 50^{th} cycle; however, it is clearly not stabilized at this point. In this case, more cycles are required to detect the point where the dissipated energy and thus the mechanical response of TSSA stabilize.

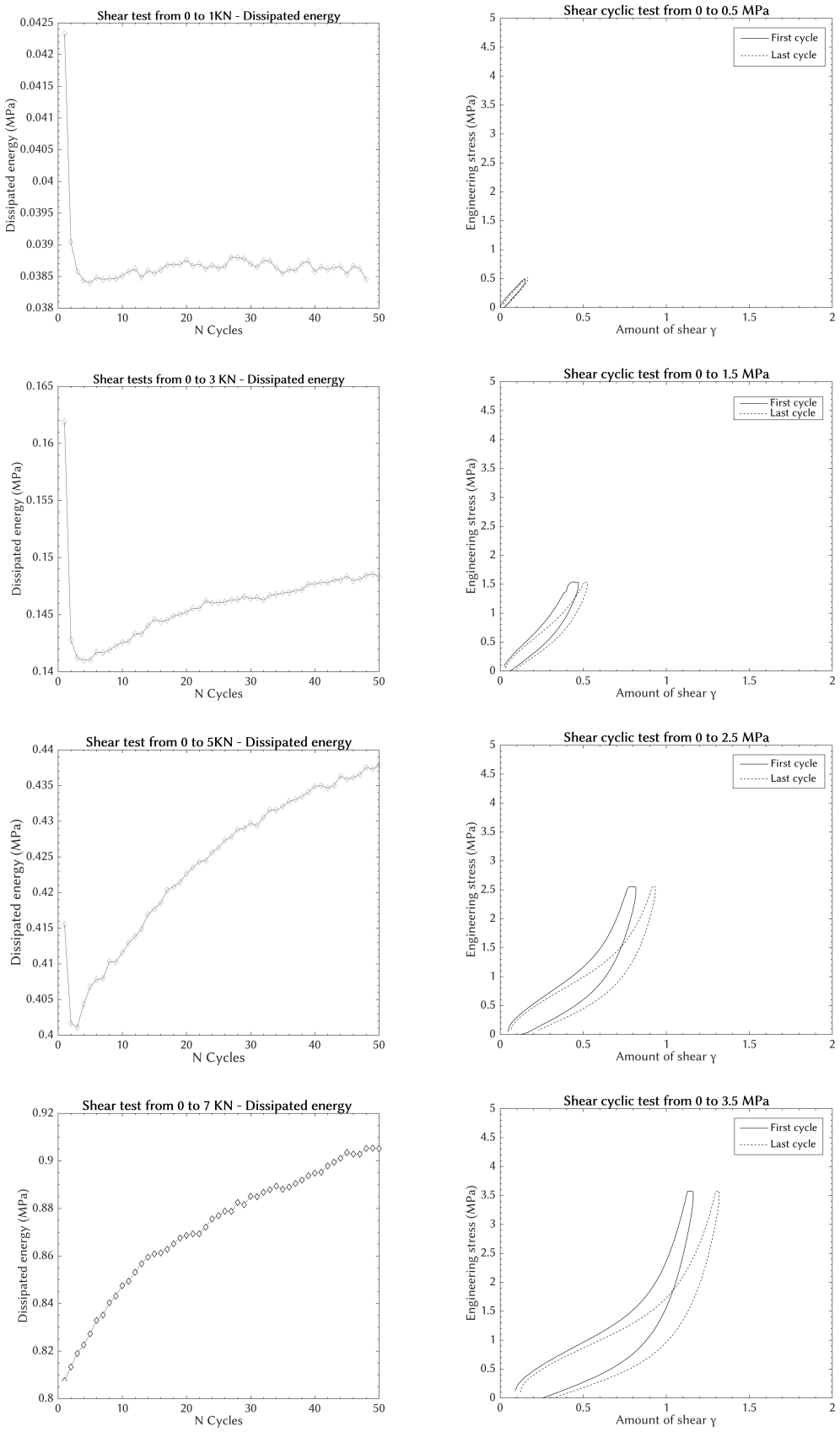


Figure 4.13: Energy dissipation analysis

Regarding the tests where specimens were subjected to reverse shear loading, it is interesting to compare the deformation behaviour of the adhesive under “positive” and “negative” shear. “Positive” and “negative” shear refer to the direction of the load as defined in Section 4.1.2. Figure 4.14 compares the mechanical response of the adhesive when a shear load is applied in both directions. The stresses and strains, corresponding to negative shear, are converted to their absolute values and compared with the results from positive shear. When the adhesive undergoes negative shear, a small decrease of the absolute deformations is observed for the same stress level. This decrease is in the range of 6% and presumably it is due to the fact that negative shear also recovers the permanent deformations caused by the previous positive shearing.

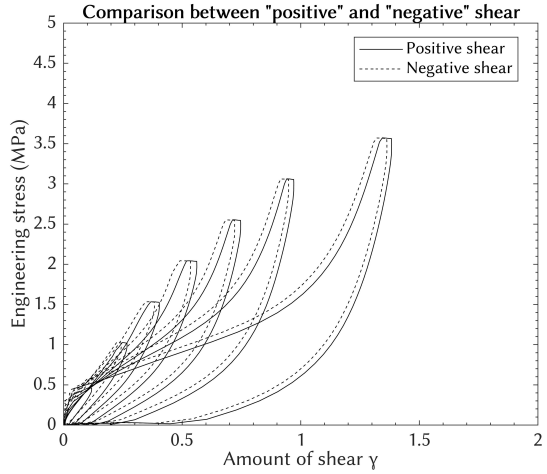


Figure 4.14: Comparison between “positive” and “negative” shear

A comparison of the mechanical response was also made between the results of cyclic shear tests from 0 to +P and from -P to +P. Figure 4.15 illustrates and compares the mechanical response in both cases for load cycles corresponding to the same maximum stress level and (cycle) number. Reverse shearing tests appear to cause smaller deformations for the same stress level. The difference in deformations is larger for cycles performed at low stresses, but it decreases for cycles performed at higher stress levels. The contrary is observed only in the final set of cycles (from 0 to 3.5MPa), where reverse shearing tests showed significant deformations and the specimens failed before the completion of the cyclic loading schedule. Nevertheless, for the largest part of the deformation field, shear loading tests performed in only one direction result in a more conservative response and thus are considered more suitable for modeling purposes. This could probably be explained due to the fact that permanent deformations or the deformations caused during the steady loading phase (due to creep effects) are recovered by the following inverse loading cycle.

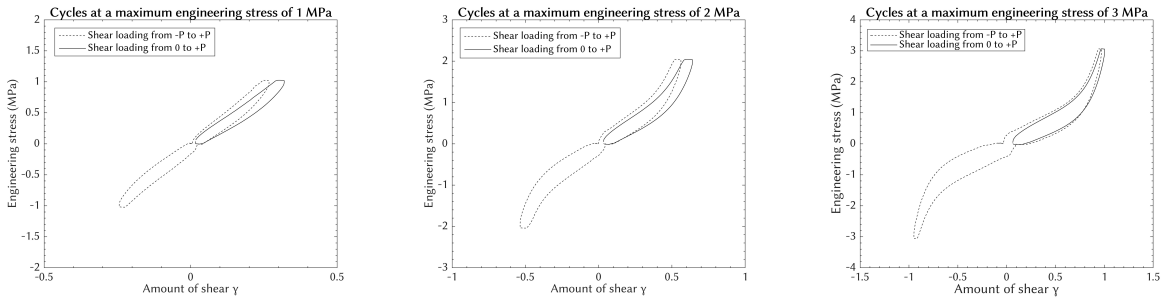


Figure 4.15: Comparison between cyclic shearing from 0 to +P and from -P to +P

Finally, it appears that the mechanical response of TSSA under cyclic shear loading is frequency dependent. Rubber-like materials, such as TSSA, always exhibit viscoelastic effects and thus their response is expected to be dependent on the loading rate. In Figure 4.16, the first cycles for each load level are isolated, in order to clearly observe the difference in behaviour between the tested frequencies of 0.1 and 1 Hz. Figure 4.17 compares the cyclic behaviour of the adhesive subjected to frequencies of 1 and 0.1 Hz. At a frequency of 1 Hz, the loading response of the adhesive shows a considerably stiffer behaviour compared with the tests performed at 0.1 Hz. The opposite is observed during the unloading phase where the softening behaviour of the adhesive appears to be more severe at 1 Hz for the largest part of the deformation field.

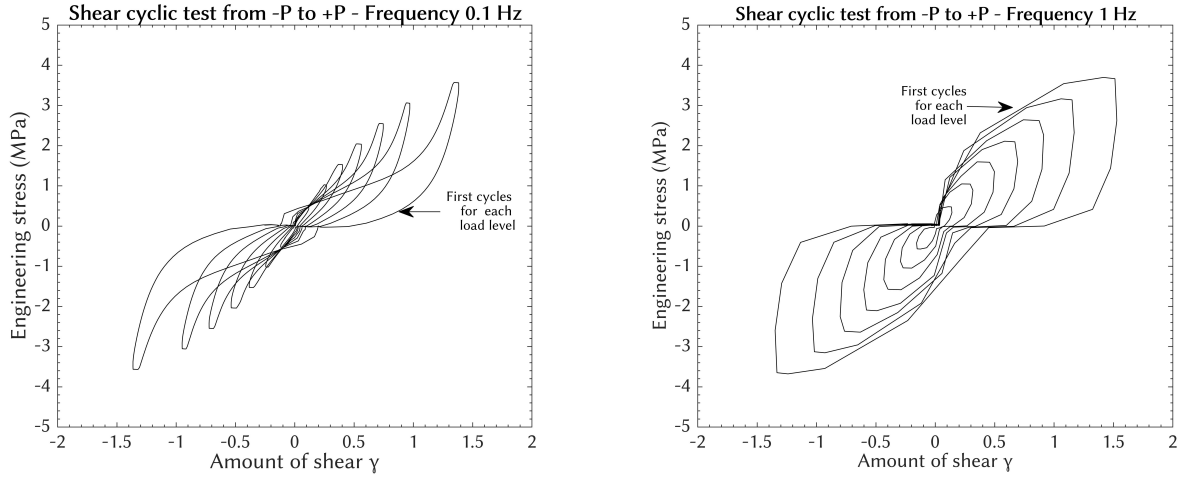


Figure 4.16: First cycles for each load level - Shear cyclic tests from -P to +P

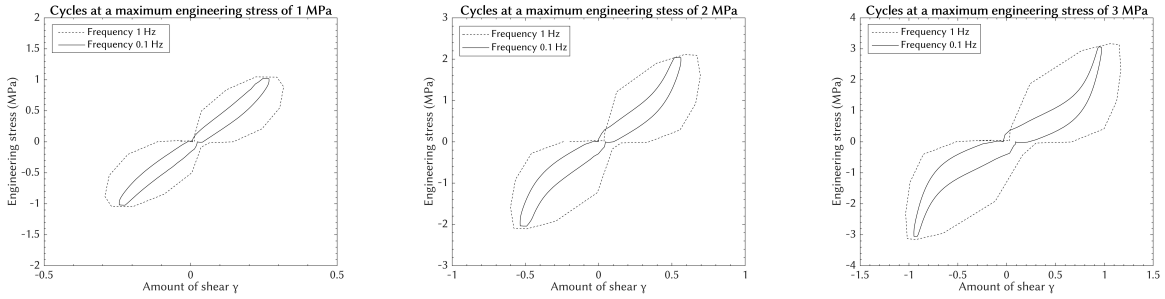


Figure 4.17: Comparison between different frequencies

4.4 Conclusions

In this chapter the static and cyclic mechanical response of TSSA circular connections under shear load is studied. From the experimental results, the following conclusions can be drawn.

The mechanical response of the adhesive in this configuration is mainly linear until failure; however, strong nonlinearities are observed from the results of cyclic loading tests. The stress-softening phenomenon appears at low stress levels of 0.5 MPa and becomes more severe with cycles of increasing magnitude. The mechanical response of TSSA appears to constantly change with the number of cycles, a fact which is observed even for cycles performed at the same stress level. Energy dissipation analysis showed that the response of TSSA tends to stabilize with the number of cycles. For loading cycles up to 1.5 MPa the response can be considered stable at the 50^{th} cycle. However, for cycles performed at higher loads, more cycles are required to detect the point when the stress-strain response stabilizes.

Laminated connections were also subjected to reverse shearing tests and the results were compared with those from shearing in one direction. The deformation behaviour of the adhesive appeared to be very similar. Test results from shearing in one direction showed slightly higher deformations for the same stress level and thus they could be considered more conservative when it comes to the simulation of the deformation behaviour of the adhesive. However, connections subjected to reverse shear loading failed before the completion of the cyclic loading schedule. Finally, the cyclic behaviour of TSSA showed some clear dependency on frequency.

A future experimental campaign should focus on on the relation between the softening effect and fatigue behaviour, as well as on finding a threshold for the change of the mechanical response under different frequencies. Further discussion on recommendations for future research is provided in Chapter 8.

Chapter 5

Experimental analysis of tensile tests

The tensile behaviour of TSSA laminated circular connections is investigated by a series of experimental tests. The specimens were subjected to both monotonically increasing and cyclic loads and subsequently were brought to failure. In this chapter, the design of the tests is presented and the results are discussed.

5.1 Method

5.1.1 Materials and geometry of specimens

A series of circular stainless steel TSSA laminated connections were tested under tensile forces. The circular connectors are made of solid 316L stainless steel bars of 50mm diameter with a height of 20mm and tolerance h9 [ISO 286] [1]. The bonded surface is machined with roughness (R_a) of 8 micron [1], in order to ensure good contact of the materials. All the circular connectors come with a 10mm blind threaded hole in the middle with depth 15mm [1]. This connectors are bonded to the glass by a very thin layer of TSSA with nominal thickness of 1mm. The glass plates are made of annealed glass and have a size of 150 x 150mm.

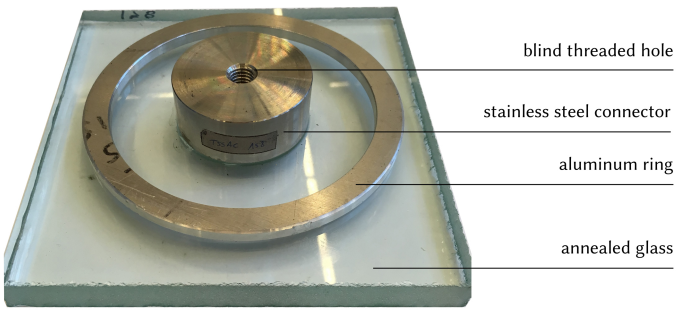


Figure 5.1: Glass specimens with a TSSA laminated steel connector.

5.1.2 Test set-up

Tests were performed with a SCHENCK testing machine and a 10 KN load cell. A steel set-up is made to restrain the glass plate during loading. More specifically, a steel plate with a thickness of 35 mm and a circular hole (with diameter 80 mm) in the middle is bolted onto two UPE 100 profiles, which in turn are fixed onto the machine base. The glass specimen is positioned right underneath the 35 mm thick steel plate. The UPE profiles allow the placement of a camera right below the glass specimen. For safety reasons, two pieces of wood uphold the glass plate. Between the steel and glass plates an aluminum ring is placed to ensure that the force is equally distributed (see also Figure 5.1). The ring has and external radius of 120mm, it is 20mm in width and 5mm in height. A cardboard mould was used in order to make sure that the aluminum ring is always positioned in the center of the specimen.

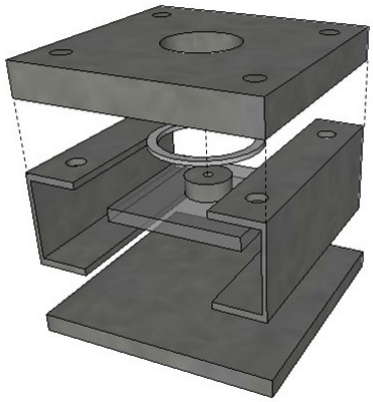


Figure 5.2: Simplified sketch of the steel set-up supporting the glass during the tensile tests

The stainless steel button is connected to a hinge with an M10 steel rod. The hinge is used to make sure that the specimen is well centered and the load is evenly distributed to the adhesive layer. The tensile force is introduced to the system by displacing the machine base. The machine base moves downwards and so does the whole set-up; therefore, a tensile force is applied to the stainless steel connector. The displacements are measured by means of three LVDT's of ± 1 mm, uniformly distributed around the stainless steel button. This is to consider possible rotations induced by fabrication tolerances or imperfections [1]. The LVDT's are fixed onto an aluminum ring (see Figure 5.4) which is rigidly fixed onto the stainless steel button.

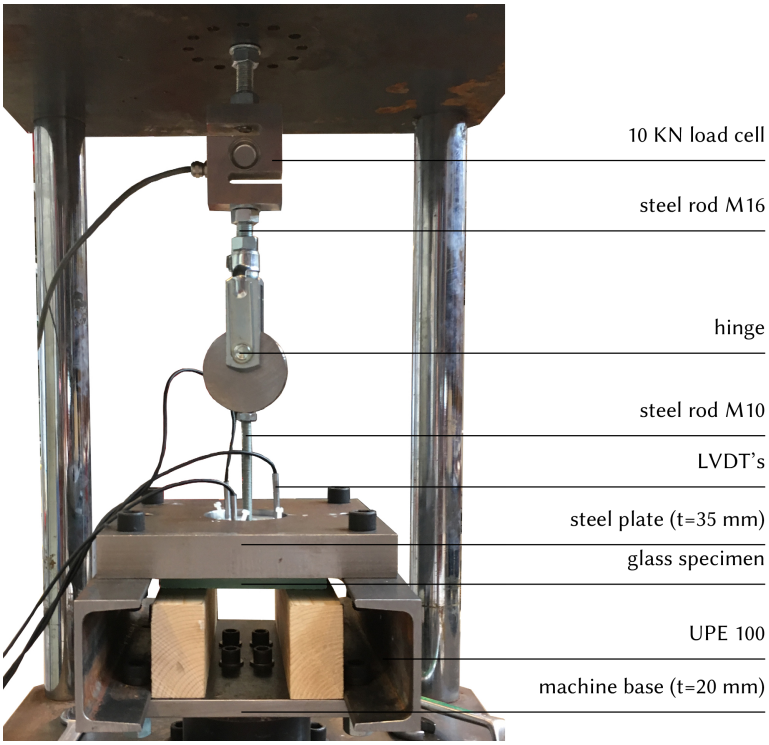


Figure 5.3: Tensile test set-up

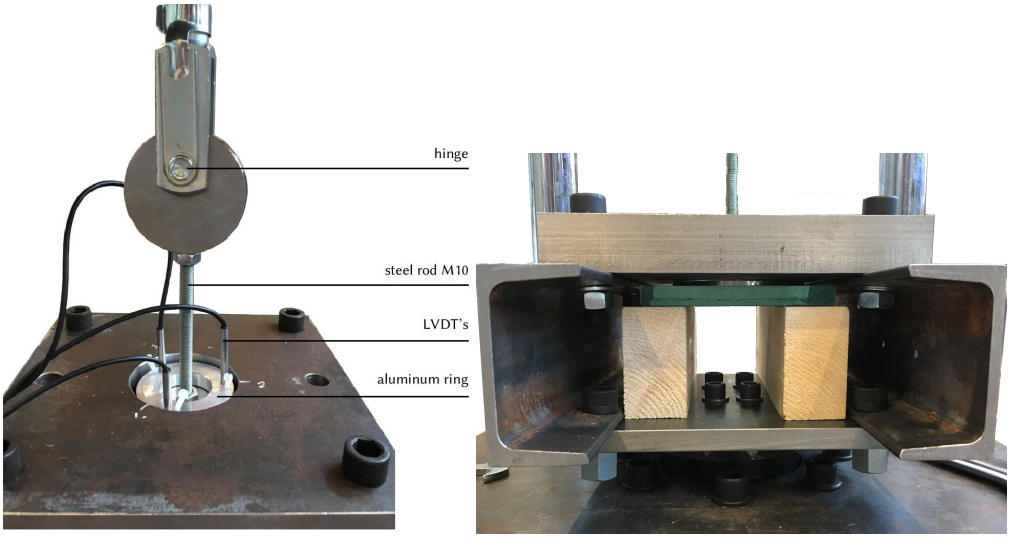


Figure 5.4: Close views to the tensile test set-up

5.1.3 Description of tests

A series of static and cyclic tests under room temperature are performed to study the behaviour of TSSA laminated connections. The average room temperature at the time of the tests is recorded at 23.7^{o}C. The static tests are performed in displacement control at a displacement rate of 1mm/min. The cyclic tests are conducted in force control and the specimens are subjected to loading cycles under two different frequencies of 0.1 and 1Hz. The loading pattern follows a trapezoidal form according to the one described in the guideline ETAG 002 [20] for mechanical fatigue tests of structural sealants. The guideline describes a linear increase of load with time, followed by a stable phase where the maximum load remains constant to counteract creep effects. In the end, the load is removed and a steady state of zero (or nearly zero) loading follows.

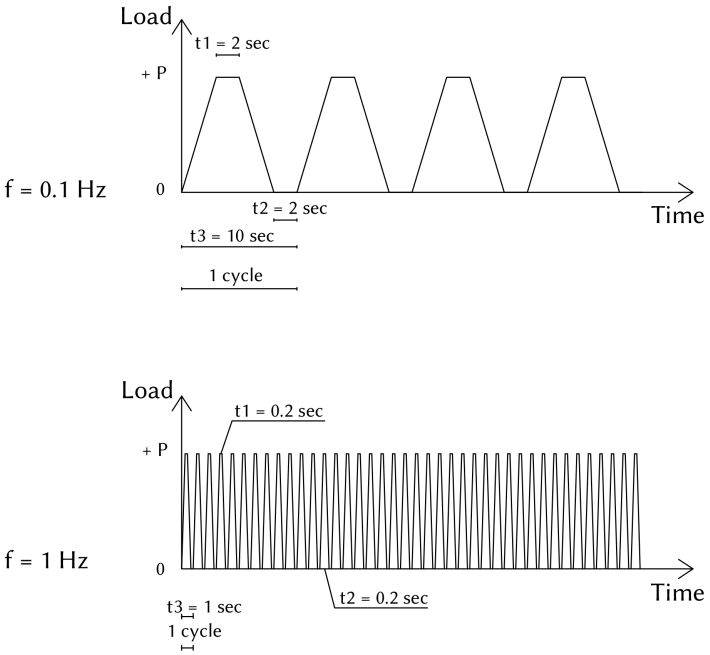


Figure 5.5: Cyclic loading pattern for frequencies 0.1 Hz (up) and 1 Hz (down)

Loading cycles are performed at different load levels in order to record the point when the stress softening phenomenon starts to occur and to study the hysteretic behaviour of the adhesive under different load levels. The cycles begin from a loading loop of 0 to 1KN that is repeated 50 times. Subsequently, the maximum load increases with a step of 1 KN every 50 cycles. The specimens are loaded up to a maximum load of 8 KN according to the cyclic loading schedule given in Table 5.1. The loading cycles are also expressed in terms of engineering stresses.

Table 5.1: Cyclic loading schedule of tensile tests

Cycles in KN (forces)	Cycles in MPa (engineering stresses)	Number of cycles
from 0 to 1 KN	from 0 to 0.5 MPa	50
from 0 to 2 KN	from 0 to 1 MPa	50
from 0 to 3 KN	from 0 to 1.5 MPa	50
from 0 to 4 KN	from 0 to 2 MPa	50
from 0 to 5 KN	from 0 to 2.5 MPa	50
from 0 to 6 KN	from 0 to 3 MPa	50
from 0 to 7 KN	from 0 to 3.5 MPa	50
from 0 to 8 KN	from 0 to 4 MPa	50
	Total	400

5.2 Results

5.2.1 Static tests

Figure 5.6 illustrates the stress-strain graph obtained by the tensile static tests. The graph is divided into two phases and resembles the experimental results obtained at 23°C in the research performed by Santarsiero et al. [1, 18]. The mechanical response starts from a linear behaviour up to approximately 4 MPa. Then, the second phase starts where the stiffness is significantly reduced and the behaviour of the adhesive exhibits an approximately linear behaviour until failure. An explanation for this abrupt change in stiffness at engineering stresses of 4 MPa has not been formulated so far (as the time of this writing). Microscopic observations at a molecular level are needed to understand the cause of this abrupt transition in stiffness.

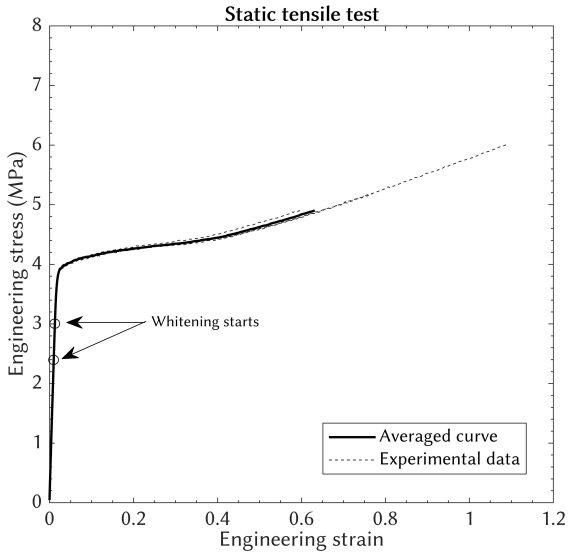


Figure 5.6: Tensile static test results of TSSA laminated connections

As expected, the whitening phenomenon of TSSA is observed during the tensile test. The whitening starts to be visible in small dots at approximately 80% of the connection radius (see Figure 5.7). Subsequently, it forms a crescent shape that propagates towards the middle of the connection and finally covers the entire surface. The only part that remains transparent is a very thin layer of the outer ring of the connecting surface. In Figure 5.6, the start of the whitening phenomenon has been noted on the graph. Regarding the failure of the connections, all of the specimens failed cohesively within the adhesive. Figure 5.8 illustrates the failure pattern of the circular connections. In some specimens, the highly stressed areas are visible after failure at 80-90% of the connection radius.



Figure 5.7: Propagation of whitening under tensile static loading



Figure 5.8: Pictures of tested specimens under monotonic loading after failure

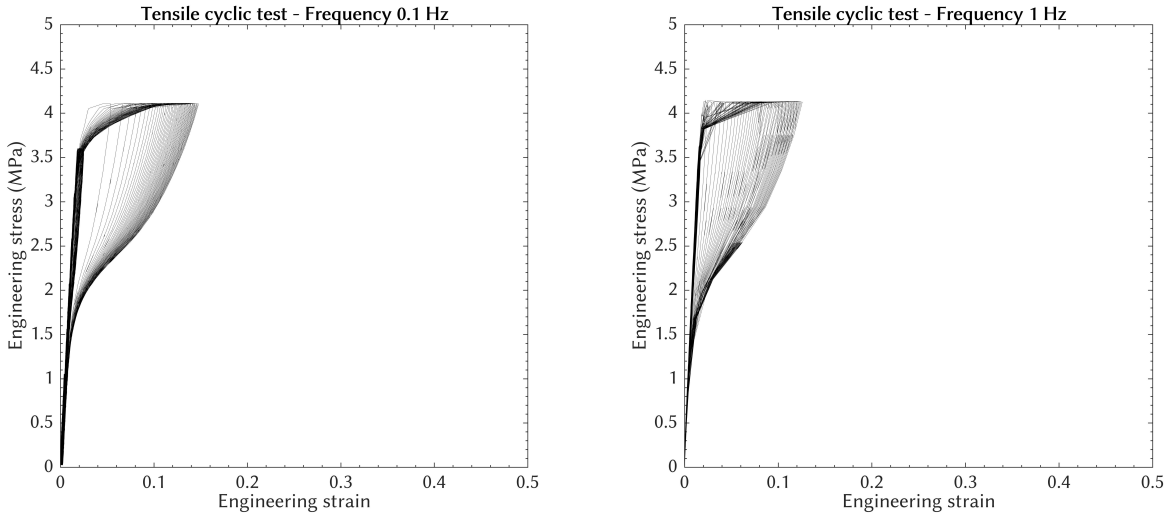
The averaged whitening and failure load levels (F_w and F_u respectively) recorded during the static tests are given in Table 5.2. The whitening load (F_w) represents the load level where the first white spots became visible. The results are also expressed in terms of engineering stresses ($\sigma_w$and σ_u). The whitening load levels are recorded using the video footage of the static tests.

Table 5.2: Test results of TSSA laminated connections subjected to tensile static loading

Test type	Number of tests	Whitening		Failure			
		F_w (KN)	$\sigma_{eng,w}$ (MPa)	F_u (KN)	$\sigma_{eng,u}$ (MPa)	St. dev. (KN)	COV (-)
Tensile static	3	5.72	2.91	10.53	5.36	1.13	0.108

5.2.2 Cyclic tests

Figures 5.9(a) and (b) show the mechanical response of the circular TSSA connections under repeated loading cycles for 0.1Hz and 1Hz respectively. In both cases, the stress-softening phenomenon becomes clearly visible when the maximum (engineering) stress level reaches 4 MPa. The softening appears to increase as the number of loading cycles increases. During the loading cycles, the whitening phenomenon is observed. As in the case of monotonic loading, whitening starts to develop in small dots at approximately 80% of the connection radius and then propagates towards the middle. During the final cycles, the entire surface of the connection turns completely white, leaving a very thin outer ring still transparent (see Figure 5.16). When the load is removed, the white color always disappears completely. Further discussion about the whitening effect is provided in Section 5.3. The failure pattern of the adhesive shows that all specimens failed cohesively within the adhesive, as shown in Figure 5.10. From the pictures it is obvious that all of the tested specimens returned to their transparent state after failure.



(a) (b)

Figure 5.9: Tensile cyclic loading test results at: (a) Frequancy 0.1 Hz, (b) Frequency 1 Hz

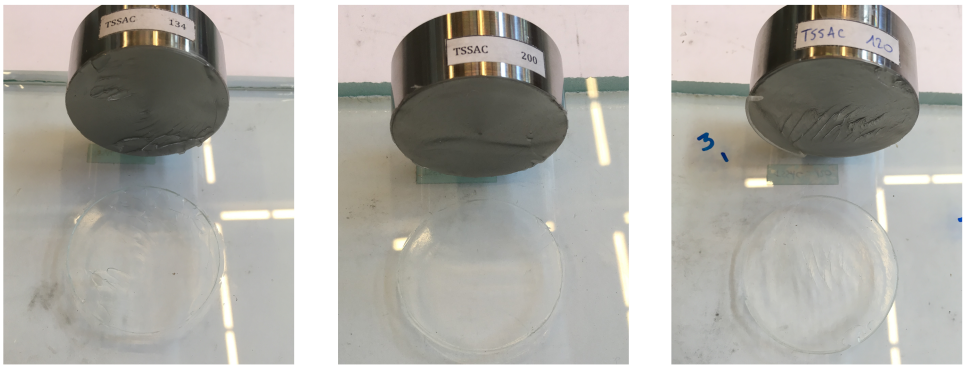


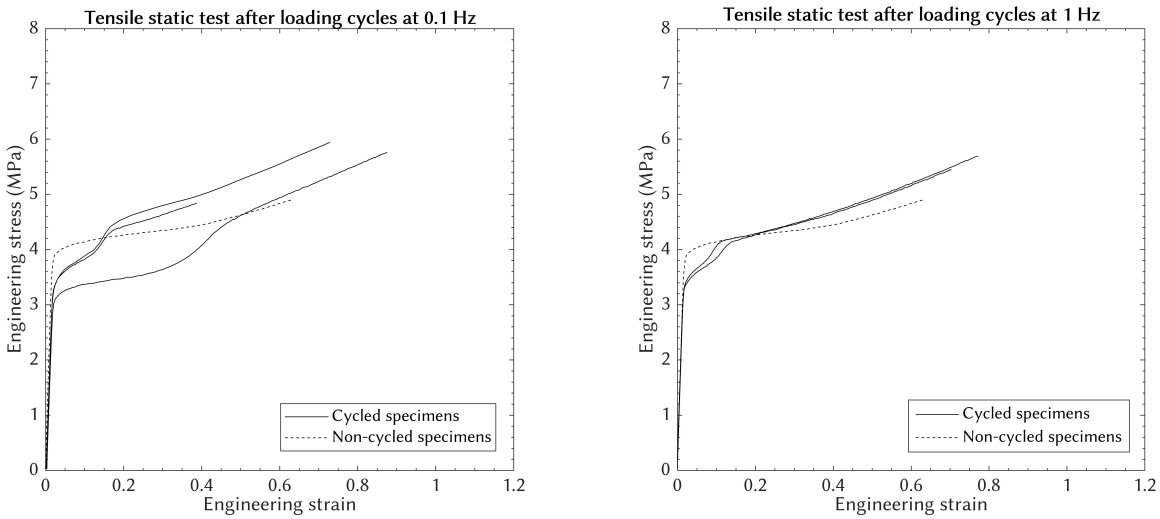
Figure 5.10: Pictures of tested specimens under cyclic loading after failure

The whitening load levels (F_w) and engineering stresses (σ_w) recorded during the cyclic tests are given in Table 5.3. For cyclic tests at 1 Hz, the precise whitening load level is difficult to be determined due to the limited accuracy of the camera used. In two out of three tests the first white spots were recorded in the first cycles from 0 to 6KN (or 0 to 3 MPa).

Table 5.3: Test results of TSSA laminated connections subjected to tensile cyclic loading

Test type	Number of tests	Whitening	
		F_w (KN)	σ_w (MPa)
Tensile cyclic at 0.1 Hz	4	4.77	2.42
Tensile cyclic at 1 Hz	3	< 6.12 > 5.10	< 3.12 > 2.60

The cycled specimens were also subjected to static loading tests until failure. Figure 5.11 illustrates the mechanical response of the cycled (continuous lines) and non-cycled (dotted lines) specimens at a displacement rate of 1mm/min. It appears that the stress-softening phenomenon also influences the monotonic behaviour of the adhesive, showing that a permanent damage takes place. The stress-stain curves overlap for loads up to 3 MPa, but above this point the response of the cycled specimens starts to diverge showing a softening behaviour. Above approximately 4 MPa (the maximum level of the loading cycles), the response of the cycled specimens returns to the path of the virgin (non-cycled) material while showing some hardening.



(a) (b)

Figure 5.11: Tensile static tests after loading cycles at: (a) 0.1 Hz and (b) 1 Hz

Table 5.4: Test results of TSSA laminated connections subjected to tensile static tests (after being cyclic loading)

Test type	Number of tests	Whitening		Failure			
		F_w (KN)	σ_w (MPa)	F_u (KN)	σ_u (MPa)	St. dev. (KN)	COV (-)
Tensile static after loading cycles at 0.1 Hz	3	4.64	2.36	10.82	5.51	1.16	0.107
Tensile static after loading cycles at 1 Hz	2	5.15	2.62	10.94	5.57	0.34	0.031

5.2.3 Healing

The behaviour of cycled specimens after a rest period is also examined. Specimens are subjected to 50 loading cycles from 0 to 3.8 MPa, in order to generate the Mullins effect. Subsequently, the specimens are left to rest for a period of 3 days and then the test is repeated again. Figure 5.12 shows the mechanical response of the adhesive before and after the rest period. It appears that the stiffness has not recovered with time, a fact which indicates that at room temperature the stress-softening phenomenon causes permanent damage. Event though, the damage due to the Mullins effect appears to be irreversible, more tests are needed in order to form more solid conclusions.

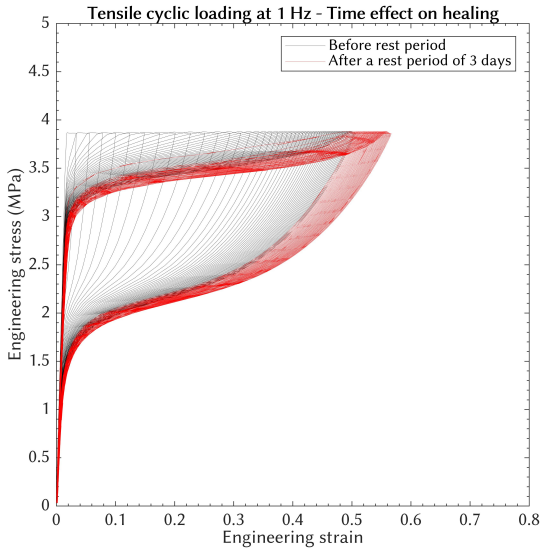


Figure 5.12: Tensile test results related to healing of the stress-softening phenomenon

5.3 Analysis and discussion

The circular TSSA laminated connections have been subjected to cyclic tensile loading of increasing maximum limit. Figure 5.13 illustrates the mechanical response of the adhesive recorded for the first and last cycle for each stress level above 2.5 MPa. The results show that for loading cycles up to 3 MPa, the loading and unloading curves overlap, meaning that response of the material is (almost) perfectly linear. When the maximum load increases to 3.5 MPa, we can observe a small deviation between the curves representing the first (continuous line) and the last cycle (dotted line), a fact which indicates the beginning of the stress-softening effect. More severe softening is observed during the loading cycles up to engineering stresses of 4 MPa. The softening behaviour of the material appears to increase dramatically as the maximum load increases from 3.5 to 4 MPa and continuous to increase with the number of cycles. Nevertheless, as it appears from Figure 5.13, TSSA does not exhibit any permanent deformations under cyclic loading.

In Appendix B, the test results of the specimens subjected to tensile loading cycles are given in more detail. Most of the specimens that showed significant softening also failed before the completion of 400 cycles, a fact that could indicate a relation between the softening phenomenon and resistance against fatigue. However, further research is required to verify such a hypothesis.

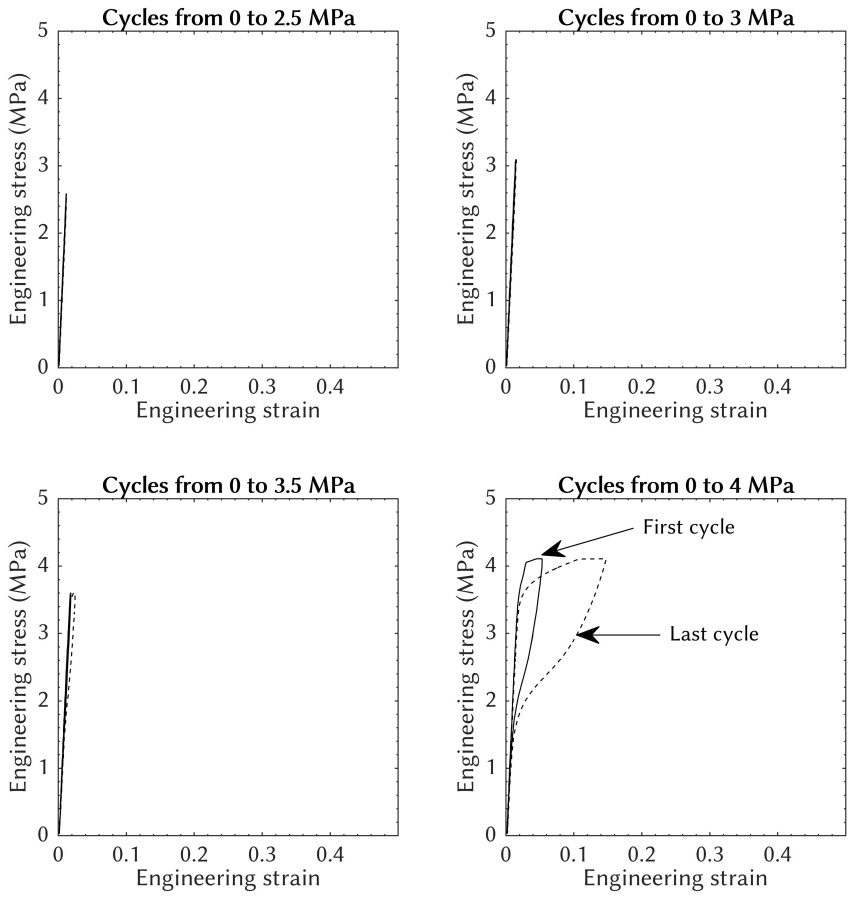


Figure 5.13: Plot of the first and last cycle for every load level

During the cyclic tests the whitening phenomenon appears. The first white spots became visible at 17% lower stress level than that recorded during the static tests. However, the development of whitening in cyclic and static loading appears to be very similar. As already mentioned in the previous section, the phenomenon starts with small white spots and as the load increases the whole adhesive surface turns white. In both cases, a very thin transparent ring is observed close to the perimeter. This shows that the edge of the connection is not constrained in the radial direction as is the middle part. In the work of Santarsiero et al. [1, 18], the whitening phenomenon observed in tensile tests is attributed to the large hydrostatic component of the stress tensor, which in turn is the result of the confined state of the adhesive.

In case of circular connections that undergo tensile forces, the largest part of the adhesive is subjected to a confined state, because the transversal (radial and tengential) deformations are fully or almost fully constrained [1, 18, 52]. Therefore, imposing a tensile load to the connection induces stresses in the longitudinal but also in the transversal directions (see Figure5.14(b)). Close to the perimeter, the adhesive is not constrained in the radial direction (x direction) and thus it is free to to deform (see Figure5.14(c)). Due to the confinement effect the adhesive exhibits higher stiffness than the modulus of elasticity [1, 18, 52]. Based on this approach, the transversal stresses in the confined state have the same magnitude and can be expressed in function of the applied stress (σ_z) and of the Poisson's ratio

(v). The fact that the transversal stresses are not zero and have the same magnitude results in a large hydrostatic component of the stress tensor.

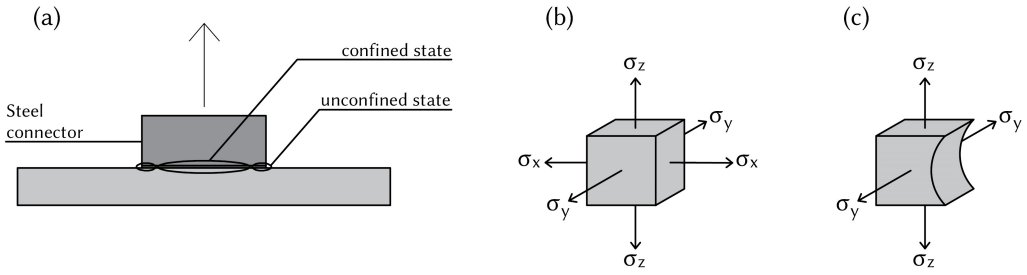


Figure 5.14: Scheme of the confinement effect: (a) region of confined and unconfined state, (b) confined state along x-axis and (c) unconfined state along x-axis

Numerical analysis performed by Santarsiero [1], for TSSA circular connections with diameter 50mm, showed that the development of the whitening phenomenon is in fact proportional to the hydrostatic stresses. In Figure 5.15, the hydrostatic stress is plotted over the diameter of the connection. The stress distribution is not uniform and the maximum value is observed approximately at $0.8R$, a fact which agrees with the position where the first white spots became visible. High hydrostatic stress is also observed in the middle of the connection (for $r < 0.8R$), a fact which explains the propagation of whitening first towards the middle of the connection and last in the region close to the perimeter. Furthermore, the value of the hydrostatic stress in the perimeter of the connection is nearly zero even for loads close to failure, a fact which could justify the small outer ring that remains transparent throughout the test.

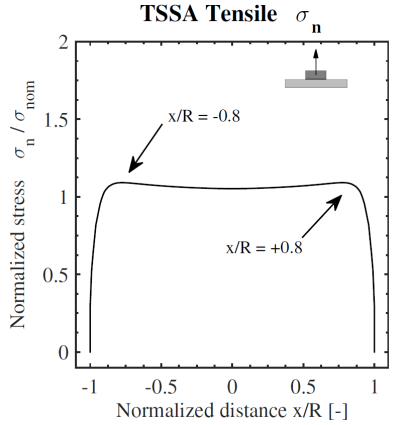


Figure 5.15: Plot of the normalized hydrostatic stress versus the normalized distance of the connection at load level close to failure [1]

Figure 5.16 illustrates the development of the whitening phenomenon under loading cycles. For loading cycles up to 3 MPa, whitening appears in a crescent shape at 80% of the radius. As the cycles increase, whitening appears in the same position and shows a small spread around this point. When

the maximum stress exceeds 3 MPa, the whitening effect seems to spread faster and in the end covers the entire surface, leaving a small ring at the perimeter still transparent. It must be noted that in all of the cycles performed, the whitening completely disappeared when the load was removed, leaving no trace of whitened surface.



Figure 5.16: Whitening effect propagation under loading cycles

The propagation of whitening and the stress level it appears proved to be consistent for most of the specimens. Inconsistencies are observed in defected specimens that failed earlier than expected and showed more sever softening behaviour. In the work of Sitte et al. [7] this is considered as a positive feature, as the whitening pattern may provide an indication of the quality of bonding without destroying the connection. An example of a defected specimen that exhibited inconsistencies with regard to the whitening propagation and failed earlier than the rest of the specimens is given in Figure 5.17.

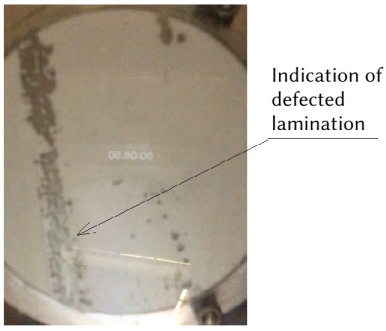


Figure 5.17: Whitening effect of a defected connection

5.4 Conclusions

In this chapter the static and cyclic mechanical response of TSSA circular connections under tensile load is studied. The propagation of the whitening phenomenon inside the adhesive is also investigated. From the experimental results, the following conclusions can be drawn.

First, the mechanical response of the adhesive changes if it is stressed above 3.5 MPa. The Mullins effect is observed, where the adhesive shows severe stress-softening during the unloading phase. Some softening is also observed during reloading; however it is less pronounced. The damage due to stress-softening appears to be irreversible. The permanent damage caused by the Mullins effect at room temperature, requires further research to understand the relation between the softening phenomenon and resistance against fatigue. Nevertheless, softening appears at load levels which are considerably higher than the design limit proposed by the manufacturer, Dow Corning, as well as higher than load level when whitening first appears. Since the whitening pilots the design stress, stress-softening can be considered to occur above the working limit of the connection.

Second, the development of the whitening phenomenon is similar both under the static and cyclic loading. The first white spots become visible at 80% of the connection radius, then the whitening propagates towards the middle and finally spreads to the area close to the perimeter. Under cyclic loading, the whitening appears to propagate faster after the maximum stress level of 3.5 MPa is reached. Most importantly, it shows some consistency to a certain stress state and completely disappears when the load is removed.

Chapter 6

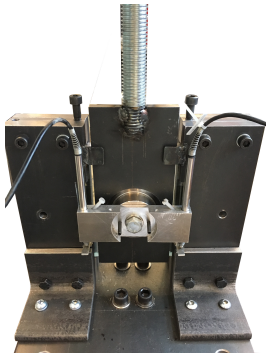
Assessment of hyperelastic material models

6.1 Introduction

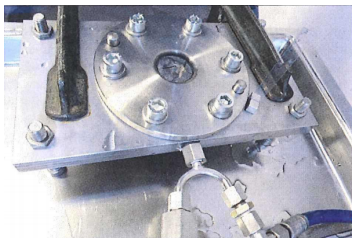
When numerically analyzing adhesive point-fixings using a finite element software, the accuracy of the results largely depends on the predefined material model. The glass and steel elements of the connection can be simulated with linear elastic properties; however, adhesives, such as TSSA, often show strong nonlinearities. Therefore, there is a need for specific mathematical expressions to describe their deformation behaviour. The suitability of the model is assessed by curve fitting various mathematical expressions to experimental data often coming from uniaxial or equibiaxial tests [31].



(a) Uniaxial tests performed by Santarsiero [1]



(b) Shear tests performed for the purpose of this study



(c) Biaxial (bulge) test performed by Drass et al. [13, 14]

Figure 6.1: Tests to be considered for the assessment oh hyperelastic material models

The curve fitting process should not be based on a single experiment, because even if a material model can describe very accurately the experimental data, it may fail to reproduce the behaviour of other loading states [30]. In this case, experimental data coming from three deformation states will be considered. The results of the shear tests conducted for this study will be combined with data from uniaxial tension and biaxial tests conducted by Santarsiero [1, 8] and Drass et al. [13, 14], respectively (see Fig-

ure 6.1). Material models with maximum three parameters are going to be considered, since larger number of parameters also requires a larger experimental database to be fitted.

6.2 Methodology

6.2.1 Basic methodology

In Chapter 3, the fundamental theory of hyperelasticity was presented and several commonly used models were discussed. The curve fitting process requires the reformulation of the strain energy functions in terms of engineering stresses and strains. In large strain problems, based on the finite deformation theory, the stress state of rubbers can be expressed either in terms of the Cauchy (or true) stress tensor σ or of the 1^{st} Piola-Kirchhoff tensor P. The relation between the stress tensors is given in Equation (6.1). The Cauchy stress tensor defines the stress state of the body in the deformed state, whereas the 1^{st} Piola-Kirchhoff tensor defines the stress state relative to the reference configuration. The 1^{st} Piola-Kirchhoff stresses are also referred to as engineering stresses. In literature, one can find the stress state of rubbers expressed also in Biot (or nominal) stresses t_i. For common deformation states imposed experimentally to adhesive foils, such as uniaxial or biaxial tension and compression or simple shear, the Biot stresses are equal to the 1^{st} Piola-Kirchhoff stresses since no rotation of the rigid body takes place under these tests (see Equation (6.2)).

$$P = J\sigma F^{-T} \tag{6.1}$$

$$T = R^T P \tag{6.2}$$

Where:

- J the Jacobian of the deformation gradient tensor ($J = det(F)$)
- σ the Cauchy stresses tensor
- F the deformation gradient tensor
- T the Biot stress tensor
- R the rotation matrix, equal to the identity matrix I for commonly tested deformation states

It is common to assess the behaviour of elastomeric materials based on their undeformed state since experimental data are expressed in terms of engineering stresses and strains. For this reason, the derivation of the 1^{st} Piola-Kirchhoff stresses is considered more suitable for the curve fitting process. Although, this tensor is more suitable for the calibration of the various hyperelastic models, it does not provide any physical interpretation and thus the Cauchy stress tensor provides more insight when numerically analyzing rubber materials [36].

The principal Cauchy stresses σ_i ,$i\epsilon\{1, 2, 3\}$ are related to the strain energy density according to Equation (6.3). [53, 35, 30, 32, 14]

$$\sigma_i = \lambda_i \frac{\partial W(\lambda_1, \lambda_2, \lambda_3)}{\partial \lambda_i} - p \tag{6.3}$$

Where:

p is a Lagrange multiplier / the hydrostatic pressure, which arises from the constraint $\lambda_1\lambda_2\lambda_3 = 1$

The corresponding Biot (or engineering) stresses, which are measured directly in experiments are given in Equation (6.4). [53, 35, 30, 32, 14]

$$t_i = \frac{\partial W(\lambda_1, \lambda_2, \lambda_3)}{\partial \lambda_i} - p\lambda_i^{-1} \equiv \sigma_i \lambda_i^{-1} \tag{6.4}$$

If deformation is applied to a thin sheet of material (e.g. uniaxial tension, simple shear or biaxial tension) then the material is under a plane stress condition and thus $\sigma_3 = 0$, which is the stress normal to the plane of the sheet [53]. For adhesives undergoing a bulge (biaxial) test, this is also the case if the the thickness of the sheet is significantly smaller than the lateral dimensions. If $t << h$ and $t << a$, then the pressure p on the sheet material is significantly smaller than the Cauchy stresses σ and thus a plane-stress state can be assumed (see Figure 6.2). Based on the plane stress assumption, the Biot (or engineering) stresses for each deformation state are the following.

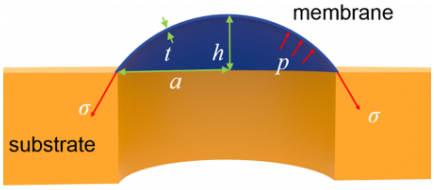


Figure 6.2: Schematic diagram of the bulge test method [54]

Uniaxial tension

For uniaxial tension we set $\sigma_1 = \sigma$ and $\sigma_2 = \sigma_3 = 0$. The incompressibility assumption yields $\lambda_2 = \lambda_3 = \lambda_1^{-1/2}$ ($\lambda_1 = \lambda$). Based on the incompressibility and the plane-stress assumption the p can be eliminated from Equation (6.3).

$$W_{iso}(\lambda_1, \lambda_2) = W(\lambda_1, \lambda_2, \lambda_1^{-1}\lambda_2^{-1}) \tag{6.5}$$

$$\sigma_1 - \sigma_3 = \lambda \frac{\partial W_{iso}}{\partial \lambda} \tag{6.6}$$

$$t_1 = \frac{\partial W_{iso}}{\partial \lambda} = \frac{\partial W_{iso}}{\partial I_1}\frac{\partial I_1}{\partial \lambda} + \frac{\partial W_{iso}}{\partial I_2}\frac{\partial I_2}{\partial \lambda} \tag{6.7}$$

Equibiaxial tension

For equibiaxial tension we have $\sigma_1 = \sigma_2 = \sigma$ and $\lambda_3 = \lambda_1^{-2} = \lambda_2^{-1}$ ($\lambda_1 = \lambda_2 = \lambda$). In the same way as uniaxial tension, we have:

$$\sigma - \sigma_3 = \lambda \frac{\partial W_{iso}}{\partial \lambda} \tag{6.8}$$

$$t = t_1 = t_2 = \frac{1}{2}\frac{\partial W_{iso}}{\partial \lambda} = \frac{1}{2}\frac{\partial W_{iso}}{\partial I_1}\frac{\partial I_1}{\partial \lambda} + \frac{1}{2}\frac{\partial W_{iso}}{\partial I_2}\frac{\partial I_2}{\partial \lambda} \tag{6.9}$$

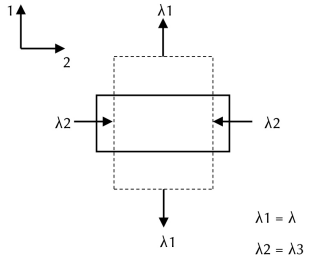
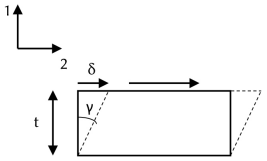
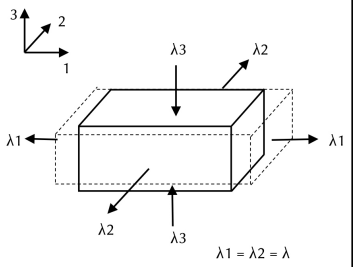
Simple shear

For simple shear we have $\lambda_1 = \lambda_2 = \lambda_3 = 1$. According to Mooney [35] the engineering shear stresses are expressed as a function of the amount of shear γ.

$$t_{12} = \frac{\partial W_{iso}}{\partial \gamma} = \frac{\partial W_{iso}}{\partial I_1}\frac{\partial I_1}{\partial \gamma} + \frac{\partial W_{iso}}{\partial I_2}\frac{\partial I_2}{\partial \gamma} \tag{6.10}$$

The deformation gradient tensor and the stress reformulations for each deformation state (uniaxial, shear and biaxial) are summarized in Table 6.1. The equations describing the engineering (or Biot) stresses t_i can be further developed for any expression of W_{iso}, meaning for every hyperelastic model available in literature which is based on the strain invariants. In this case, the Neo-Hooke, Mooney-Rivlin (with two and three parameters), Yeoh and Gent-Thomas models are going to be assessed based on their ability to reproduce the deformation behaviour of TSSA. The complete derivation of the engineering stresses for each deformation state and for each one of the above mentioned models is given in Appendix C.

Table 6.1: Derivation of stresses for the uniaxial, shear and equibiaxial tension tests

Uniaxial tension	Simple shear	Equibiaxial tension
		
$F = \begin{bmatrix} \lambda_1 & 0 & 0 \\ 0 & \lambda_2 & 0 \\ 0 & 0 & \lambda_3 \end{bmatrix} = \begin{bmatrix} \lambda & 0 & 0 \\ 0 & \lambda^{-1/2} & 0 \\ 0 & 0 & \lambda^{-1/2} \end{bmatrix}$	$F = \begin{bmatrix} 1 & \gamma & 0 \\ 0 & 1 & 0 \\ 0 & 0 & 1 \end{bmatrix}$	$F = \begin{bmatrix} \lambda & 0 & 0 \\ 0 & \lambda & 0 \\ 0 & 0 & \lambda^{-2} \end{bmatrix}$
$\bar{F} = F$ (incompressibility assumption)	$\bar{F} = F$ (incompressibility assumption)	$\bar{F} = F$ (incompressibility assumption)
$\bar{I}_3 = \det(\bar{F}) = \lambda_1\lambda_2\lambda_3 = 1$	$\bar{I}_3 = \det(\bar{F}) = 1$	$\bar{I}_3 = \det(\bar{F}) = 1$
$\bar{B} = \begin{bmatrix} \lambda^2 & 0 & 0 \\ 0 & \lambda^{-1} & 0 \\ 0 & 0 & \lambda^{-1} \end{bmatrix}$	$\bar{B} = \begin{bmatrix} 1+\gamma^2 & \gamma & 0 \\ \gamma & 1 & 0 \\ 0 & 0 & 1 \end{bmatrix}$	$\bar{B} = \begin{bmatrix} \lambda^2 & 0 & 0 \\ 0 & \lambda^2 & 0 \\ 0 & 0 & \lambda^{-4} \end{bmatrix}$
$\bar{I}_1(\bar{B}) = 2\lambda_1^{-1} + \lambda_1^2$ $\bar{I}_2(\bar{B}) = \lambda_1^{-2} + 2\lambda_1$	$\bar{I}_1(\bar{B}) = 3 + \gamma^2$ $\bar{I}_2(\bar{B}) = 3 + \gamma^2$	$\bar{I}_1(\bar{B}) = 2\lambda^2 + \lambda^{-4}$ $\bar{I}_2(\bar{B}) = \lambda^4 + 2\lambda^{-2}$
$t_{11} = 2(1-\lambda_1^{-3})[\lambda_1 \frac{\partial W_{iso}}{\partial I_1} + \frac{\partial W_{iso}}{\partial I_2}]$	$t_{12} = 2\gamma[\frac{\partial W_{iso}}{\partial I_1} + \frac{\partial W_{iso}}{\partial I_2}]$	$t_{11} = t_{22}$ $= 4(\lambda - \lambda^{-5})\frac{\partial W_{iso}}{\partial I_1} + 4(\lambda - \lambda^{-3})\frac{\partial W_{iso}}{\partial I_2}$

The calibration of the material parameters is based on the non-linear least square optimization method. The stress-strain curves derived from the shear tests are averaged by means of a Matlab® script that interpolates between the ordinate values of each dataset and subsequently averages the corresponding abscissa values. A Matlab® script is also developed for the curve fitting process. The material constants are calculated based on each dataset individually (e.g uniaxial, shear, equibiaxial) but also on combination of datasets (e.g. uniaxial & shear & equibiaxial). The accuracy of the material model is increased when datasets from multiple deformation states are taken into account, because in this case a single set of material parameters is used to describe all deformations states. The fitting process is based on the least squares method that calibrates the material constants by minimizing the value of the error function E. The error function is expressed in Equation (6.11) for the case when all above mentioned deformation states are taken into account for the curve fitting process. The Matlab® functions *Lsqcurvefit* and *Lsqnonlin* were used for this purpose. Matlab® also offers the option to minimize the error either using the 'Trust-region-reflective' or the 'Levenberg-Marquardt' algorithm. For both cases the results were the same.

$$E = \sum_{i=1}^{n_{UT}} (\sigma_i^{test} - \sigma_i^{theoretical})^2 + \sum_{j=1}^{n_S} (\sigma_j^{test} - \sigma_j^{theoretical})^2 + \sum_{k=1}^{n_{ET}} (\sigma_k^{test} - \sigma_k^{theoretical})^2 \tag{6.11}$$

Where:

n_{UT}, n_S, n_{EB} the number of data points of uniaxial tension, shear and equibiaxial tension tests respectively.

The fitting of each model to the experimental data is assessed by introducing the coefficient of determination R^2, which takes the value of 1 in the case of perfect fitting.

$$R^2 = 1 - \frac{\sum (y_i - \hat{y_i})^2}{\sum (y_i - \overline{y})^2} \tag{6.12}$$

Where:

$y_i, \hat{y_i}, \overline{y}$ the test data, the model data and the average value of the test data, respectively.

The relative error for every data point is also calculated, in order to assess the performance of each model throughout the deformation field of the adhesive.

$$error = |\frac{\sigma_i^{theoretical}}{\sigma_i^{test}} - 1| \tag{6.13}$$

The methodology for curve fitting hyperelastic models to experimental data coming from static tests is summarized in the algorithm of Figure 6.3.

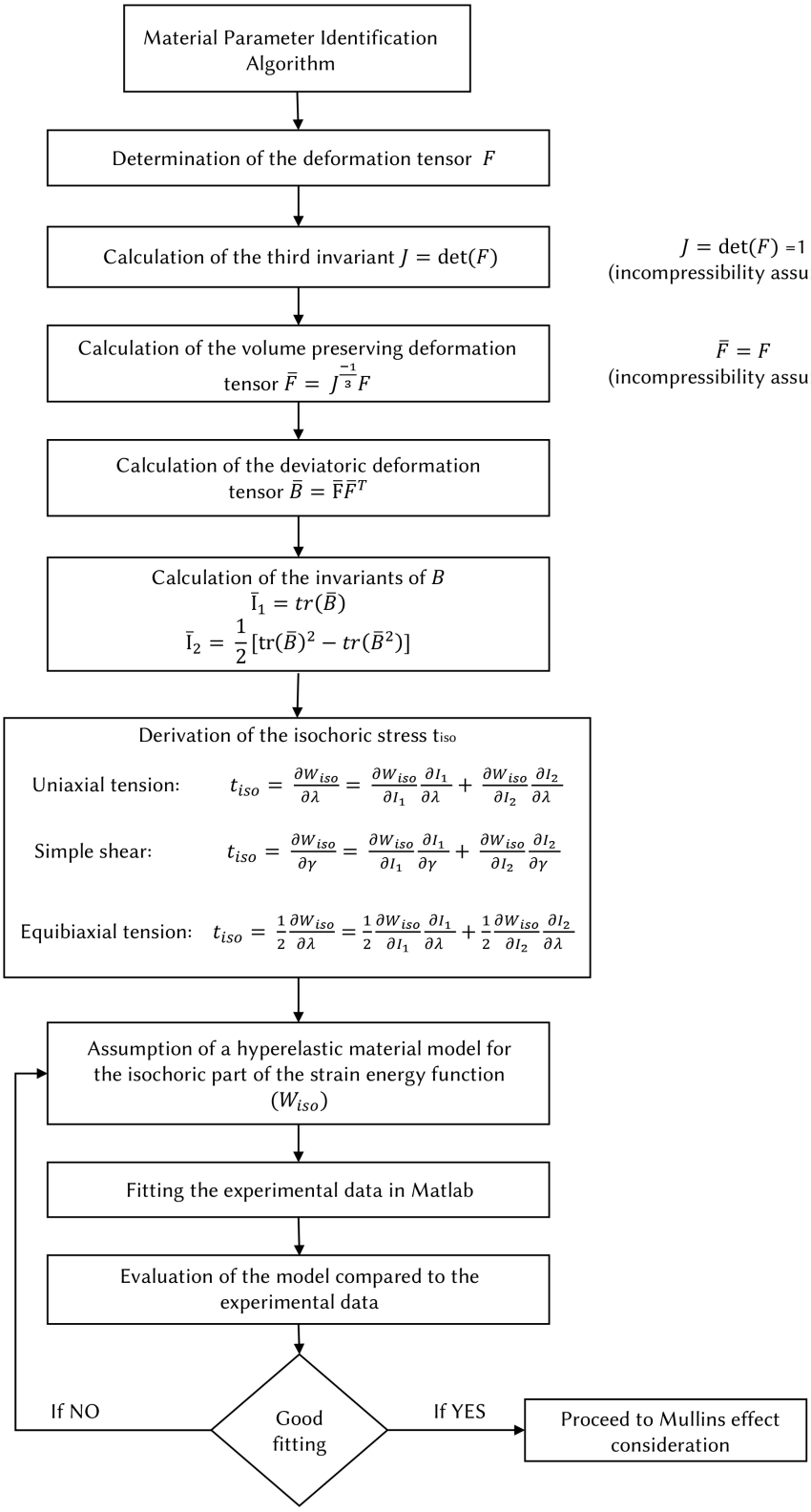


Figure 6.3: Material parameter identification algorithm

6.2.2 Methodology for describing the stress-softening phenomenon

Having described the basic methodology for calibrating material constants in order to describe simple monotonic tests, the next step is to model the changes in the behaviour of the adhesive under cyclic loading. The shear tests of circular connections showed that TSSA undergoes a stress-softening phenomenon, meaning that the stiffness of the adhesive changes significantly when loaded cyclically. More specifically, tests showed that the softening behaviour of the adhesive becomes more severe as the maximum load applied increases. As already mentioned in Section 3.6, no material models currently exist that account for changes in the deformation behaviour when repetitive loading is applied, as well as there are no models that can be expressed as a function of the previously applied maximum load. Therefore, it remains at the discretion of the engineer to choose which loading and unloading curves will provide more insight to a particular problem or application.

Figure 6.4 illustrates a simplified approach on how to model the behaviour of TSSA considering the Mullins effect. The static behaviour of TSSA is modeled based on the methodology described in Section 6.2.1. During the first loading, the deformation of the material follows the static curve; however for any subsequent unloading or reloading the mechanical response of the adhesive changes, as illustrated below.

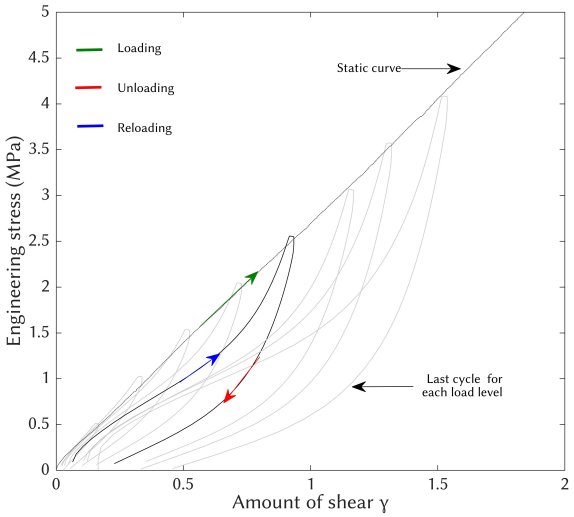
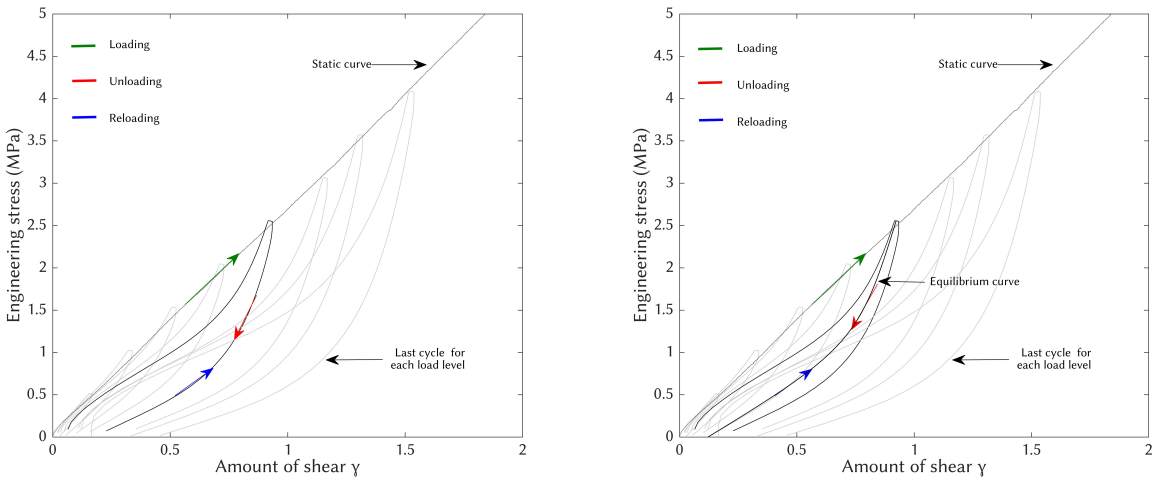


Figure 6.4: Simplified model that accounts for the stress-softening phenomenon

Material models that are currently supported by finite element software, such as the Ogden- Roxburgh, do not account for different unloading and reloading branches and thus for cases such as the one observed for TSSA, the problem should be further simplified. Two approaches are possible and these are illustrated in Figure 6.5. In the first case (see Figure 6.5(a)), it is assumed that the reloading of the material follows the unloading branch and thus a “worst case scenario” in terms of stiffness is taken into account. On the other hand, an equilibrium curve may be constructed [36], which represents the average of the unloading and reloading response and thus it can serve for the simulation of the stress-softening phenomenon (see Figure 6.5(b)). In this study, the first case is considered more appropriate in terms of safety.



(a) (b)

Figure 6.5: Simplified approaches for the modeling of the stress softening phenomenon

The Ogden - Roxburgh model oversimplifies the deformation behaviour of TSSA. Guo [32] proposed a model that considers a different loading and reloading mechanical response. In this study, the model of Guo is also calibrated and compared with the experimental results of TSSA. The goal is to find if this model approaches better the actual response of Figure 6.4. In this way, a less conservative approach may be adopted for the simulation of the deformation behaviour of TSSA. The performance of the Guo model is discussed in the next following section.

The curve fitting process is based on the minimization of the error according to the nonlinear least squares optimization method. The coefficient of determination R^2 is again used for the assessment of the damage model. It must be noted that for the calibration of the damage factor for the simulation of the stress-softening phenomenon, the dataset of the stabilized response should be considered. This is because, creep effects may prove to be decisive for the deformation state of the adhesive, and thus it is important that the model reproduces the behaviour of the adhesive at its stabilized state, when the stress-strain curves do not change significantly with the number of cycles. As it was pointed out in Section 4.3, for shear loading up to 1.5 MPa the dissipated energy stabilizes until the 50^{th} cycle. For higher loads, even though the rate of increase of the dissipated energy is decreasing with the number of cycles, the energy is clearly not stabilized yet at the 50^{th} cycle. In this study, damage parameters will be calibrated for all the load levels tested; however for loading cycles with maximum engineering stresses above 1.5 MPa, these parameters should be used with great care to provide only an indication of the behaviour of the adhesive at the 50^{th} cycle. For future research it is recommended that more cycles are performed, in order to calibrate the damage model based on the stabilized state of the adhesive.

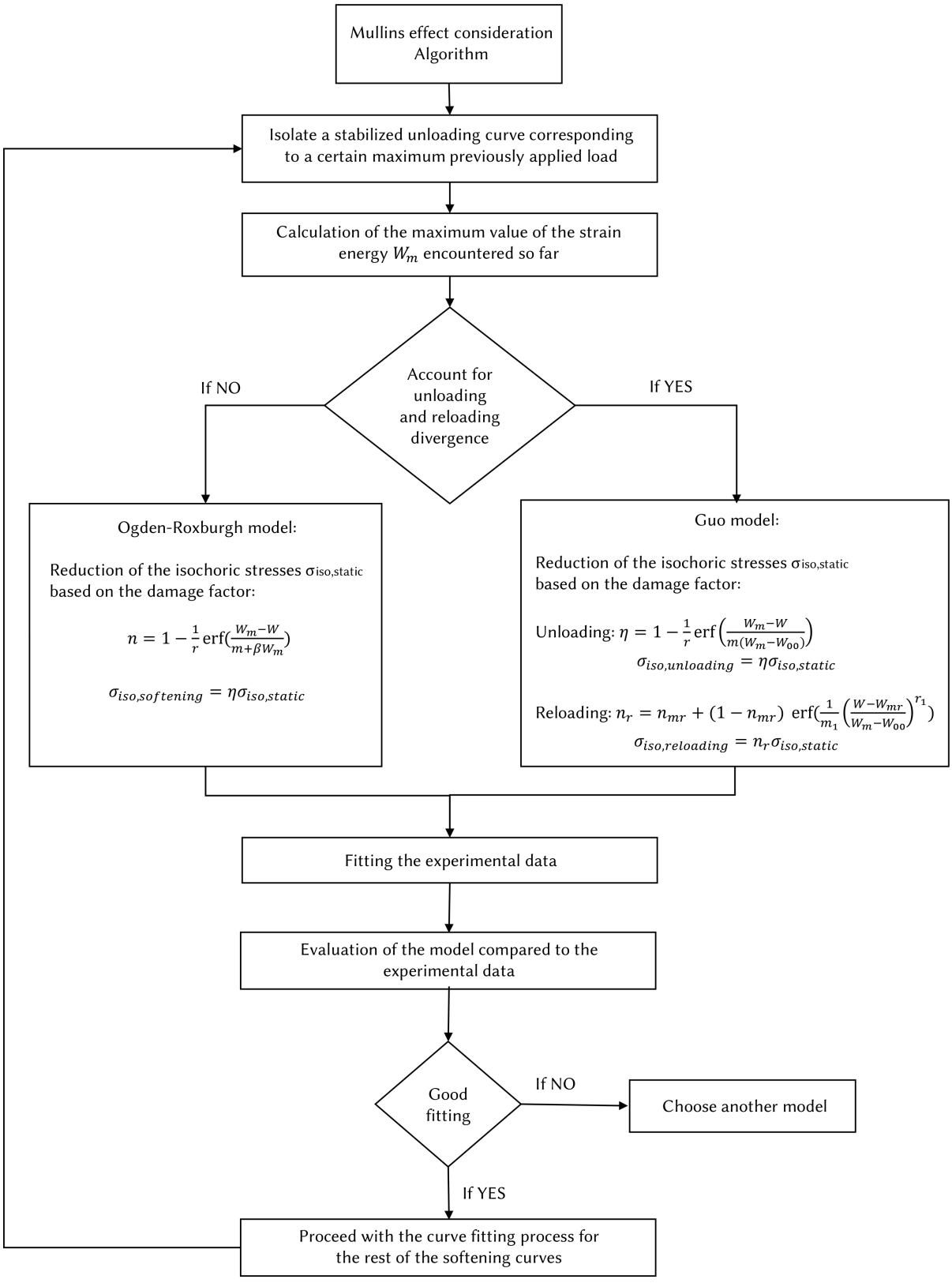


Figure 6.6: Mullins effect consideration algorithm

6.3 Results and discussion

Figure 6.7 shows the performance of the selected hyperelastic models for describing the uniaxial, shear and biaxial stress state of the adhesive. It is evident that the Yeoh model fails to reproduce all three deformation states, as well as that the three-parameter Mooney-Rivlin model fails to approach the biaxial stress-strain behaviour of TSSA. This can be explained by the fact that higher order material models, such as the Yeoh and the three-parameter Mooney-Rivlin model, are intended for large deformations and often show poor performance at small strains. TSSA exhibits maximum strains of the order of 140% to 200%, whereas high order models, such as the Yeoh model, are intended for fitting over a large strain range, such as 400% to 700%.

The rest of the models show a very good performance in shear, but they become weaker in uniaxial and even more in biaxial tension. The Gent-Thomas model appears to reproduce better the uniaxial tension data, whereas for the case of biaxial tension it is difficult to clearly distinguish which model performs best. Their performance though appears to be very similar for stretches up to 180%.

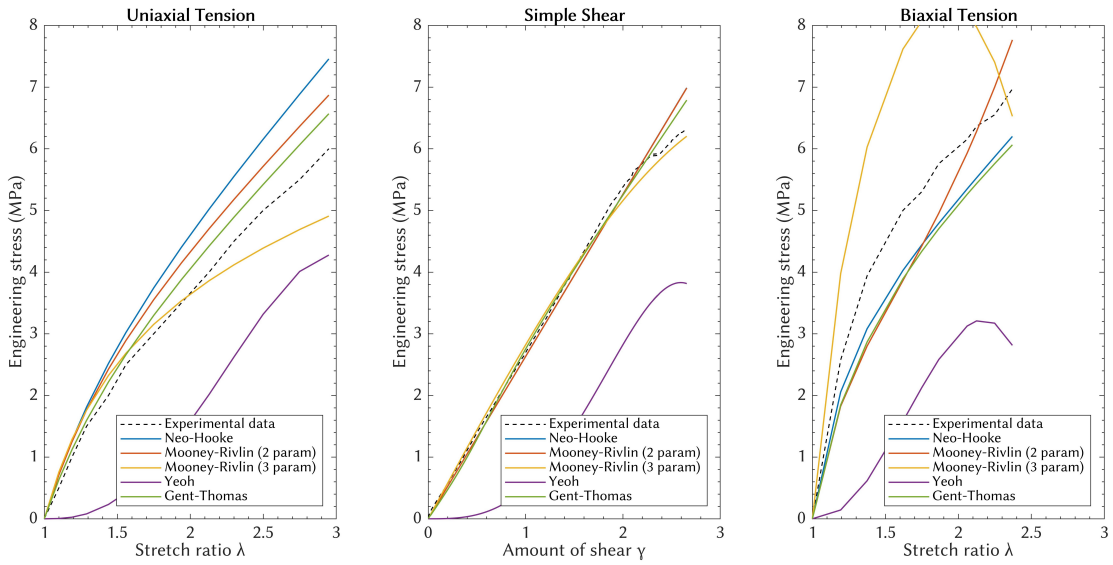


Figure 6.7: Performance of hyperelastic models fitted based on uniaxial, shear and biaxial test data

When material constants are calibrated using multiple datasets, there is a compromise between how good the model approaches the experimental data of each deformation state individually but also all datasets simultaneously. Table 6.2 provides the material constants and coefficients of determination R^2[1] for material models calibrated using only one dataset (e.g. only uniaxial tension data) but also all other possible combinations of deformation states. Models that are calibrated based on a single deformation state approach almost perfectly the experimental data of this specific dataset ($R^2 \approx 1$) but perform poorly for the rest of the deformation states. When all three deformation states are included in the curve fitting process, then the error of all three datasets is minimized, leading to a material model that aims to reproduce all deformation states. However, in this case it is difficult to achieve an almost perfect fitting and thus the goodness-of-fit R^2 appears to deviate more with respect to the

[1]The coefficients R^2_{UT}, R^2_S, R^2_{UT} refer to the goodness-of-fit when compared with uniaxial, shear and biaxial test data, respectively.

previous case. In the work of Dispersyn et al. [31], the combination of as many experimental data from different test configurations is disputed. Therefore, the decision for the suitability of a model should also be based on the particular application the adhesive is going to be used.

Table 6.2: Material constants and coefficient of determination of the Neo-Hooke, Mooney-Rivlin and Gent-Thomas material models

Material models	Coeff.	Models are fitted based on:						
		UT	S	BT	UT & S	S & BT	UT & BT	UT & S & BT
Neo - Hooke	C_{10}	1.058	1.317	1.532	1.311	1.320	1.271	1.315
	R^2_{UT}	0.9995	0.7848	0.2810	0.7946	0.7781	0.8547	0.7880
	R^2_S	0.8380	0.9929	0.8863	0.9928	0.9929	0.9880	0.9929
	R^2_{BT}	-2.2100	0.8586	0.9983	0.8512	0.8634	0.7963	0.8563
Mooney-Rivlin	C_{10}	1.058	0.658	1.532	0.874	1.234	1.092	1.159
	C_{01}	$7.9^{*}10^{-6}$	0.658	$1.3^{*}10^{-9}$	0.442	0.084	0.162	0.1554
	R^2_{UT}	0.9995	0.9430	0.2810	0.9922	0.8530	0.9637	0.9076
	R^2_S	0.8380	0.9929	0.8863	0.9929	0.9929	0.9837	0.9929
	R^2_{BT}	0.0195	-0.6697	0.9891	0.2876	0.8958	0.8318	0.8698
Gent-Thomas	C_{10}	1.058	1.116	1.532	1.092	1.215	1.073	1.158
	C_{01}	$1.5^{*}10^{-5}$	0.806	$4.6^{*}10^{-9}$	0.898	0.4295	4.586	0.6500
	R^2_{UT}	0.9995	0.9386	0.2810	0.9957	0.9204	0.9987	0.9671
	R^2_S	0.8380	0.9962	0.8863	0.9962	0.9954	-0.9478	0.9960
	R^2_{BT}	0.0293	0.6610	0.9891	0.7770	0.8298	0.3960	0.8076

From Table 6.2 it can be observed that the fitting of the Neo-Hooke and Gent-Thomas models yields the best results when shear tests or a combination including shear tests is used for the calibration of the material parameters. On the other hand, the Mooney-Rivlin model appears to perform best when at least uniaxial and biaxial data are combined for the curve fitting process. In this case, the consideration of shear tests does not affect significantly the goodness of fit (R^2) and the material constants.

Figure 6.8 illustrates the relative error for every data point. The very large errors observed at small deformations are due to small denominators of the relative error fraction (see Equation (6.13)). In the work of Ogden et al. [53],a relative error of 5% is considered as an upper bound when fitting a model to a single experiment and, in case of fitting two deformation states at the same time, a widened relative error of 20% is considered acceptable. The acceptable relative error is still arguable; however considering the uncertainties during the realization of the tests and the post-processing of the results, such an error may be tolerable [14].

Assessing the overall performance of the hyperelastic models it can be concluded that the Mooney-Rivlin and Gent-Thomas models reproduce best the mechanical response of TSSA. Both models perform very well in shear, but are weaker in uniaxial and biaxial tension. Nevertheless, their performance is very similar for stretches up to 150-180%. At larger stretches close to failure, the models appear to diverge, especially for the case of biaxial tension. The Mooney-Rivlin model results in a smaller relative error (see Figure 6.8); however it fails to approach the deformation behaviour of the adhesive recorded in the tests. On the other hand, the Gent-Thomas model approaches better the stiffness of the adhesive at large strains.

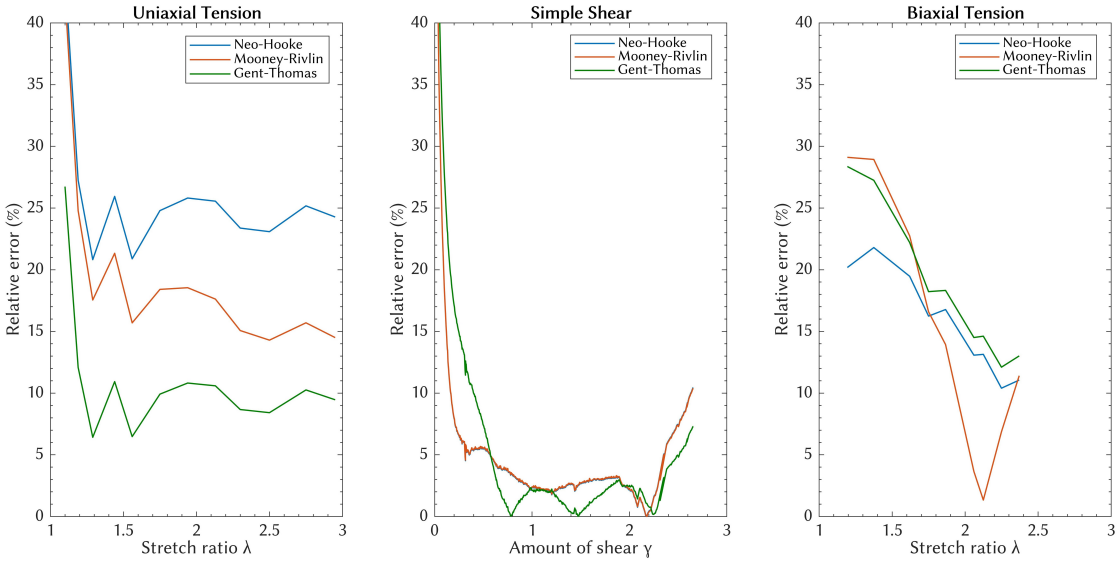


Figure 6.8: Relative error

The next step is to calibrate the damage models for the simulation of the stress-softening phenomenon. Starting with the simplified model that is currently supported by most finite element codes, the Ogden - Roxburgh model is combined with the Mooney-Rivlin or the Gent-Thomas hyperelastic law. In this way, damage parameters are calibrated based on the already defined material constants of Table 6.2 describing the undamaged situation. Figure 6.9 illustrates the performance of the Ogden-Roxburgh damage model compared to the experimental shear data.

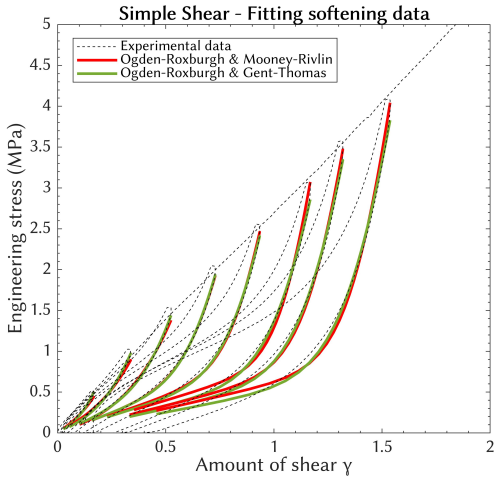


Figure 6.9: Fitting the Ogden-Roxburgh model to the experimental softening data

The fitting of the experimental data appears to be very good. This model though does not consider permanent deformations at the stress-free state and this is the reason it becomes weaker in describing the deformations of the adhesive at low stress levels. This weakness becomes more relevant for loading cycles with high maximum stress levels (above 2.5 MPa), where permanent deformations are larger.

Table 6.3 gives the coefficients of the damage model for (engineering) stress levels up to 1.5 MPa. The coefficients for higher stress levels are given in Appendix C.2; however as already mentioned, they do not describe the stabilized state of the adhesive and should be used only as an indication of the deformation behaviour of TSSA up to the 50^{th} loading cycle.

Table 6.3: Damage coefficients based on the Ogden - Roxburgh model for describing the softening behaviour of TSSA

		Maximum applied engineering stress		
Material models	Coeff.	0.5 MPa	1 MPa	1.5 MPa
Ogden-Roxburgh & Mooney-Rivlin	m	0.591	3.651	0.985
	r	0.256	0.110	0.586
	b	0.201	0.144	0.180
	R^2	0.9640	0.9767	0.9922
Ogden-Roxburgh & Gent-Thomas	m	0.065	0.214	0.230
	r	1.467	1.419	1.320
	b	0.016	$9.55^{*}10^{-9}$	0.500
	R^2	0.9879	0.9943	0.9956

Figure (6.10) shows the performance of the Guo model in describing the actual response of TSSA under cyclic shear loading. Here the fitting for cycles up to maximum stresses of 1.5, 2 and 2.5 MPa is indicatively given. The model reproduces well the behaviour of the adhesive at moderate stress levels, while showing some weakness at cycles performed at very low or very high stresses. Table (6.4) gives the damage coefficients and the goodness-of-fit R^{22} based on the Guo model for stress levels up to 2.5 MPa. For higher stress levels refer to Appendix C.3.

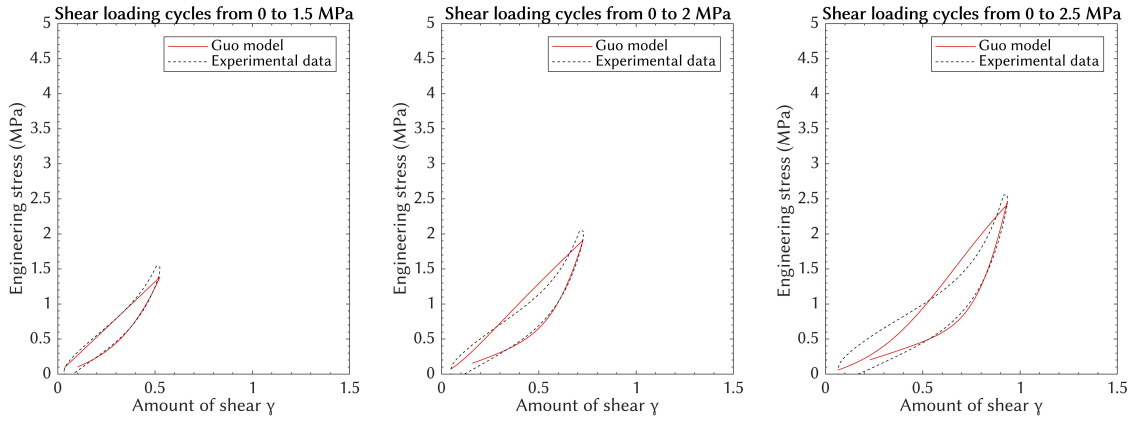


Figure 6.10: Fitting the Guo model to the experimental softening data

[2]The coefficients $R^2_{unloading}$, $R^2_{reloading}$ refer to the goodness-of-fit when compared with unloading and reloading test data, respectively.

Table 6.4: Damage coefficients based on the Guo model for describing the softening behaviour of TSSA

		Maximum applied engineering stress				
Material models	Coeff.	0.5 MPa	1 MPa	1.5 MPa	2 MPa	2.5 MPa
Guo	m	34.392	21.361	2.641	0.617	0.442
	r	0.121	0.125	0.00025	1.537	1.503
	m_1	0.079	0.816	1.662	0.365	0.839
	r_1	0.063	0.017	0.640	0.491	0.628
	$R^2_{unloading}$	0.9688	0.9816	0.9924	0.9962	0.9930
	$R^2_{reloading}$	0.7914	0.8896	0.9531	0.9742	0.9675

6.4 Conclusions

In this chapter, multiple phenomenological material models are calibrated and compared to the available experimental data. Uniaxial tension, shear and equibiaxial tension data are used to calculate the material constants of TSSA. The least squares optimization method is used to fit the experimental data to mathematical models based on continuum mechanics theory. The results from the curve fitting process showed that there is not a unique "optimal" set of material parameters and that the identification of those parameters is in general a very delicate issue, a fact which has been also highlighted in the work of Ogden et al. [53], Drass et al. [13, 14], Dispersyn et al. [31] and many more. The suitability of a model depends on the extend to which it can recreate the deformation behaviour and the stiffness of the adhesive in multiple deformation states and varying stress levels. However, it is generally difficult to achieve an almost perfect fitting for all tested deformation states and thus the suitability of a model should also be related to a particular application.

The two parameter models proposed by Mooney-Rivlin and Gent-Thomas proved to perform well for all deformation states. Their relative error appears to be acceptable for the largest part of the deformation field of TSSA. The modeling of the stress-softening phenomenon is also discussed with respect to the weakness of pseudo-elastic models, that are currently supported by finite element codes, to account for a non monotonous stress-strain relation describing the unloading and reloading phase. The mechanical response of TSSA is simplified based on the Ogden-Roxburgh model, whereas the Guo model is selected to approach the actual behaviour of the adhesive. Both models performed well, while showing some weakness in describing the permanent deformations observed during loading cycles.

Finally, it should be noted that the calibration of the material parameters in the undamaged and damaged situation was based on the assumption of incompressibility. Obviously, TSSA is not a perfectly incompressible material, a fact which means that the deformation is always dependent on the actual Poisson ratio (v) of the material. In this case, the problem is simplified and a perfectly incompressible behaviour is assumed (v=0.5). The theoretical simulation of the mechanical response of rubbers requires this simplification; however, one should be aware of the error this might cause.

Chapter 7

TSSA laminated connections on the edge of the glass

In this chapter TSSA laminated point connections on the glass edge are studied. Glass specimens with stainless steel blocks bonded to their edge are fabricated for the purpose of this study. Then they are subjected to shear tests to determine their ultimate strength. Numerical analysis is conducted to study the distribution of stresses in the connection.

7.1 Method

7.1.1 Materials and geometry of specimens

In total, four specimens are manufactured with laminated steel blocks on their edge. The glass plates are made of tempered glass with a size of 300 x 150 mm and thickness 19 mm. The edges of the glass are polished. The stainless steel blocks have a size of 50 x 30 x 15 mm. Two cylindrical recesses with a thread are made in the steel block for the positioning of the LVDT's and for imposing the shear load to the connection. The block is laminated at mid-height of the glass edge and centered over the glass thickness.

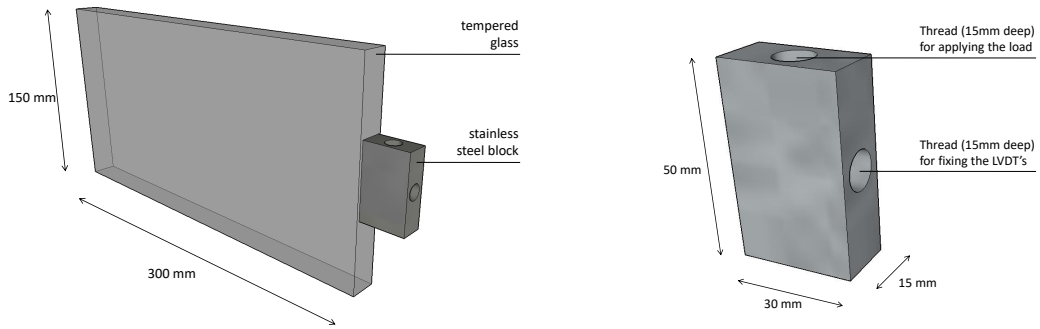
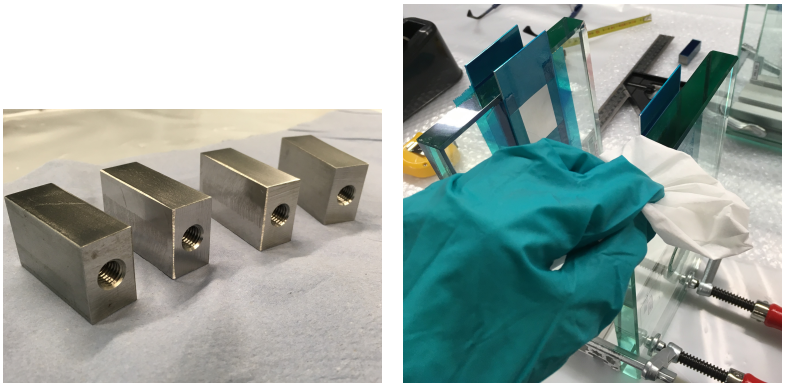


Figure 7.1: Materials and geometry of specimens

7.1.2 Fabrication

The edge bonded connections were fabricated in the TU Delft Aerospace Structures and Materials Laboratory. The stainless steel blocks were sanded prior to lamination. Both the glass and the steel blocks were cleaned following the two-cloth cleaning method recommended by Dow Corning. The surfaces were wiped with soft cloths saturated in isopropanol and then immediately dried with a separate clean cloth. This process was repeated 3 or 4 times to ensure that all dirt and contaminants were sufficiently removed.



(a) Stainless steel blocks

(b) Cleaning the substrates prior to lamination

Figure 7.2: Preparation of the substrates for lamination

Subsequently, the TSSA foil was taken out of the refrigerator and conditioned at room temperature until no condensation was visible on its surface. TSSA comes with two protective thin foils on both sides, a fact which prevents any condensation coming directly in contact with its surface. It is important that the water completely evaporates prior to cutting the foil into the desired size and removing the protective layers, because otherwise water may infiltrate on the surface of the adhesive and cause problems during lamination (e.g. not sufficient bonding due to air bubbles). First, TSSA was applied on the surface of the stainless steel block. The foil was applied very carefully in order to ensure that no air bubbles were created on the interface between the adhesive and the steel surface. Subsequently, the steel block was positioned on the surface of the glass edge. Two aluminum plates were taped on two opposite sides of the glass in order to ensure that the steel block remains completely straight throughout the lamination process. Two thermocouples were connected with the glass and the steel block close to the adhesive. In this way the temperature of the materials is monitored throughout the curing process.

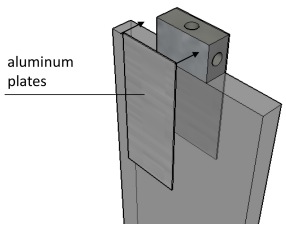
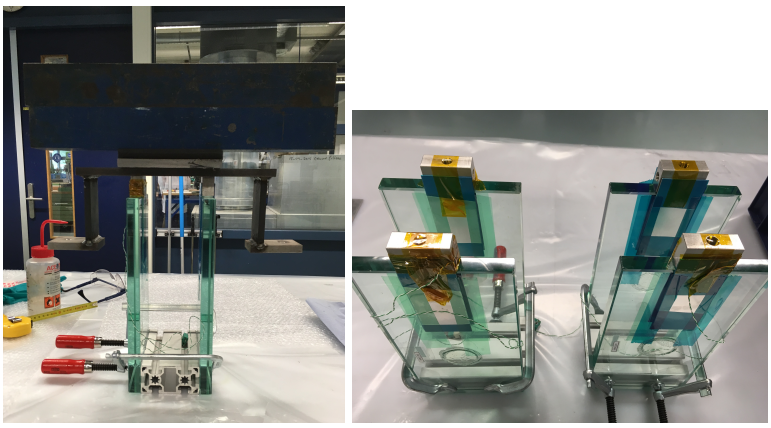


Figure 7.3: Aluminum plates for stability

Pressure is applied to ensure optimum contact of the material interfaces. Dow Corning recommends a pre-pressure of 0.15 to 1.3 MPa. In this case, a pressure of 0.2 MPa was imposed to each connector for 15 minutes. If air bubbles were still visible then the process was repeated to ensure that the adhesive entered the oven with as few as possible air inclusions. The specimens entered the oven that was preheated at 135^{o}C. This temperature remained stable for one hour and a half. Subsequently, the oven was switched off and the specimens were left there to cool down gradually for 18 hours. More detailed information about the end results is provided in Appendix D.



(a) (b)

Figure 7.4: Applying pressure to the connectors (a) and picture of the specimens after curing (b)

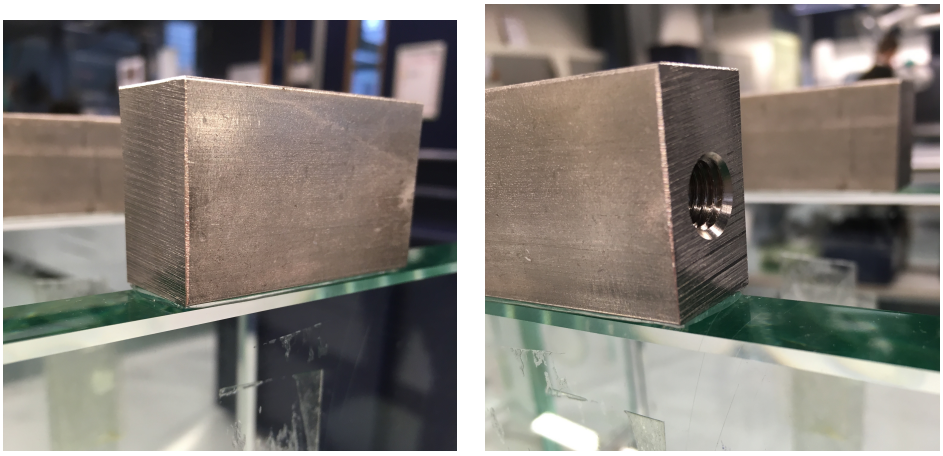


Figure 7.5: Close views to the edge bonded connections after lamination

7.1.3 Test set-up

Tests were performed with a SCHENCK testing machine and a 10KN load cell. A steel set-up is made to restrain the glass plate when the connection is loaded. The glass plate is restrained laterally by two steel plates with a thickness of 15 mm. These plates are stabilized and fixed to the machine base with the help of two L-profiles (80 x 80 x 8 mm). In the vertical direction, the glass is restrained by two M8 bolts that pressure the glass and prevent uplift or rotation of the glass during the test. At the interfaces between glass and steel, small aluminum plates are positioned to avoid direct contact of glass and steel and reduce the possibility of brittle failure of the glass during testing. A simplified sketch of the steel set-up is given in Figure 7.6.

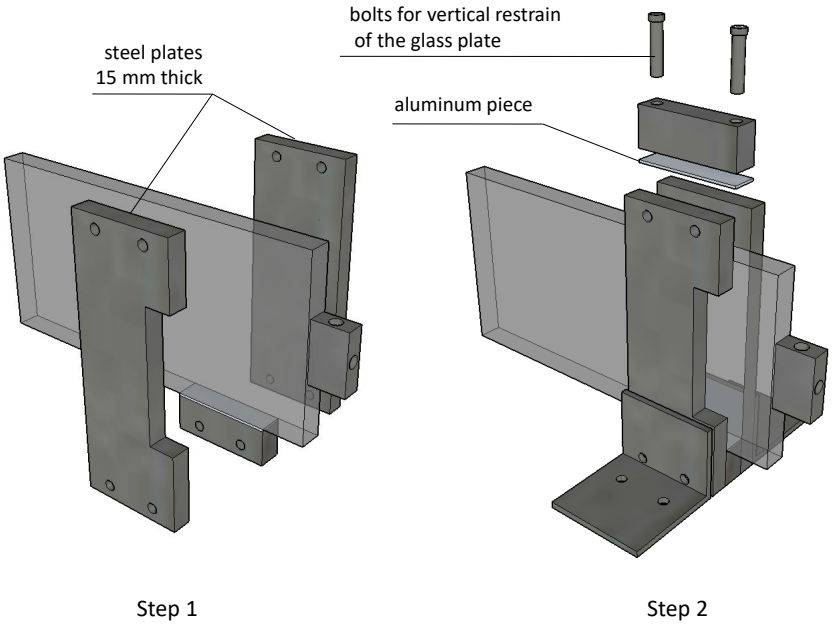


Figure 7.6: Sketch of the steel set-up for clamping the glass

The shear load is transferred to the connector via an M10 steel rod. The rod is connected to a metallic hinge, which in turn is connected to the load cell. The machine base displaces downwards and brings the steel rod in tension introducing a shear load to the connection. The relative displacement between the glass and the steel connector is measured by two LVDT's ± 5 mm, which are placed on the right and left side of the connector. These are fixed onto an extra aluminum piece which in turn is rigidly connected to the stainless steel block. An aluminum L-profile (with thickness 2mm) is glued on the surface of the glass edge in order to measure the relative displacement of glass and steel (see Figure 7.8).

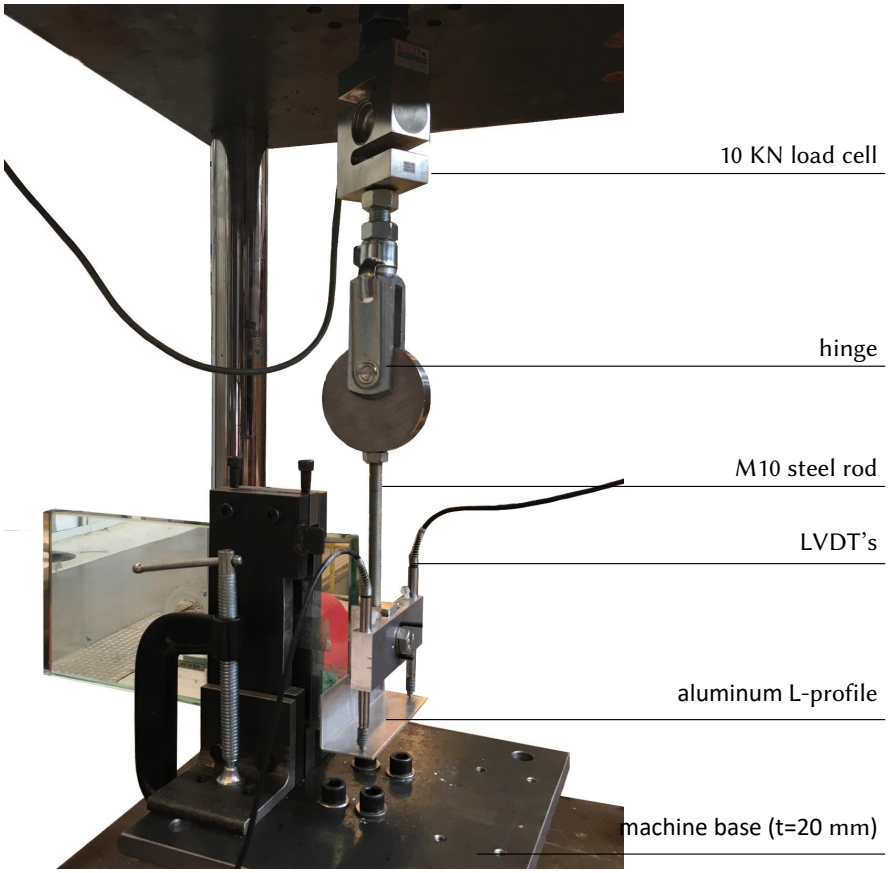


Figure 7.7: Set-up for shear testing the TSSA edge bonded connections

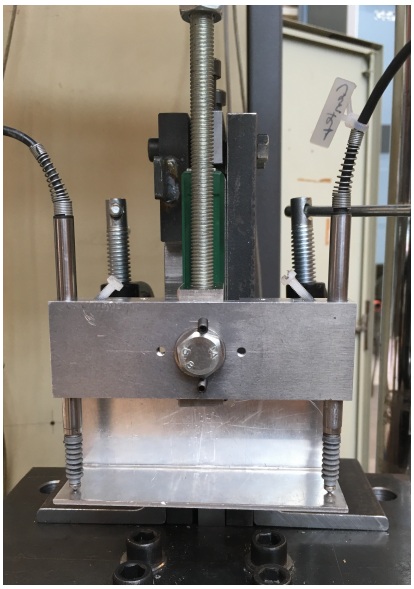


Figure 7.8: Method for measuring the relative displacement of glass and steel

7.2 Experimental analysis

A series of static tests is conducted, were TSSA laminated connections on the glass edge are subjected to monotonically increasing shear loads. The specimens are loaded in displacement control under a displacement rate of 1mm/min. The mechanical response in shear is given in Figure 7.9. The majority of results appear to be consistent, with only one specimen slightly deviating from the rest. The behaviour of the connection shows a linear behaviour until before failure and resembles the results obtained from the shear tests of circular connections. The recorded forces, stresses and displacements at the point of failure are given in Table 7.1. The strength of the joint is considerably smaller, in the range of 20%, compared with the recorded strength of the tested circular connections.

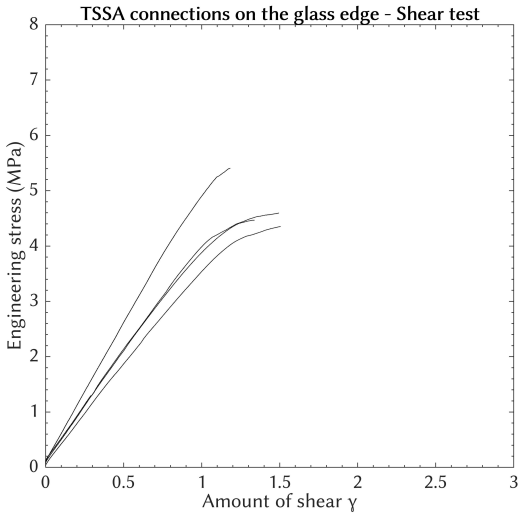


Figure 7.9: Experimental results of TSSA laminated connections on the glass edge under shear force

Table 7.1: Failure results of TSSA connections on the glass edge

Specimen	Force at failure (KN)	Stress at failure (MPa)	Displacement at failure (mm)
EB1	3.45	4.60	1.494
EB2	3.35	4.47	1.339
EB3	4.06	5.41	1.184
EB4	3.26	4.35	1.507
Average	3.53	4.71	1.381
St. dev.	0.36	-	0.15
COV	0.102	-	0.110

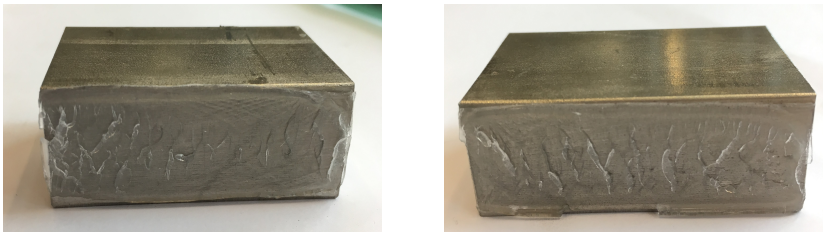


Figure 7.10: TSSA laminated connections on the glass edge after failure

7.3 Numerical analysis

In this section, the shear behaviour of TSSA laminated connections on the glass edge is analyzed by means of a finite element model. The purpose of the numerical analysis is to compute the nonlinear stress distribution in the connection, taking into account its three dimensional nature.

7.3.1 Geometry, boundary conditions and meshing

A three-dimensional finite element model is created with the DIANA FEA software. Figure 7.11 shows the geometry of the model, the dimensions and the boundary conditions. The symmetry along the x-axis is taken into account and thus only half of the connection is modeled in DIANA. Linear material properties are assigned to the glass plate and stainless steel block. The TSSA layer is modeled with the Mooney-Rivlin hyperelastic law, which is the only two-parameter model provided by the software. The Mooney-Rivlin model reproduced almost perfectly the shear behaviour of the adhesive and proved to be adequate for describing the deformations recorded in uniaxial and biaxial tests.

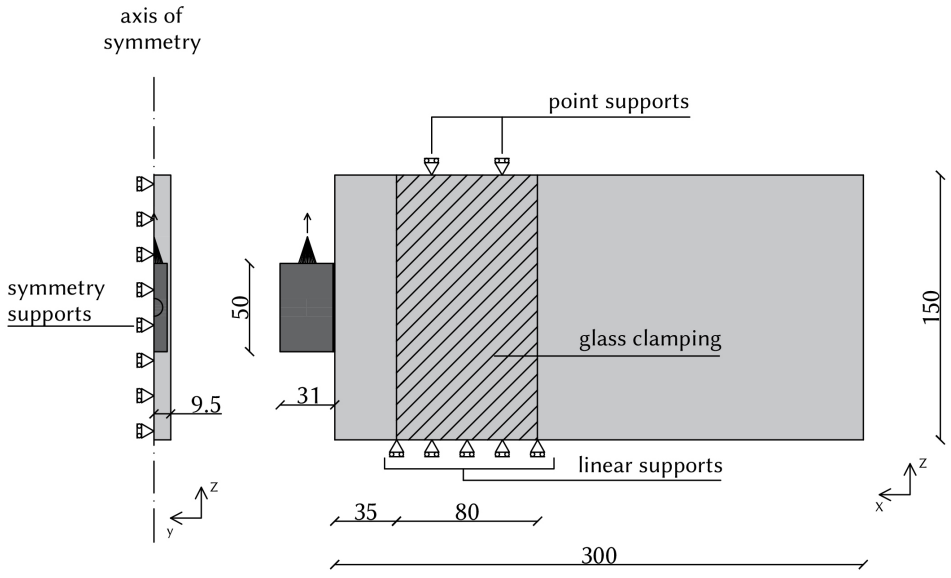


Figure 7.11: Geometry, dimensions and boundary conditions of the model (units in mm)

The Mooney-Rivlin material constants that were calculated in the previous chapter are going to be used for the simulation of TSSA. These constants do not account for any volume changes in the adhesive, since they were calculated based on the incompressibility assumption. Volume changes are considered based on the bulk modulus K, which is usually determined by oedometric tests (see Section 3.4). Alternatively, the initial bulk modulus (K_o) may provide a good approximation. The material properties assigned in the software are given in Table 7.2.

The glass panel is restrained laterally (y-direction) at the position were the steel plates clamp the glass. It is also restrained vertically (z-direction) with a linear support at the bottom and at the top with two point supports at the places were the vertical bolts touch the glass. Symmetry supports in the y-direction are also included in the simulation. The load is applied to a reference point 15 mm above the connection and is redistributed to the stainless steel block via a metallic cone. This is done to simulate the load transfer between the steel rod and the stainless steel thread.

Table 7.2: Material properties

Material	Properties
Glass	$\varrho = 2.50 g/cm^3$ $E = 70000 MPa$ $v = 0.23$
Stainless steel	$\varrho = 7.85 g/cm^3$ $E = 200000 MPa$ $v = 0.3$
TSSA	Mooney-Rivlin: $C_{10} = 1.159 MPa, C_{01} = 0.1554 MPa$ $K_o = 2\frac{(C_{10}+C_{01})}{1-2v} = 26.3 MPa$

The mesh consists of quadratic elements of multiple sizes and geometries. The glass and steel elements are model with regular brick (CHX60[1]), tetrahedron (CTE30[2]), pyramid (CPY39[3]) or wedge (CTP45[4]) structural elements. The adhesive is modeled with brick rubber elements (CHX64[5]) of maximum size 0.5 mm. The mesh of the steel connector is refined close to the adhesive, where the elements have a maximum size of 1mm, and becomes coarser towards the edge of the connector with elements of maximum size 3 mm. The mesh of the glass element is also refined close to the adhesive and consists of elements with maximum size 9.5 mm.

[1] Isoparametric solid brick elements with 20 nodes, based on quadratic interpolation.
[2] Isoparametric solid tetrahedron elements with 10 nodes, based on quadratic interpolation.
[3] Isoparametric solid pyramid elements with 13 nodes, based on quadratic interpolation.
[4] Isoparametric solid wedge elements with 15 nodes, based on quadratic interpolation.
[5] Isoparametric solid (rubber) brick elements with 20 nodes, based on quadratic interpolation.

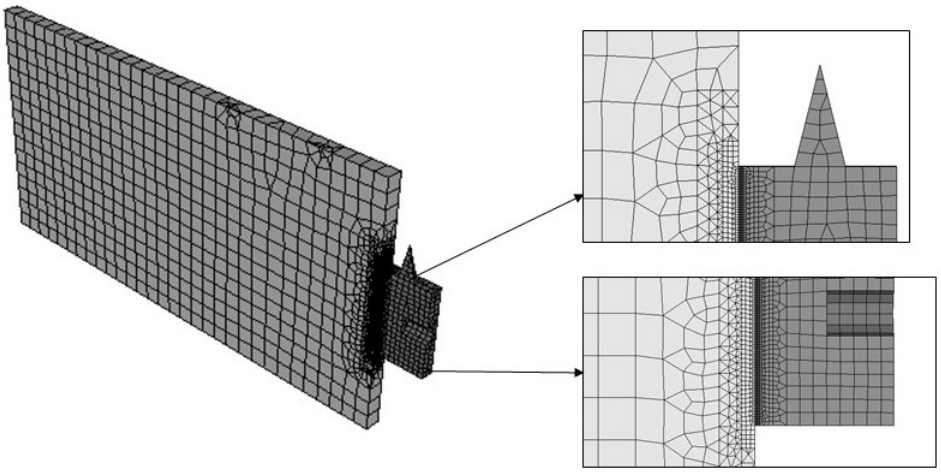


Figure 7.12: Mesh of the three-dimensional model in DIANA FEA

Nonlinear step-by-step analysis is conducted using the regular Newton-Raphson method. Physical and geometric nonlinearities are taken into account, since the deformation of the adhesive must be calculated based on the hyperelastic and finite deformation theories.

7.3.2 Numerical results and discussion

Figure 7.13 shows the distribution of shear stresses in edge bonded connections subjected to shear loads. The stress distribution is not uniform along the x and z axes. The non-uniform distribution of stresses along the x-axis has also been observed in numerical analysis of circular (d=50 mm) connections performed by Santarsiero[1]. This nonlinearity is attributed to the fact that the adhesive has a very small thickness compared to the glass and steel adherents and thus it is unable to fully involve, stress-wise, their whole thickness. Therefore, the stresses in the adherents are localized close the the adhesive. The stresses in the adhesive appear to be uniform towards the middle part of the connection. However, high stress peaks are visible close to the free edge of the connection, especially at the interface of the adhesive with the glass element.

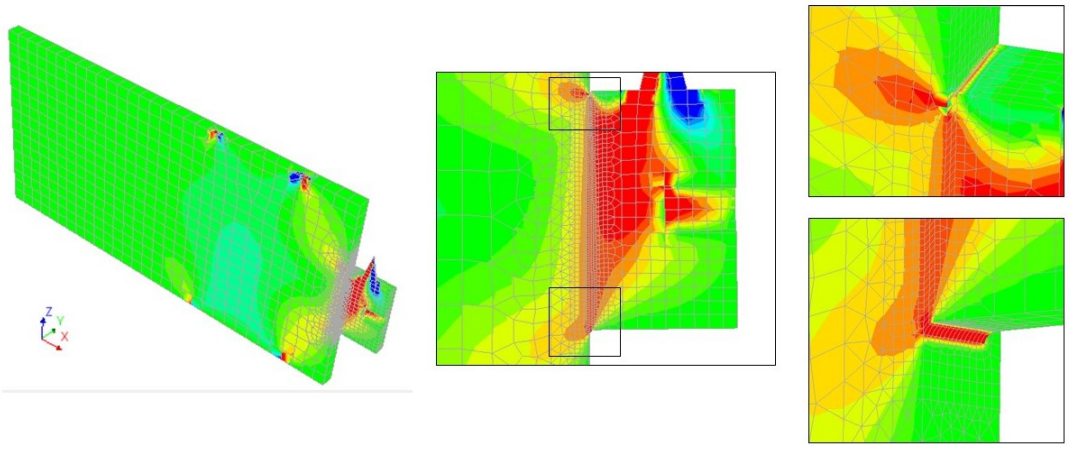


Figure 7.13: Distribution of shear Cauchy stresses (σ_{xz}) in laminated connections on the glass edge

Even though a shear load is applied to the connection, normal tensile and compressive stresses are also occurring. This is because the load is applied with a certain eccentricity from the glass edge and causes bending stresses. Figure 7.14 illustrates the distribution of stresses normal to to the surface of the connection (σ_{xx}).

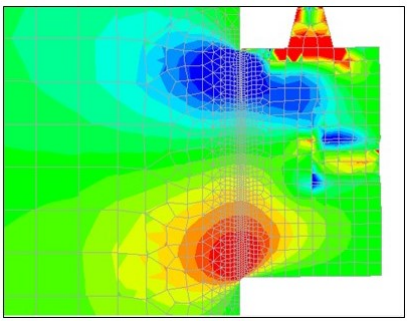


Figure 7.14: Distribution of bending stresses

To give a better understanding, the shear stress distribution along the height of the adhesive is plotted in Figure 7.15. The results are presented in terms of normalized stress versus normalized distance. The normalized stress is the ratio between the actual stress τ_{zy} occurring on the interface of the adhesive with the glass and the nominal stress τ_{nom}. The actual shear stresses are obtained by the three-dimensional finite element analysis and the nominal stress is calculated based on the applied force F divided by the adhesive area A.

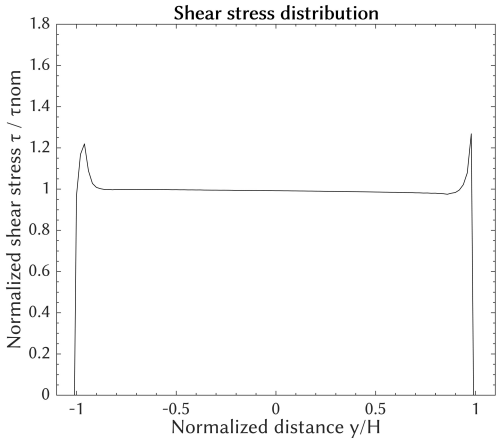


Figure 7.15: Shear stress distribution in the adhesive

The results show significant stress peaks on the edges of the connection. A parametric study is performed varying the eccentricity of the applied load. More specifically, the results obtained from applying the load in the middle of the connection are compared with the cases of maximum and minimum possible eccentricity. The goal is to understand how much the eccentricity of the applied load affects the stress peaks in the adhesive.

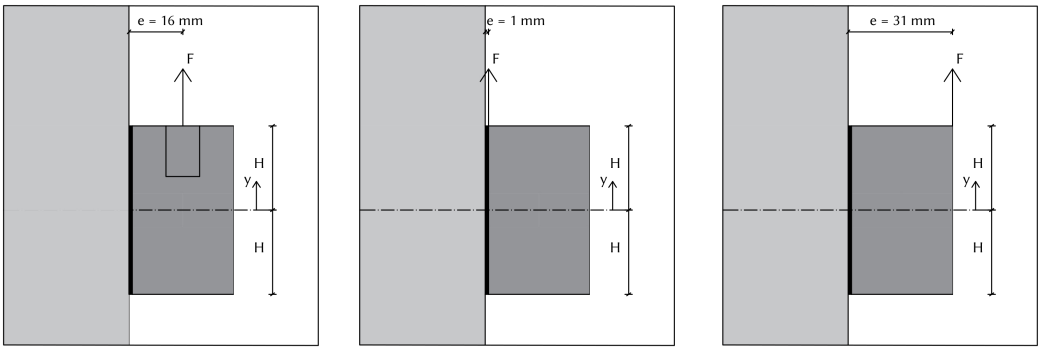


Figure 7.16: Examined eccentricities

The results of the parametric study are illustrated in Figure 7.17. For the case where the load is applied very close to the connection, stress peaks appear to be much less severe than what was observed in the tested configuration. In case the load is applied on the edge of the connector (maximum eccentricity of 31 mm), the stress peaks become very critical. The results verify that there is some dependency on the magnitude of stress peaks and the eccentricity of the applied load.

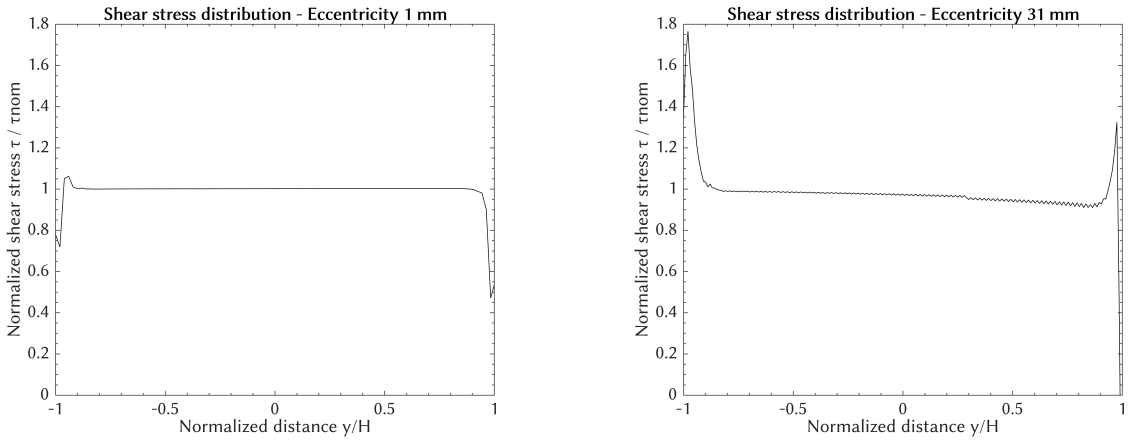


Figure 7.17: Shear stress distribution in the adhesive at varying load eccentricities

7.4 Discussion and conclusions

The numerical analysis of laminated connections on the glass edge showed that the efficiency of the joint depends on the eccentricity of the applied load. This is because stress peaks occur close to the end of the joint and become more severe as the eccentricity of the load increases. In case of high stress peaks, the shear load is mainly transferred with shear stresses concentrated on the edge of the connection [1] and thus the largest portion of the connecting surface does not contribute significantly to the shear load transfer.

This might explain the reason the edge bonded specimens failed at considerably lower engineering stresses than the ones recorded for circular connections. After the fabrication of the edge bonded specimens, weaknesses were observed at the edges of the adhesive (see also Appendix D.1), a fact

which might have contributed to their early failure. Therefore, it is recommended that particular attention must be payed to the quality of lamination on the edges. Further improvements to increase the strength of the connection include the application of a primer and a heat-curing process inside an autoclave, as recommended by the manufacturer.

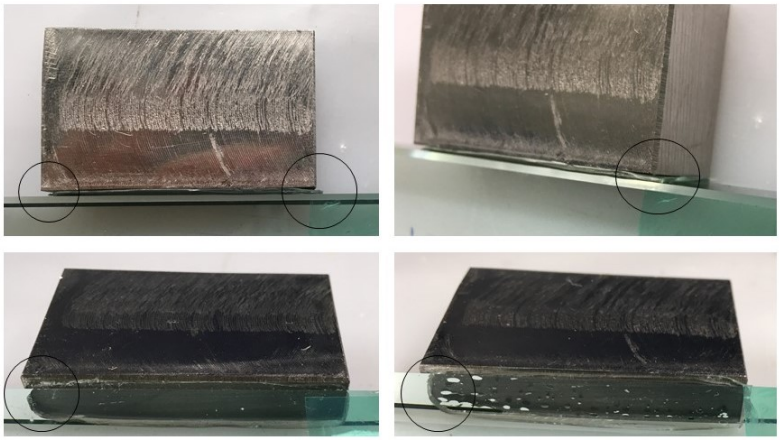


Figure 7.18: Pictures after fabrication - weak edges

Edge bonded connections could be used in many ways and configurations in building construction and they would allow simpler connection joints and easier assembly of glass elements. More specifically, applications such as supporting vertically glass panels onto glass fins may be considered. Stainless steel blocks may be laminated on the edge of glass panels and fins in order to enable the realization of simple vertical connections loaded in shear (see Figure 7.19). In this case, vertical bolts may be used to prevent lateral movement.

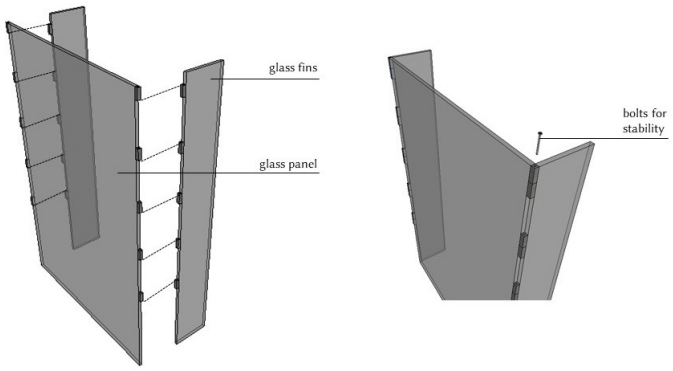


Figure 7.19: Glass panel supported vertically on glass fins

A more ambitious approach is the realization of a vertical connection at the edge of a simply supported glass beam. However, creep and relaxation effects of TSSA must be thoroughly investigated prior to the development of such connection. Furthermore, ensuring that a shear load is the dominant action in the connection may prove to be more challenging. Stabilizing the connection with simple a configuration could induce a risk of adhesive detachment. Inserting a hinge into the system may mitigate such a risk, and thus could enable the creation of a pure shear connection (see Figure 7.20(c)).

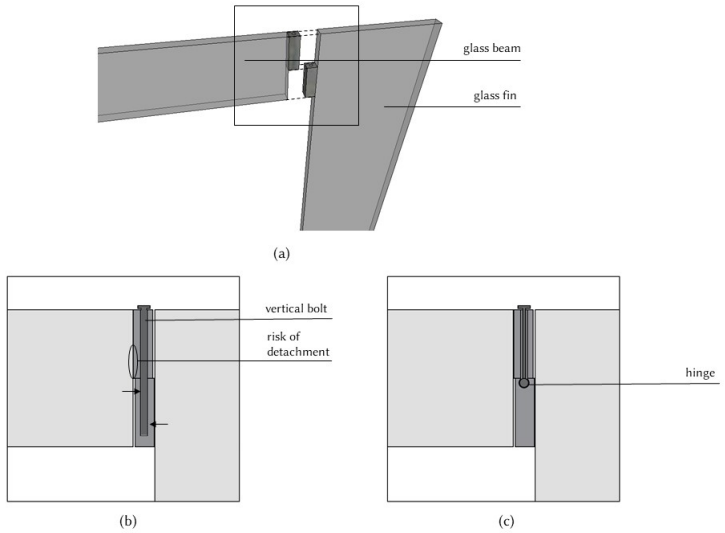


Figure 7.20: Connection of a simply supported beam

There is still plenty of room for research and development of such systems that goes beyond the scope of this study. Nevertheless, this case study provides a first glance on the feasibility and the behaviour of such connections and aims to give the trigger for future research involving different sizes, geometries and configurations of edge bonded connections.

Chapter 8

Conclusions and recommendations

8.1 Conclusions

In this master thesis, the mechanical behaviour of TSSA laminated connections was studied. The research focused on investigating the static and cyclic mechanical response of TSSA laminated circular connections under shear and tensile load. The tests were combined with uniaxial and biaxial test data in order to calibrate various hyperelastic models for the simulation of the mechanical response of TSSA. The stress-softening phenomenon observed in cyclic tests was analyzed and a simplification of the softening response was suggested. Subsequently, the softening behaviour was simulated based on the simplified approach that is currently supported by finite element codes. A first attempt was also made to simulate the actual softening behaviour of the adhesive based on a more sophisticated model. From the experimental and analytical results, the following conclusions can be drawn.

In Chapter 4, the mechanical response of TSSA laminated circular connections with diameter 50 mm is studied by means of simple shear tests. It is concluded that the cyclic response of TSSA shows significant stress softening that depends on the maximum load previously encountered and the applied frequency. This softening behaviour deviates from the static response, which appeared to be mainly linear, and thus a nonlinear constitutive law is needed to simulate the cyclic response of TSSA. More specifically, the observations and conclusions are the following. The softening phenomenon is observed even at cycles performed at low stress levels and becomes more severe as the maximum load increases. Energy dissipation analysis showed that the mechanical response of TSSA tends to stabilize after a certain number of cycles. Whitening appears at high stress levels but it was much less evident compared with the case of tensile tests. Under cyclic loading, whitening is barely visible. Furthermore, loading cycles were either performed in one or two directions (reverse shearing) and at different frequencies of 0.1 or 1 Hz. The mechanical response of the connections subjected to reverse shearing appears to be the same in both directions, meaning that there is no need to account for any divergence of the response between "positive" and "negative" shear when it comes to the simulation of the deformation behaviour. Moreover, results from shearing in only one direction appeared to be more conservative and resulted in higher deformations compared with reverse shearing tests. However, all specimens subjected to reverse shear loads failed before the completion of the cyclic loading schedule.

In Chapter 5, the behaviour of laminated circular connections under tensile load is studied. It is concluded that the stress-softening phenomenon starts to develop at very high stress levels above the working limit of the connection. Furthermore, the development of the whitening phenomenon was observed to be similar under static and cyclic loading. More specifically, the results showed that the

mechanical response of the connection under static tensile load is bilinear, exhibiting a very stiff behaviour followed by a significant reduction of the stiffness until failure. Whitening starts to propagate from the middle and finally covers the perimeter of the connection. Under cyclic loading, whitening completely disappears when the load is removed leaving no trace. This information must be carefully considered in case the whitening effect is utilized as a warning for overloading. In civil engineering practice, stress peaks usually appear instantaneously, a fact which means that in case of overloading, the whitening effect is expected occur instantly and thus to disappear completely when the connection is unloaded. Nevertheless, the whitening effect shows some consistency to a certain stress state, a fact which is considered advantageous as it may be used as an indicator of the quality of bonding in non-destructive quality assurance testing.

In Chapter 6, various phenomenological models are calibrated and assessed based on their performance to recreate the mechanical behaviour of the adhesive. From the results it can be concluded that the Mooney-Rivlin and the Gent-Thomas models perform best in describing the static behaviour of TSSA in the considered deformation states and that the Guo model can provide a good approximation of the actual cyclic response of the adhesive. More specifically, the shear tests performed within the framework of this study are combined with uniaxial and biaxial tension test data performed by Santarsiero [1] and Drass et al. [13, 14], respectively. The theoretical simulation of the mechanical response of TSSA involves many simplifications and the selection of the optimal model is not a straight forward process. The suitability of a model depends on its ability to recreate the behaviour of the adhesive in multiple deformations states. However, this is often difficult to be achieved and thus the suitability should also be related to a particular application. The softening behaviour observed in shear tests was modeled based on the simplified approach proposed by Ogden and Roxburgh. A less conservative approach was suggested based on the model of Guo, that accounts for a divergence between the unloading and the reloading paths and appeared to approach better the actual response of the adhesive. This model may be implemented in a user-defined subroutine and be used to predict the changes in stiffness observed during the tests.

In Chapter 7, the first attempt to laminate a stainless steel connector on the glass edge is studied by means of experimental tests and numerical analysis. It can be concluded that most of the shear force is carried by the edges of the adhesive layer and that the efficiency of the connection depends on the eccentricity of the applied load. More specifically, the experimental tests showed that the mechanical response of the connection appears to be mainly linear, resembling the experimental results of circular connections. However, the specimens failed at considerably lower engineering stress levels. Numerical analysis showed that the shear force is mainly carried by the edges of the adhesive, as high stress peaks appeared close to the free edges of the connection. A parametric study varying the eccentricity of the load showed that the peaks become more severe as the eccentricity is increased and thus the efficiency of the connection is reduced.

8.2 Recommendations for future research

From the research performed in this master thesis, several possibilities arise for future research.

In Chapter 4, shear cyclic tests are conducted to analyze the stress-softening phenomenon. Tests are performed on circular connections of diameter 50 mm. It would be of interest to repeat the same tests on circular connections of varying diameters or to experiment with different geometries. This will give a better understanding on the dependency of the results on geometry. Points of interest are finding a threshold for the start of the stress-softening phenomenon, studying the hysteretic response and calculating the dissipated energy to understand whether the mechanical response of the adhesive has a tendency to stabilize after a certain number of cycles. It is also recommended that the same experimental study is repeated at different deformation states, such as uniaxial and biaxial tension, and the results are compared with those obtained from the shear tests.

Furthermore, an experimental study could be launched to investigate the change in behaviour under different frequencies. The results of this study showed that the mechanical response of the adhesive under loading cycles is dependent on the applied frequency. Therefore, it would be interesting to perform cyclic tests at varying frequencies, in order to find a threshold when the response starts to change.

The shear and tensile cyclic tests showed that there is a viscoelastic effect present in TSSA. A viscoelastic material exhibits a hysteretic behaviour under loading cycles, as well as it creeps or relaxes under long-term loading. It would be of interest to study the long-term behaviour of TSSA by means of sustained loading tests at varying load levels. The experimental results may be used to calibrate time-dependent nonlinear elastic models in order to consider viscoelastic effects in numerical simulations.

In Chapters 4 and 5, the possibility of recovering the behaviour of the adhesive accounting for time and temperature effects is investigated. Results showed that the damage caused by the Mullins effect is permanent. Therefore, future research should focus on the fatigue resistance of TSSA connections and its possible relation with the stress-softening phenomenon. An experimental campaign should be introduced where connections are subjected to loading cycles until failure. The tests should be repeated at different load levels with the aim to derive a stress-number of cycles curve. Additional experimental research on fatigue may also include temperature effects.

In Chapter 6, the mechanical response of TSSA under static and cyclic loading was simulated based on hyperelastic constitutive laws and damage models. In order to provide additional validation, the material models should be implemented in a finite element software where the complete geometry of the test set-up is simulated. Subsequently the numerical results should be compared with the experimental data. Furthermore, volumetric changes in the material should be studied by means of oedometric tests, in order to experimentally derive the bulk modulus of TSSA.

In Chapter 7, the shear behaviour of TSSA laminated connections on the glass edge is studied. For future attempts to fabricate edge bonded connections, it is recommended that pre-pressure is increased in order to eliminate air bubbles and that the specimens are cured inside an autoclave. Special attention should be payed to the quality of the free edges of the adhesive. It would be interesting to repeat the tests on rectangular connections of different sizes and numerically calculate the stress peaks in the adhesive. Experimental research could also be extended to study the behaviour and strength of a stainless steel connector laminated on the edge of a multi-layered laminated glass component. In this case, topics such as chemical compatibility of TSSA and PVB or the reduction of the effective connecting surface, due to the interaction with the interlayers, could be addressed.

Bibliography

[1] M. Santarsiero. *Laminated Connections for Structural Glass Applications*. PhD thesis, EPFL, Lausanne, 2015.

[2] IStructE. *Structural use of glass in buildings*. Institution of Structural Engineers, December 1999.

[3] V. Dias. *Development of adhesives constitutive material laws for the assessment of bonded steel to glass partial composite beams*. PhD thesis, University of Luxembourg, November 2013.

[4] D. Callewaert. *Stiffness of Glass/Ionomer Laminates in Structural Applications*. PhD thesis, Ghent University, 2011.

[5] NEN 2608: Vlakglas voor gebouwen - Eisen en bepalingsmethode, 2014.

[6] M. Lindqvi. *Structural Glass Strength Prediction Based on Edge Flaw Characterization*. PhD thesis, EPFL, February 2013.

[7] S. Sitte, M.J. Brasseur, L.D. Carbary, and A.T. Wolf. Preliminary Evaluation of the Mechanical Properties and Durability of Transparent Structural Silicone Adhesive (TSSA) for Point Fixing in Glazing. *Journal of ASTM International*, Vol. 8(No. 10):pp. 1–27, 2011.

[8] M. Santarsiero, C. Louter, and A. Nussbaumer. The mechanical behaviour of SentryGlas ionomer and TSSA silicon bulk materials at different temperatures and strain rates under uniaxial tensile stress state. *Glass Structures and Engineering*, pages 1–21, 5 2016.

[9] A. Hagl, O. Dieterich, A. T. Wolf, and S. Sitte. Tensile Loading of Silicone Point Supports - Revisited. In *Challenging Glass 3*, 2012.

[10] L. Mullins. Softening of Rubber by Deformation. *Rubber Chemistry and Technology*, 42(1):339–362, 1969.

[11] L. Mullins. Effect of Stretching on the Properties of Rubber. *Rubber Chemistry and Technology*, 21(2):281–300, 1948.

[12] L. Mullins. Permanent Set in Vulcanized Rubber. *Rubber Chemistry and Technology*, 22(4):1036–1044, 1949.

[13] M. Drass, G. Schwind, J. Schneider, and S. Kolling. Adhesive Connections in Glass Structures - Part I: Experiments and Analytics on Thin Structural Silicone. *Glass Structures & Engineering*, 2017.

[14] M. Drass, G. Schwind, J. Schneider, and S. Kolling. Adhesive Connections in Glass Structures - Part II: Material Parameter Identification on Thin Structural Silicone. *Glass Structures & Engineering*, 2017.

[15] *Dow Corning Transparent Structural Silicone Adhesive (TSSA) Product - Product Application and Handling, Quality Control Guide, Facade Design Guide*, January 2014.

[16] J. Watson. *Novel Structural Glass Connections for Architectural Applications*. PhD thesis, University of Cambridge, 2013.

[17] M. Santarsiero, C. Louter, and A. Nussbaumer. Laminated connections for structural glass applications under shear loading at different temperatures and strain rates. *Construction and Building Materials*, 128:214 – 237, 2016.

[18] M. Santarsiero, C. Louter, and A. Nussbaumer. Laminated connections under tensile load at different temperatures and strain rates. *International Journal of Adhesion and Adhesives*, pages –, 2017.

[19] ASTM Standard C1184-05. Standard Specification for Structural Silicone Sealants. Annual Book of ASTM Standards, 2005.

[20] EOTA Recommendation. ETAG 002 Structural Sealant Glazing Systems, Part 1: Supported and Unsupported Systems, 1999; Part 2: Coated Aluminium Systems, 2002; Part 3: Thermal Breaks, 2003.

[21] EN Standard 15434:2006 + A1. Glass in Building - Product Standard for Structural and/or Ultraviolet Resistant Sealant (for Use With Structural Sealant Glazing and/or Insulating Glass Units With Exposed Seals), 2010.

[22] A. Ali, M. Hosseini, and B. B. Sahari. A Review of Constitutive Models for Rubber-Like Materials. *American Journal of Engineering and Applied Sciences*, 3(1):232–239, 2010.

[23] G. Chagnon, G. Marckmann, and E. Verron. A Comparison of the Hart-Smith Model with Arruda-Boyce and Gent Formulations for Rubber Elasticity. *Rubber Chemistry and Technology*, 77(4):724–735, 2004.

[24] J. Diani, B. Fayolle, and P. Gilormini. A review on the Mullins effect. *European Polymer Journal*, 45(3):601 – 612, 2009.

[25] J. A. C. Harwood, L. Mullins, and A. R. Payne. Stress Softening in Natural Rubber Vulcanizates. Part II. Stress Softening Effects in Pure Gum and Filler Loaded Rubbers. *Rubber Chemistry and Technology*, 39(4):814–822, 1966.

[26] AF. Blanchard and D. Parkinson. Breakage of carbon-rubber networks by applied stress. *Ind Eng Chem*, 44:799–812, 1952.

[27] R. Houwink. Slipping of molecules during the deformation of reinforced rubber. *Rubber Chem Technol*, 29:888–93, 1956.

[28] EM Dannenberg and JJ. Brennan. Strain-energy as a criterion for stress softening in carbon-black-filled vulcanizates. *Rubber Chem Technol*, 39:597–608, 1965.

[29] G. Kraus, CW Childers, and KW Rollman. Stress softening in carbon black reinforced vulcanizates. Strain rate and temperature effects. *J Appl Polym Sci*, 10:229–240, 1966.

[30] G. Marckmann and E. Verron. Comparison of Hyperelastic Models for Rubber-Like Materials. *Rubber Chemistry and Technology*, 79(5):835–858, 2006.

[31] J. Dispersyn, S. Hertele, W. De Waele, and J. Belis. Assessment of hyperelastic material models for the application of adhesive point-fixings between glass and metal. *International Journal of Adhesion and Adhesives*, 77:102 – 117, 2017.

[32] Z. Guo. *Computational Modelling of Rubber-like Materials under Monotonic and Cyclic Loading*. PhD thesis, Delft University of Technology, 2006.

[33] R.S. Rivlin. Large Elastic Deformations of Isotropic Materials. IV. Further Developments of the General Theory. *Philosophical Transactions of the Royal Society of London A: Mathematical, Physical and Engineering Sciences*, 241(835):379–397, 1948.

[34] V. Dias, C. Odenbreit, O. Hechler, F. Scholzen, and T. Ben Zineb. Development of a constitutive hyperelastic material law for numerical simulations of adhesive steelâglass connections using structural silicone. *International Journal of Adhesion and Adhesives*, 48:194 – 209, 2014.

[35] M. Mooney. A Theory of Large Elastic Deformation. *Journal of Applied Physics*, 11(9):582–592, 1940.

[36] MSC.Software. *Nonlinear Finite Element Analysis of Elastomers*, 2010.

[37] R. S. Marlow. A general first-invariant hyperelastic constitutive model. In *Constitutive Models For Rubber -Proceedings*, pages 157–160, London, 2003. Balkema.

[38] P. Steinmann, M. Hossain, and G. Possart. Hyperelastic models for rubber-like materials: consistent tangent operators and suitability for Treloar's data. *Archive of Applied Mechanics*, 82(9):1183–1217, 2012.

[39] O.H. Yeoh. Phenomenological Theory of Rubber Elasticity. In SL Aggarwal, editor, *Comprehensive Polymer Science*. Pergamon Press, 1995.

[40] F. Peeters and M. Kussner. Material law selection in the finite element simulation of rubber-like materials and its practical application in the industrial design process. *Const Model Rubber*, pages 29–36, 1999.

[41] A.N. Gent and A.G. Thomas. Forms for the stored (strain) energy function for vulcanized rubber. *Journal of Polymer Science*, 28(118):625–628, 1958.

[42] J.C. Simo. On a fully three-dimensional finite-strain viscoelastic damage model: Formulation and computational aspects. *Computer Methods in Applied Mechanics and Engineering*, 60(2):153 – 173, 1987.

[43] S. Govindjee and J. Simo. A micro-mechanically based continuum damage model for carbon black-filled rubbers incorporating Mullins' effect. 39:87–112, 12 1991.

[44] R.W. Ogden and D.G. Roxburgh. A pseudo-elastic model for the Mullins effect in filled rubber. 455, 08 1999.

[45] H.J. Qi and M.C. Boyce. Constitutive model for stretch-induced softening of the stress-stretch behavior of elastomeric materials. *Journal of the Mechanics and Physics of Solids*, 52(10):2187 – 2205, 2004.

[46] K. Miller. Testing Elastomers for Finite Element Analysis.

[47] W. V. Mars. Evaluation of a Pseudo-Elastic Model for the Mullins Effect. *Tire Science and Technology*, 32(3):120–145, 2004.

[48] R. Kazakeviciute-Makovska. Experimentally determined properties of softening functions in pseudo-elastic models of the Mullins effect. *International Journal of Solids and Structures*, 44(11):4145 – 4157, 2007.

[49] C. Miehe. Discontinuous and continuous damage evolution in Ogden-type large-strain elastic materials. *European Journal of Mechanics A/Solids*, 14:697â720, 1995.

[50] D. Besdo and J. Ihlemann. A phenomenological constitutive model for rubberlike materials and its numerical applications. *Int J Plast*, 19:1019â1036, 2003.

[51] L.R.G. Treloar. *The Physics of Rubber Elasticity*. Monographs on the physics and chemistry of materials. Oxford University Press, USA, 1975.

[52] J. Dispersyn, M. Santarsiero, J. Belis, and C. Louter. A preliminary study of the nonlinearity of adhesive point-fixings in structural glass facades. *Journal of Facade Design and Engineering*, 2:85–107, 2014.

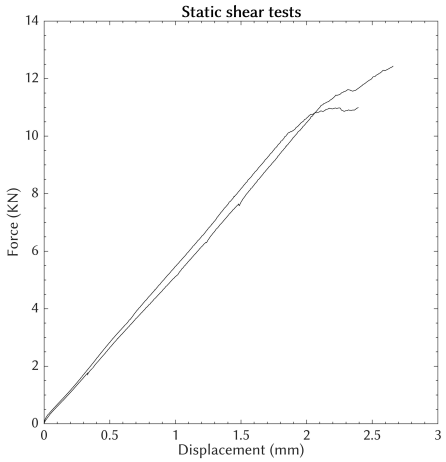
[53] R.W. Ogden, G. Saccomandi, and I. Sgura. Fitting hyperelastic models to experimental data. *Computational Mechanics*, 34(6):484–502, 2004.

[54] JY Sheng, LY Zhang, B Li, GF Wang, and XQ Feng. Bulge test method for measuring the hyperelastic parameters of soft membranes. *Acta Mechanica*, Aug 2017.

Appendix A

Appendix: Shear tests

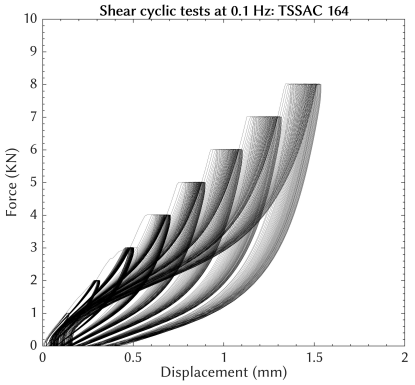
Appendix A.1 - Static shear test results

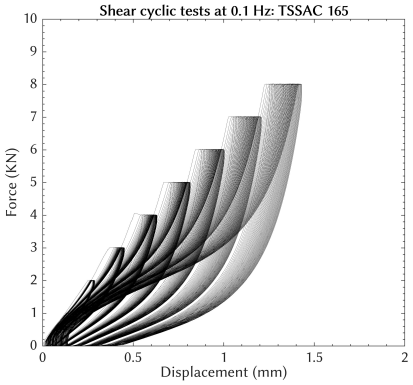


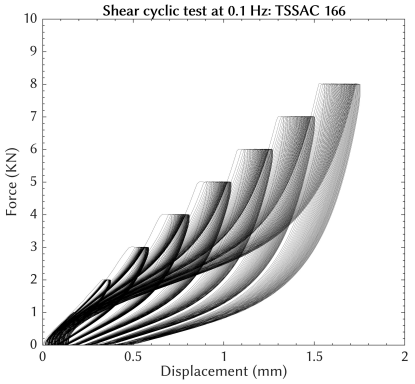
Static shear tests (1mm/min)

Specimen name	Notes before testing	Notes during testing (from video)	Failure load (KN)	Displacement at failure (mm)	Notes after testing
TSSAC 190	a lot of TSSA is squeezed out	1) The bottom half of the connection exhibits very slightly whitening 2) The whitening slightly spreads until the point when the detaching of the button starts close to LVDT 1 3) Fracture happens first on the right part of the connection 4) At failure part of the connection remains white	10.99	2.395	1) After the specimen is removed from the set-up, the whitening disappears 2) The button is not completely detached from the glass 3) Failure happened cohesively within the adhesive
TSSAC 191	little TSSA is squeezed out	1) The bottom half of the connection exhibits very slightly whitening 2) The whitening spreads until the point when the button starts to detach from the glass (close to LVDT 2) 3) Fracture happens first on the left part of the connection 4) at failure a very small part o f the connection remains white	12.44	2.660	1) After the specimen is removed from the set-up, the whitening remains 2) The button is not completely detached from the glass 3) Failure happened cohesively within the adhesive
TSSAC 181	little TSSA is squeezed out	1) The bottom half of the connection exhibits very slightly whitening	14.95	2.452	1) The button is completely detached from the glass 2) Failure happened cohesively within the adhesive

Appendix A.2 - Cyclic shear test results from 0 to +P at 0.1 Hz







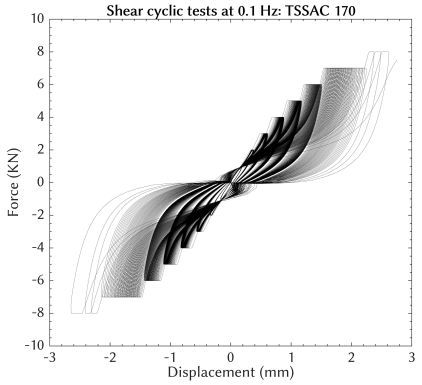
Shear cyclic loading from 0 to +P at 0.1 Hz

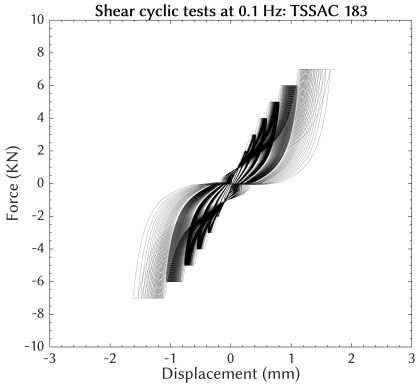
Specimen name	Notes before testing	Notes during testing (from video)
TSSAC 164	a lot of TSSA is squeezed out	Very slight whitening is visible under shear load and is completely recovered after removing the load
TSSAC 165	a lot of TSSA is squeezed out	Very slight whitening is visible under shear load and is completely recovered after removing the load
TSSAC 166	little TSSA is squeezed out	Very slight whitening is visible under shear load and is completely recovered after removing the load

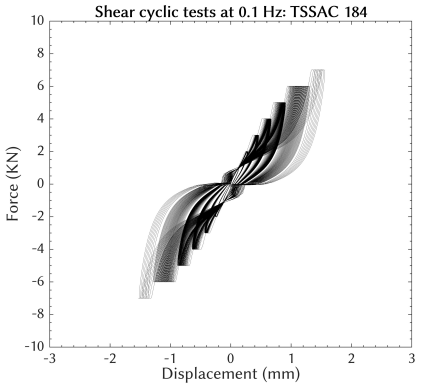
Shear static test after cyclic loading (displ. rate at 1mm/min)

Specimen name	Notes during testing (from camera)	Failure load (KN)	Displacement (mm)	Notes after testing
TSSAC 164	Whitening starts to become clearly visible above 10.7 KN	11.62	2.072	1) The steel button is not completely detached from the glass 2) Failure happened cohesively within the adhesive
TSSAC 165	Whitening starts to become clearly visible above 9.5 KN	12.91	1.976	1) The steel button is not completely detached from the glass 2) Some whitening is still visible after the specimen is removed 2) Failure happened cohesively within the adhesive
TSSAC 166	Whitening starts to become clearly visible above 8.5 KN	11.98	2.268	1) The steel button is not completely detached from the glass 2) Failure happened cohesively within the adhesive

Appendix A.3 - Cyclic shear test results from -P to +P at 0.1 Hz



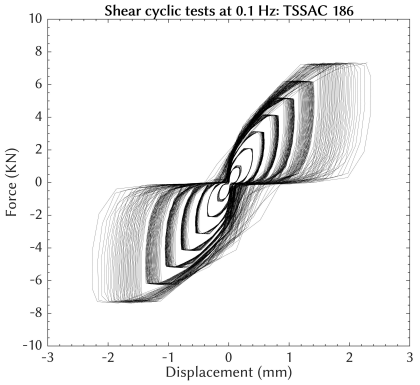


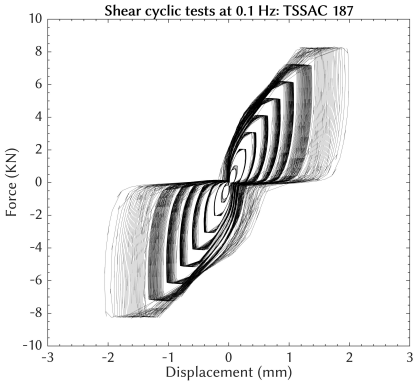


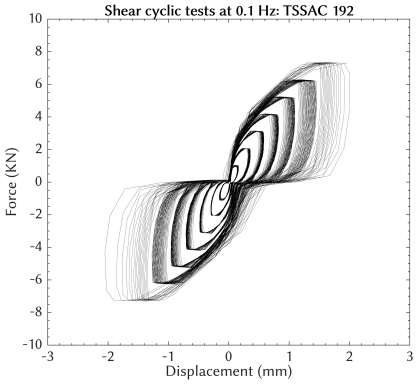
Shear cyclic loading from -P to +P at 0.1 Hz

Specimen name	Notes before testing	Notes during testing (from video)	Failure load (KN)	Notes after testing
TSSAC 170	little TSSA is squeezed out	-	Failure at 7.50 KN during the 354^{th} cycle (at loading cycles from -8 to 8KN)	1) The steel button is completely detached from the glass 2) Failure happened cohesively within the adhesive
TSSAC 183	a lot of TSSA is squeezed out	-	failure at 6.97 KN during the 321^{st} cycle (at loading cycles from -7 to 7KN)	1) The steel button is completely detached from the glass 2) Failure happened cohesively within the adhesive
TSSAC 184	a lot of TSSA is squeezed out	1) Fracture begins on the perimeter of the connection 2) Very slight whitening is visible	Failure at -6.99 KN during the 309^{th} cycle (at loading cycles from -7 to 7KN)	1) The steel button is completely detached from the glass 2) Failure happened cohesively within the adhesive

Appendix A.4 - Cyclic shear test results from -P to +P at 1 Hz







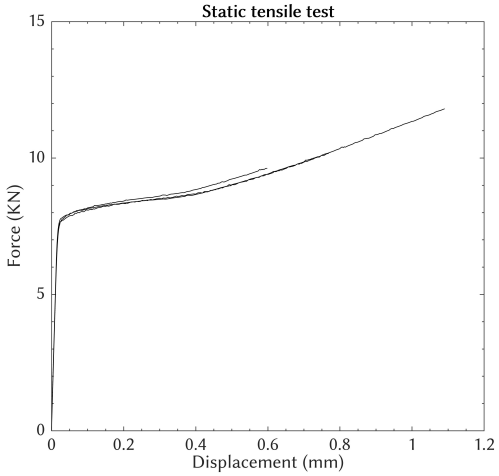
Shear cyclic loading from -P to +P at 1 Hz

Specimen name	Notes before testing	Notes during testing (from video)	Failure load (KN)	Notes after testing
TSSAC 186	little TSSA is squeezed out	1) Very slight whitening appears 2) The whitening pattern changes when reverse shear is applied	Failure at 7.33 KN during the 364^{th} cycle (at loading cycles from -7 to 7KN)	1) The steel button is completely detached from the glass 2) Failure happened cohesively within the adhesive
TSSAC 187	a lot of TSSA is squeezed out	1) Very slight whitening appears uniformly distributed 2) Fracture begins on the perimeter of the connection	failure at 8.28 KN during the 379^{th} cycle (at loading cycles from -7 to 7KN)	1) The steel button is completely detached from the glass 2) Failure happened cohesively within the adhesive
TSSAC 192	a lot of TSSA is squeezed out	1) Fracture begins in the middle of the connection 2) Very slight whitening is visible	Failure at 7.31 KN during the 320^{th} cycle (at loading cycles from -7 to 7KN)	1) The steel button is completely detached from the glass 2) Failure happened cohesively within the adhesive

Appendix B

Appendix: Tensile tests

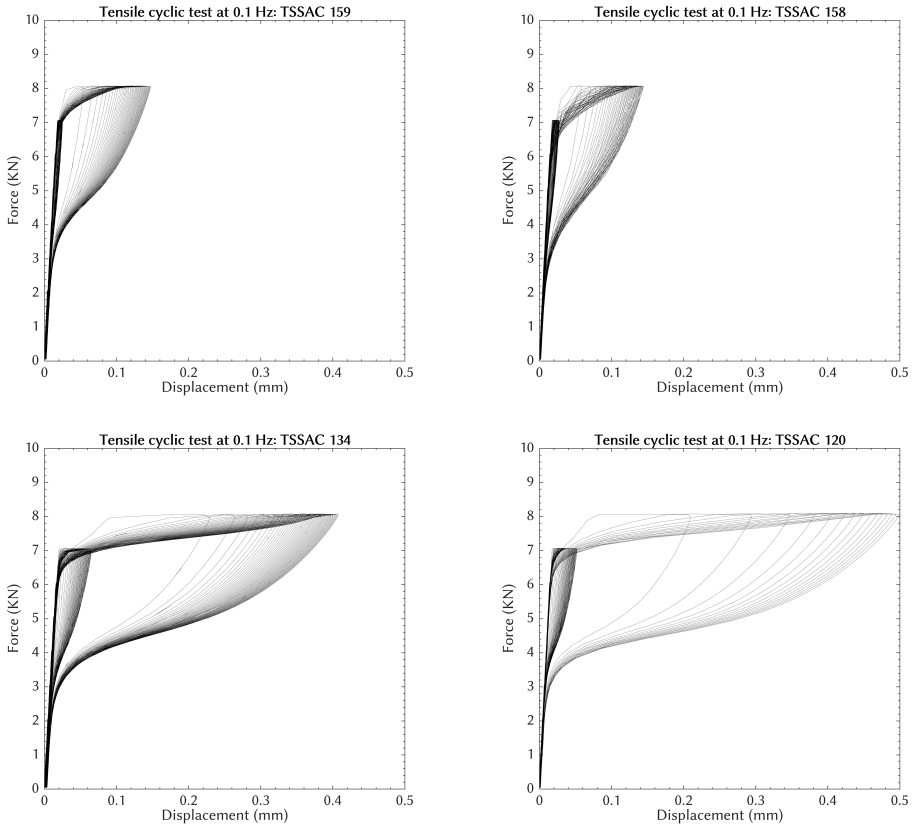
Appendix B.1 - Static tensile test results



Static tensile tests (1mm/min)

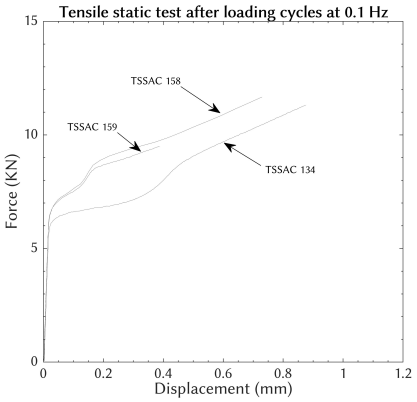
Specimen name	Notes before testing	Notes during testing (from video)	Whitening load (KN)	Failure load (KN)	Displacement at failure (mm)	Notes after testing
TSSAC 117	good quality	Whitening appears in a crescent shape around 80% of the connection radius and propagates towards the middle	6.23	10.17	0.769	1) Failure happened cohesively within the adhesive 2) The steel button is not completely detached from the glass
TSSAC 118	good quality	Whitening appears in a crescent shape around 80% of the connection radius and propagates towards the middle	6.03	11.80	1.091	1) Failure happened cohesively within the adhesive 2) The steel button is not completely detached from the glass
TSSAC 119	good quality	Whitening appears in a crescent shape around 80% of the connection radius and propagates towards the middle	4.91	9.62	0.598	1) Failure happened cohesively within the adhesive 2) The steel button is not completely detached from the glass

Appendix B.2 - Cyclic tensile test results at 0.1 Hz



Tensile cyclic loading at 0.1 Hz

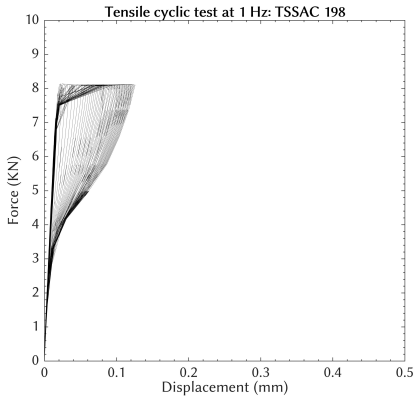
Specimen name	Notes before testing	Notes during testing (from video)	Whitening load (KN)
TSSAC 159	a lot of TSSA is squeezed out	whitening starts from the edges and propagated towards the middle	4.85
TSSAC 158	bad edge	-	4.40
TSSAC 134	a lot of TSSA is squeezed out	whitening starts from the edges and propagated towards the middle	-
TSSAC 120	good quality	1) Whitening appears at very small dots next to LVDT 2 2) Failure during cyclic loading at 7.87 KN	5.06

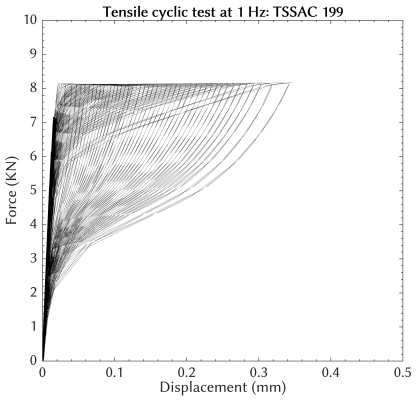


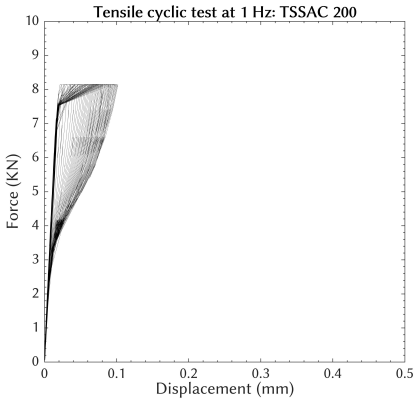
Tensile static test after cyclic loading at 0.1 Hz (displ. rate at 1mm/min)

Specimen name	Notes during testing (from camera)	Whitening load (KN)	Failure load (KN)	Displacement (mm)	Notes after testing
TSSAC 159	-	4.62	9.50	0.388	Failure happened cohesively within the adhesive
TSSAC 158	-	4.82	11.67	0.730	Failure happened cohesively within the adhesive
TSSAC 134	-	4.48	11.30	0.876	Failure happened cohesively within the adhesive

Appendix B.3 - Cyclic tensile test results at 1 Hz

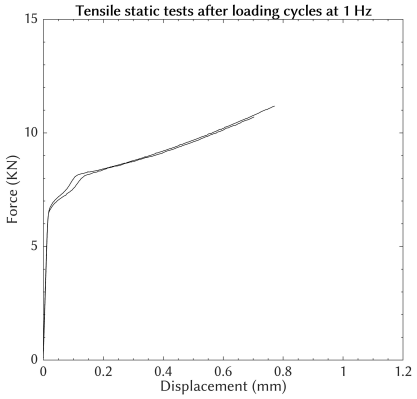






Tensile cyclic loading at 1 Hz

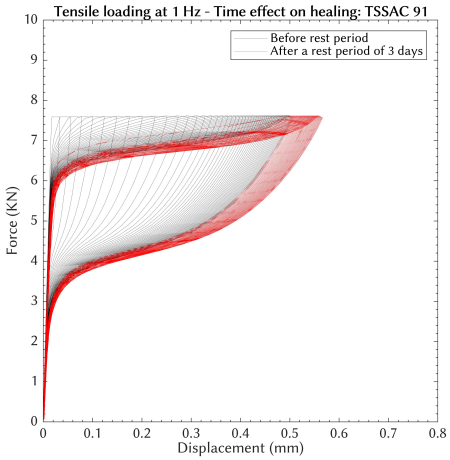
Specimen name	Notes before testing	Notes during testing (from video)
TSSAC 198	a lot of TSSA is squeezed out	Whitening appears during the first cycle from 0 to 6 KN
TSSAC 199	a lot of TSSA is squeezed out	1) Whitening appears close to the edge, near LVDT 2 2) A strip of TSSA does not turn white 3) Failure during cyclic loading at 8.17 KN 4) Bad lamination is observed from the whitening and the failure pattern
TSSAC 200	little TSSA is squeezed out	Whitening appears during the second cycle from 0 to 6 KN

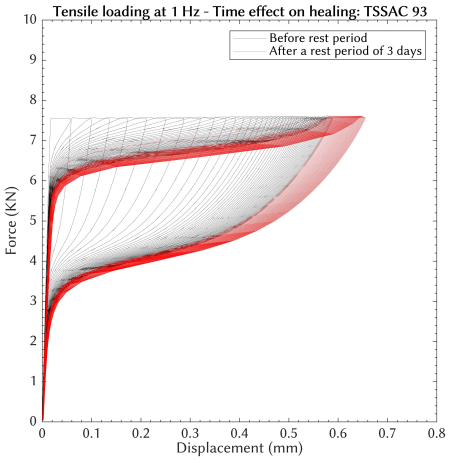


Tensile static test after cyclic loading at 1 Hz (displ. rate at 1mm/min)

Specimen name	Notes during testing (from camera)	Whitening load (KN)	Failure load (KN)	Displacement (mm)	Notes after testing
TSSAC 198	good quality	4.89	10.70	0.703	Failure happened cohesively within the adhesive
TSSAC 200	good quality	5.40	11.18	0.772	Failure happened cohesively within the adhesive

Appendix B.4 - Cyclic tensile tests related to healing





Specimen name	Notes before testing	Notes after testing
TSSAC 91	good quality	1) Failure happened cohesively within the adhesive 2) The steel connector was not completely detach from the glass
TSSAC 93	good quality	1) Failure happened cohesively within the adhesive

Appendix C

Appendix: Curve fitting hyperelastic and damage models to experimental data

Appendix C.1 - Engineering stress reformulations

Engineering stress reformulations

Material models	Uniaxial tension	Simple shear	Equibiaxial tension
Neo-Hookean $W_{iso} = C_{10}(\overline{I_1} - 3)$	$t_{11} = 2C_{10}\lambda_1(1 - \lambda_1^{-3})$	$t_{12} = 2C_{10}\gamma$	$t_{11} = t_{22} = 2C_{10}(\lambda - \lambda^{-5})$
Mooney-Rivlin (2 param.) $W_{iso} = C_{10}(\overline{I_1} - 3) +$ $+C_{01}(\overline{I_2} - 3)$	$t_{11} = 2(1 - \lambda_1^{-3})(C_{10}\lambda_1 +$ $+C_{01})$	$t_{12} = 2\gamma(C_{10} +$ $+C_{01})$	$t_{11} = t_{22} = 2C_{10}(\lambda - \lambda^{-5}) +$ $+2C_{01}(\lambda - \lambda^{-1})^3$
Mooney-Rivlin (3 param.) $W_{iso} = C_{10}(\overline{I_1} - 3) +$ $+C_{01}(\overline{I_2} - 3) +$ $C_{11}(\overline{I}_1 - 3)(\overline{I}_2 - 3)$	$t_{11} = 2(1 - \lambda_1^{-3})[(\lambda_1 C_{10} +$ $+C_{01} +$ $+3C_{11}(\lambda_1^{-1} + \lambda_1^2 - \lambda_1 - 1)]$	$t_{12} = 2\gamma C_{10} +$ $+2\gamma C_{01} +$ $+4\gamma^3 C_{11}$	$t_{11} = t_{22} = 4(\lambda - \lambda^{-5})[(C_{10} +$ $+C_{11}(\lambda^4 + 2\lambda^{-2} - 3)] +$ $+4(\lambda - \lambda^{-3})[C_{01} +$ $+C_{11}(2\lambda^2 + \lambda^{-4} - 3)]$
Yeoh $W_{iso} = C_{10}(\overline{I_1} - 3) +$ $+C_{20}(\overline{I_1} - 3)^2 +$ $+C_{20}(\overline{I_1} - 3)^3$	$t_{11} = 2\lambda_1(1 - \lambda_1^{-3})[C_{10} +$ $+2C_{20}(2\lambda_1^{-1} + \lambda_1^2 - 3) +$ $+3C_{30}(2\lambda_1^{-1} + \lambda_1^2 - 3)^2]$	$t_{12} = 2\gamma(C_{10} + 2C_{20}\gamma^2 +$ $+3C_{30}\gamma^4)$	$t_{11} = t_{22} = 2(\lambda - \lambda^{-5})(C_{10} +$ $+2C_{20}(2\lambda^2 + \lambda^{-4} - 3) +$ $+3C_{30}(2\lambda^2 + \lambda^{-4} - 3)^2)$
Gent-Thomas $W_{iso} = C_{10}(\overline{I_1} - 3) +$ $+C_{01} ln(\frac{\overline{I_2}}{3})$	$t_{11} = 2(1 - \lambda_1^{-3})[\lambda C_{10} +$ $+C_{01}(\lambda_1^{-2} + 2\lambda_1)^{-1}]$	$t_{12} = 2\gamma[C_{10} +$ $+C_{01}(3 + \gamma^2)^{-1}]$	$t_{11} = t_{22} = 2C_{10}(\lambda - \lambda^{-5}) +$ $+2C_{01}(\lambda - \lambda^{-1})^3(\lambda^4 + 2\lambda^{-2})^{-1}$

Appendix C.2 - Ogden-Roxburgh damage coefficients

		Maximum applied engineering stress							
Material models	Coeff.	0.5 MPa	1 MPa	1.5 MPa	2 MPa	2.5 MPa	3 MPa	3.5 MPa	4 MPa
	m	0.591	3.651	0.985	0.290	0.378	0.404	0.514	0.576
Ogden-Roxburgh	r	0.256	0.110	0.586	1.534	1.501	1.433	1.338	1.293
& Mooney-Rivlin	b	0.201	0.144	0.180	0.205	0.115	0.117	0.141	0.144
	R^2	0.9640	0.9767	0.9922	0.9943	0.9932	0.9836	0.9912	0.9885
	m	0.065	0.214	0.230	0.248	0.127	10^{-7}	10^{-7}	$2.59^{*}10^{-7}$
Ogden-Roxburgh	r	1.467	1.419	1.320	1.241	1.248	1.229	1.266	1.245
& Gent-Thomas	b	0.016	$9.55^{*}10^{-9}$	0.500	0.500	0.500	0.500	0.426	0.383
	R^2	0.9879	0.9943	0.9956	0.9923	0.9908	0.9921	0.9938	0.9944

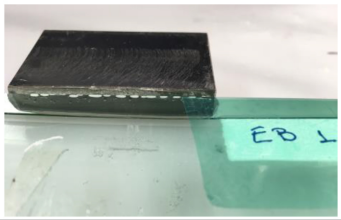
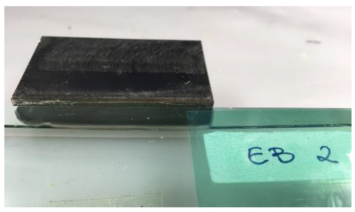
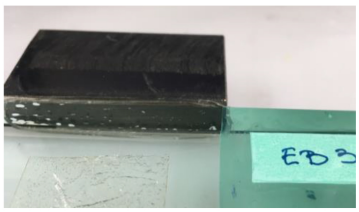
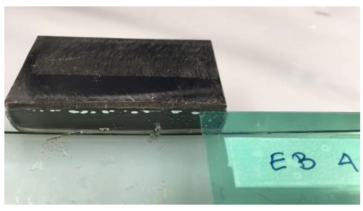
Appendix C.3 - Guo damage coefficients

		Maximum applied engineering stress							
Material models	Coeff.	0.5 MPa	1 MPa	1.5 MPa	2 MPa	2.5 MPa	3 MPa	3.5 MPa	4 MPa
	m	34.392	21.361	2.641	0.617	0.442	0.329	0.365	0.328
	r	0.121	0.125	0.00025	1.537	1.503	1.432	1.339	1.294
Guo	m_1	0.079	0.816	1.662	0.365	0.839	0.901	1.839	2.157
& Mooney-Rivlin	r_1	0.063	0.017	0.640	0.491	0.628	0.957	0.636	0.680
	$R^2_{unloading}$	0.9688	0.9816	0.9924	0.9962	0.9930	0.979	0.9904	0.9869
	$R^2_{reloading}$	0.7914	0.8896	0.9531	0.9742	0.9675	0.976	0.9640	0.9702

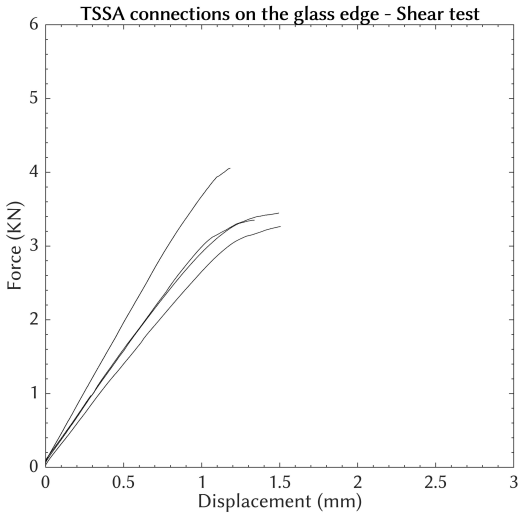
Appendix D

Appendix: TSSA laminated connections on the edge of the glass

Appendix D.1 - Quality of lamination

Specimens	Pictures	Comments
EB1 (Edge Bonding 1)		Air inclusions are concentrated on the edge of the adhesive. Bad lamination at the corners.
EB2 (Edge Bonding 2)		Significant accumulation of air inclusions is not observed. Bad lamination at the corners.
EB3 (Edge Bonding 3)		Air inclusions are concentrated on the left side of the connection. Bad lamination at the corners.
EB4 (Edge Bonding 4)		Some air inclusions are concentrated on the edge of the adhesive. Bad lamination at the corners.

Appendix D.2 - Experimental results



Shear static test (1 mm/min)

Specimen	Force at failure (KN)	Stress at failure (MPa)	Displacement at failure (mm)
EB1	3.45	4.60	1.494
EB2	3.35	4.47	1.339
EB3	4.06	5.41	1.184
EB4	3.26	4.35	1.507